ENHANCING ENERGY HARVESTING AND CONVERSION EFFICIENCIES OF HETEROGENEOUS PHOTOCATALYSTS FOR SOLAR WATER SPLITTING USING SURFACE PLASMON RESONANCE AND CATHODIC REDUCTION METHODS

by

JUE WANG

SHANLIN PAN, COMMITTEE CHAIR
ARUNAVA GUPTA
SHANE C. STREET
DANIEL J. GOEBBERT
YUPING BAO

A DISSERTATION

Submitted in partial fulfillment of the requirements
for the degree of Doctor of Philosophy
in the Department of Chemistry
in the Graduate School of
The University of Alabama

TUSCALOOSA, ALABAMA

2015

ABSTRACT

This dissertation presents surface enhanced photocatalytic characteristics of heterogeneous catalysts (e.g., α-Fe_2O_3 and CdS) for solar water splitting. The enhancement can be obtained by either incorporating plasmonic metallic nanostructures, such as Au nanorods (NRs), or cathodic reduction of catalytic materials. This dissertation also presents various electrochemical methods for large-scale synthesis of plasmonic structures (e.g., vertically aligned NRs) for surface enhanced photoelectrochemistry. Four major aspects of the dissertation are described briefly.

First, surface-enhanced light absorption and photoelectrochemical characteristics of α-Fe_2O_3 thin film modified with Au NRs in a top configuration are studied. The photoelectrochemical reaction of the plasmon active substrates for water oxidation is performed and compared at various α-Fe_2O_3 thicknesses. The photocurrent increase in the surface plasmon region is attributed to the enhanced visible light absorption of α-Fe_2O_3 in the presence of Au NRs.

Second, a template-free technique is invented for a facile fabrication of vertically standing metal NRs and nanowires (NWs). The growth mechanism of NRs and NWs is explored through investigating their morphological changes as the electrodeposition proceeds. Because of their large specific surface area, one direction alignment, stability, and wide tunability over the diameter, length, and coverage, these NRs and NWs will have broad applications in surface enhanced photoelectrochemical reaction and optical spectroscopy.

Third, cathodic reduction methods are introduced and they are capable of improving the photoelectrochemical performance of α-Fe_2O_3 photoanode. The morphology and photoelectrochemical responses of α-Fe_2O_3 thin-film photoanode are presented before and after the cathodic reduction. The photocurrent of ~20 nm α-Fe_2O_3 thin film is enhanced by about 7 times after the cathodic reduction. The enhancement is attributed to the conductivity improvement.

Finally, vertical-aligned Ag nanoplates and NWs are presented at the outlet of this dissertation. These nanostructures are electrochemically deposited on Indium Tin Oxide (ITO) substrates with the assistance of sacrificial templates such as anodic aluminum oxide (AAO) templates. Ag nanostructures obtained using this method have minimum contamination because no surfactant is adopted for the synthesis; therefore they are suitable for surface modifications for applications in surface-enhanced Raman scattering, surface-enhanced photocatalyst, and metal-enhanced fluorescence.

DEDICATION

This dissertation is dedicated to everyone who helped me and guided me through the trials and tribulations of creating this manuscript. In particular, my family and friends who stood by me throughout the time taken to complete this masterpiece.

LIST OF ABBREVIATIONS AND SYMBOLS

A	Absorbance
AAO	Anodic Aluminum Oxide
AC	Alternating Current
APCVD	Atmospheric pressure chemical vapor deposition
AU	Arbitrary Unit
b	Light-path length
c	Concentration
CBD	Chemical Bath Deposition
CTAB	Cetyltrimethylammonium bromide
CV	Cyclic Voltammetry
C_{SC}	Capacitance of the space charge region
d	Distance
DC	Direct Current
DDA	Discrete dipole approximation
DI	Deionized
e	Electronic charge
ε	Dielectric constant
ε_0	Permittivity of free space
E	Potential
E^0	Equilibrium potential

E_{FB}	Flatband potential
eV	Electron volt
FTO	Fluorine-doped Tin Oxide
H	Hour
i_{dark}	Dark current
i_{photo}	Photo current
ITO	Indium Tin Oxide
IPCE	Incident photon-to-current efficiency
j_{ph}	Photocurrent density
k	Boltzmann's constant
λ	Photon wavelength
MW	Molecular weight
N	Donor density
NHE	Normal hydrogen electrode
NR	Nanorod
NW	Nanowire
ν	Frequency
PEDOT: PSS	Poly(3,4-ethylenedioxythiophene)-poly(styrenesulfonate)
pH	The acidity or basicity of an aqueous solution
P_{mono}	Light intensity at a given wavelength
PS	Polystyrene
PSS	Poly(styrenesulfonate)
R6G	Rhodamine 6G

θ	Angle
3D	Three dimensional
SCE	Saturated Calomel Electrode
SEM	Scanning Electron Microscopy
SERS	Surface Enhanced Raman Spectroscopy
T	Temperature
TEM	Transmission Electron Microscopy
UV-Vis	Ultra-Violet Visible
V	Voltage
XRD	X-Ray Diffraction

ACKNOWLEDGMENTS

I am pleased to have this opportunity to thank the many colleagues, friends, and faculty members who have helped me with this research project. I am most indebted to Dr. Shanlin Pan, my research adviser and the chairman of this dissertation committee, for sharing his research expertise and ideas. I would also like to thank all of my committee members, Dr. Arunava Gupta, Dr. Shane Street, Dr. Daniel Goebbert, and Dr. Yuping Bao for their invaluable input, inspiring questions, and support of both the dissertation and my academic progress. I would like to thank the staffs in Central Analytical Facility (CAF) for their assistance in XRD and SEM measurements. I also thank Dr. Daniel Clayton, Dr. Caleb Hill, and Dr. Robert Bennett for their suggestions and assistance with TEM and Raman characterization.

This material is supported by the National Science Foundation under award number CHE-1153120. Jue Wang is also partially supported by a graduate fellowship support from China Scholarship Council.

CONTENTS

LIST OF TABLES

LIST OF FIGURES

CHAPTER 1

INTRODUCTION

1.1 Solar Energy Potential for Solar Water Splitting and a Brief History of Photoelectrochemistry of Hematite Photoanode

In recent decades, the global energy consumption is soaring because of the rising living standards and it is predicted to at least be doubled from the current rate of 12.8 TW to 28 – 35 TW in 2050 (TW = 10^{12} watts).[1] To meet the increasing demand of energy while nullifying the detrimental environmental impact from the CO_2 generated by the consumption of fossil fuels, exploring and developing green energy sources is never overemphasized. While no single source is able to suffice the needs currently, our largest green energy source the Sun could easily supply the adequate energy if it is efficiently harvested. However, the direct use of solar cell, such as solar thermal power or photo-voltaic cells, is still quite limited, only accounting for 0.22% of total primary energy consumption of US in 2013.[2]

Photoelectrochemical systems hold the promise of providing electric power and clean renewable energy sources using solar energy. For example, solar cells based on photoelectrochemical reaction have been developed to capture solar energy for the direct production of electricity.[3,4,5,6] It is worth noting that solar cells only produce electricity under sunlight, which means no energy can be produced in the evening and desires a solution to store the energy they generate under the sunlight for the utilization without sunlight. So far, the most practical and efficient way to store the energy is through a chemical carrier. Hydrogen is one of the best candidates as an energy carrier and it becomes water after combustion without producing

any waste. Direct water splitting using sunlight for hydrogen production with photocatalysts have been intensively explored[7] since the original experiment demonstrating the use of TiO_2 for splitting water under UV light.[8] The water-splitting process through an n-type semiconductor is shown in Figure 1.1. When the semiconductor is illuminated by the photons with energy larger than the bandgap of the semiconductor, the electrons on the valence band will be excited to the conduction band and these excited electrons could reduce the protons to hydrogen if the conduction-band edge of the semiconductor is higher the reduction potential of H^+/H_2 (E^0=0.0 V vs. NHE). NHE represents Normal Hydrogen Electrode. The holes left on the valence band are able to oxidize water to generate oxygen if the valence-band edge of the semiconductor is lower than the oxidation potential of H_2O/O_2 (E^0=1.23 V vs. NHE). Although TiO_2 is a low cost material and remains one of the most studied photocatalysts for photoelectrochemical applications, its bandgap of near 3.0 eV limits the operation wavelengths of light to be less than 400 nm, thereby yielding low power efficiencies for hydrogen production using visible solar radiation. Attempts to search for semiconductors other than TiO_2 have continued and many possible alternatives have been discovered. For example, new types of oxynitrides (e.g., $(Ga_{1-x}Zn_x)(N_{1-x}O_x)$[9]) and doped TiO_2 have shown visible light sensitivity for direct water splitting under sun light.[10,11,12,13] Continued catalyst improvements are required for real technological applications which require lower costs and improved efficiencies and the ability to meet the following criteria.[5,14] (1) A minimum bandgap of about 1.6 eV is needed, which is the equilibrium potential difference between the redox pairs of H^+/H_2 (E^0=0.0 V vs. NHE) and H_2O/O_2 (E^0=1.23 V vs. NHE) at 25°C in addition to the energy losses in the semiconductor for charge carrier transport. Such a band gap allows a photocatalyst to absorb light in most of the visible light spectrum. Considering the over-potential losses, 2.0 eV is an ideal bandgap for the

semiconductor, corresponding to an absorption onset at 620 nm. (2) The valence band edge energy level for an n-type semiconductor should be lower than the H_2O/O_2 oxidation potential, and the conduction band edge should be higher than the H^+/H_2 reduction potential to obtain a high incident photon-to-current efficiency (IPCE). (3) The photocatalyst must be stable in aqueous solution without changing its composition and electronic structure by photo-oxidation and/or corrosion caused by changes in local pH during the course of photoelectrochemical reaction. (4) The material used should be low cost. (5) The material should minimize over-potential losses.

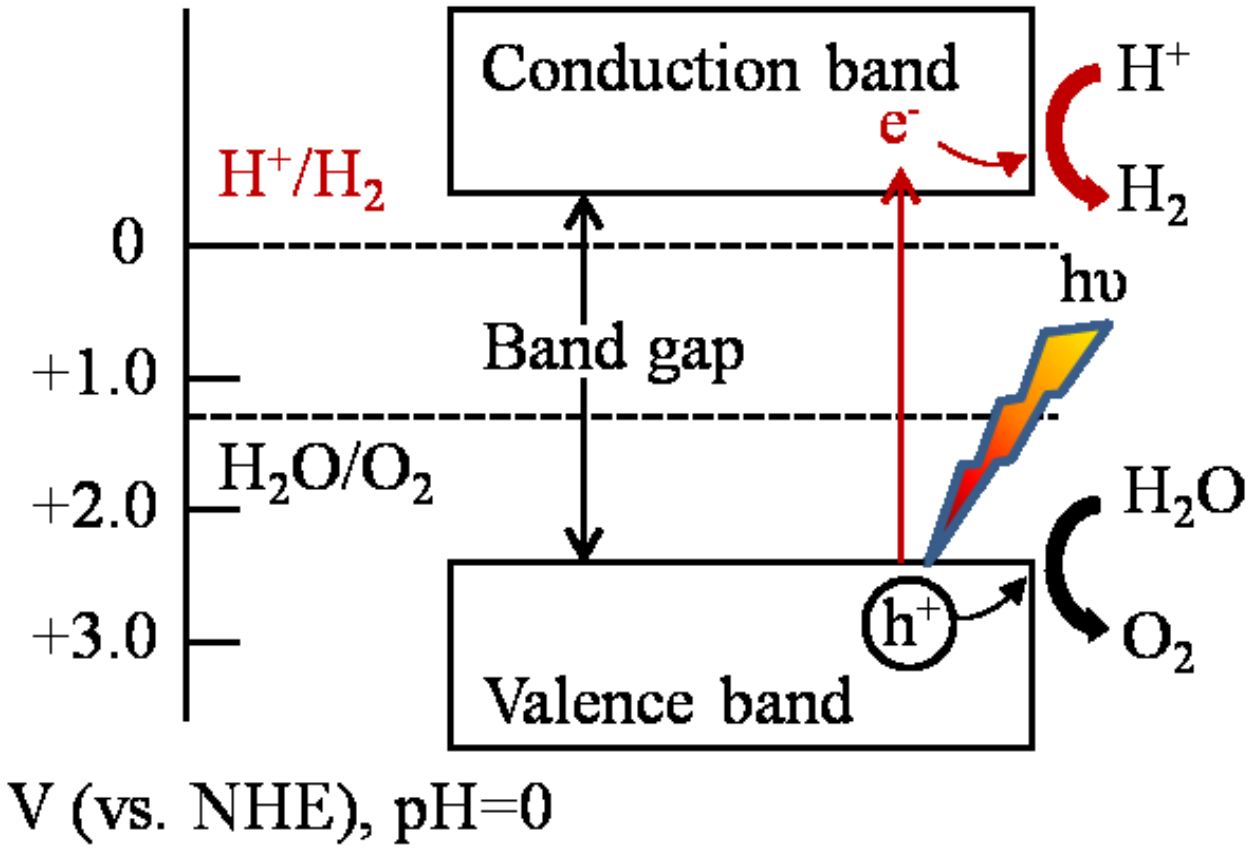

Figure 1.1 Water-splitting processes through an n-type semiconductor in aqueous solution.

No single semiconducting material has yet been found which meets all five criteria. Hematite (α-Fe_2O_3) meets at least three of the above criteria as it has a band gap around 2.0 eV, a good chemical stability in aqueous environments, and low cost as iron is one of the most abundant materials on earth. A theoretical water splitting efficiency of 16.8% has been predicted for hematite.[15] A number of research groups have studied the use of hematite as an oxygen-evolving photoanode but only obtained poor efficiency because of several intrinsic limitations of this oxide material.[16,17]Hematite possesses a conduction band edge at an energy level below the H^+/H_2 reduction potential as shown in Figure 1.2. Thus, one needs to either apply an external electrical bias or couple the hematite electrode with a solar cell in order to collected the excited electrons from its conduction band and deliver the electrons to a noble metal electrode such as Pt for water reduction reaction. For example, unassisted solar hydrogen production can be achieved by incorporating hematite in a tandem cell configuration.[18,19] While hematite has a light penetration depth of 118 nm (at λ=550 nm),[20] it has a very small hole diffusion length (2-4 nm[21,22] or 20 nm[23]). This means that a majority of the photons absorbed by a relatively thick hematite layer are not used to oxidize water at the solid-liquid interface, which is displayed in Figure 1.3. This problem can be partially addressed by using a doping agent to improve the conductivity of the thin film electrode made of hematite. For example, silicon-doped hematite thin films and nanostructures, prepared by atmospheric pressure chemical vapor deposition (APCVD),[24] have a variety of nanostructured morphologies and exhibit a solar-to-hydrogen conversion efficiency of more than 3% in a tandem configuration. This efficiency is still far below the theoretical prediction largely due to the thick hematite nanostructure, which increases the number of photons absorbed to generate electron and hole carriers but hole transport is limited to a distance of 2-4 nm or 20 nm. WO_3 has recently been utilized as a scaffold for a few

nanometer thick α-Fe_2O_3 layer to increase the hole-collection efficiency,[12] but at the expense of sacrificing the light absorption. A different methodology, which would enable efficient visible light absorption while retaining efficient hole transport through the thin film, is needed in order to improve the overall photoelectrochemical performance of a visible-light-active photocatalyst such as hematite.

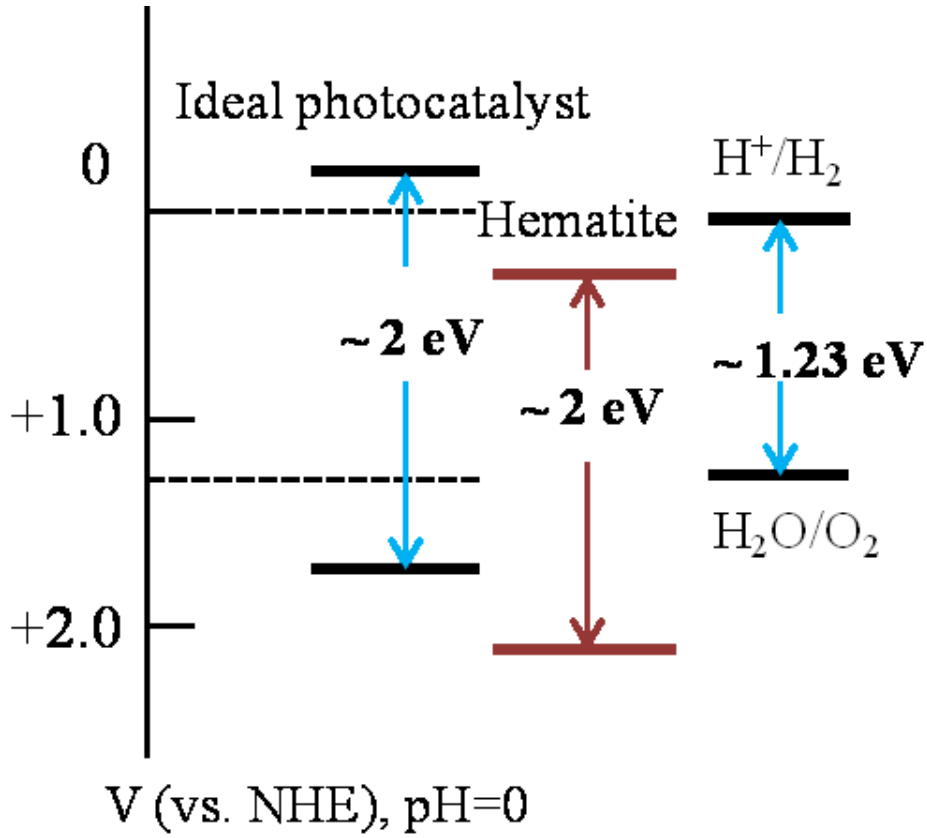

Figure 1.2 Band edge positions of hematite compared with the ideal photocatalyst.

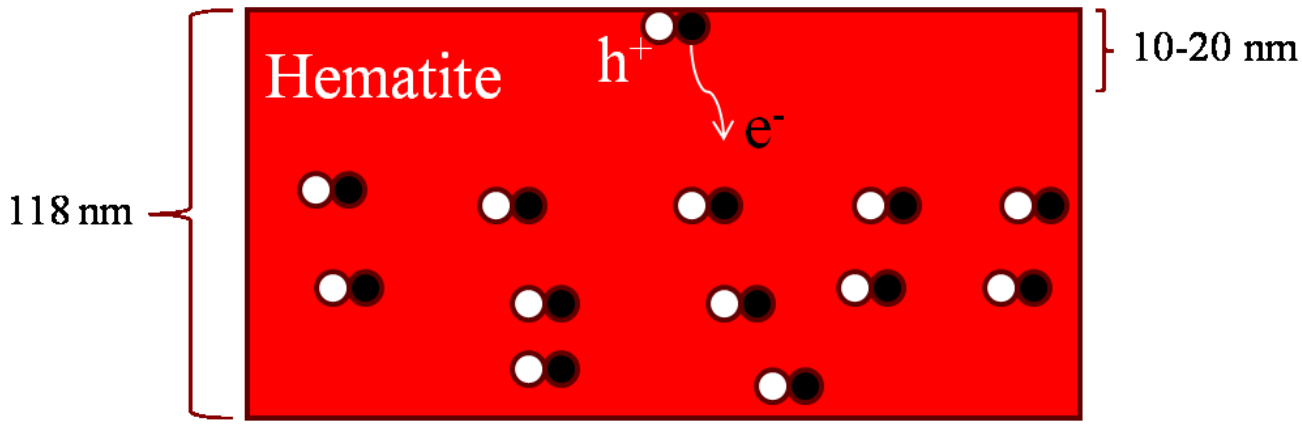

Figure 1.3 Comparison of the hole transport distance of hematite with its light penetration depth.

1.2 Surface Plasmon Resonance and Brief Introduction of Plasmon Enhanced Solar Water Splitting

One solution to increase the photoelectrochemical performance of a photocatalyst would be to enhance its light absorption using the surface plasmon of metallic nanoparticles as shown in the review article.[25] Surface plasmon resonances refer to the collective oscillating motion of conductive electrons near a metal surface, such as gold and silver, when an external electromagnetic field is applied. Surface plasmons can be excited from the surfaces of metallic nanoparticles.[26,27,28] The extinction spectra of metallic nanoparticles are usually dominated by one or more well-resolved peaks, which are caused by strong light scattering and absorption. The surface plasmon frequency is determined not only by the dispersion relation of the metal but also by a number of other parameters, such as particle size and shape, surface modification of the particle, and changes in dielectric constant of the surrounding medium. Coupling between individual particles and particle geometry can also dramatically influence the position of the plasmon resonance.[29] Surface plasmons of silver nanoparticles can cause significant enhancement in the local electromagnetic field due to the intense surface plasmon resonance cross-section of silver.[30] Coupling between two or more metallic nanoparticles can localize their excited states between the particles to produce much stronger local field intensity than individual nanoparticles. Surface plasmons near an organic or inorganic semiconductor material have been found to enhance their light absorption by amplifying the electromagnetic field intensity sensed by the system without significant quenching their fluorescence.[31]

Numerous recent studies show that a visible light photoelectrochemical response can be observed for thin film electrodes made of TiO_2 by doping with silver and gold nanoparticles.[32,33,34,35,36,37] More recently, Thimsen et al.[38] studied the effects of bare spherical gold particles on the photocatalytic performance of α-Fe_2O_3 electrodes with the gold

nanoparticles embedded in the hematite layer and on its surface. The embedded gold nanoparticles were found to have no effect on hematite performance, whereas the surface coating configuration on hematite nanoplatelets allowed gold nanoparticles to have a spectroscopic effect on the photocurrent response of the electrode due to their surface plasmon. However, the overall power efficiency was decreased upon the gold nanoparticle modification. More recently, Thomann et al.[39] reported that bare spherical gold nanoparticles would decrease the photocatalytic behavior of α-Fe_2O_3 in both embedded and top configurations because gold can serve as a charge recombination center. In contrast, silica shell coated gold nanoparticles can enhance photocatalytic efficiency by the surface plasmon of gold particles because the charge recombination is blocked by the silica.[40] In addition, different enhancement action spectra were observed for embedded and top configurations due to the changes in electronic structure and morphology of hematite at the solid-liquid interface in the presence of silica coated gold nanoparticles. Gao et al. showed an enhanced photocurrent in a thin-film iron oxide photoanode coated on gold nanopillars.[41] However, their enhancement factor was measured from 500 nm to 700 nm where the IPCE is close to zero. This means that a substantial amount of noise was introduced when the relative enhancement from the plasmon is calculated by dividing the spectra of the gold nanopillar-enhanced hematite by that of a pristine hematite film to show the spectroscopic response of the current to the plasmon.

In addition to the controversies in literature on plasmon effects on the photolectrochemical performance of hematite,[42] additional experimental evidences are needed to fully understand the enhancement effect in the presence of Au plasmonic antenna in a photoelectrochemical system. (1) How will the plasmon effect on the photoelectrochemical reaction depend on the thickness of the hematite layer and what is the optimal thickness of the

film needed for surface enhancement? (2) How will the enhancement effect depend on the shape of the gold nanoparticle? (3) How is the photoelectrochemical performance determined by the electrode potential and affected by the background current?

Besides enhancing the absorbance of hematite by using surface plasmon, improving the conductivity of hematite is an effective way to improve the photoelectrochemical performance of hematite as well. For example, enhanced PEC effect has been obtained by doping hematite with transition metals[43,44,45] to increase the charge carrier transport and collection efficiencies. However, very few electrochemical methods, which are facile, low cost, and efficient, have been developed to improve the photoelectrochemical performance of hematite.

1.3 Introduction of Template Based Methods for Preparing Nanostructures

AAO template as exhibited in Figure 1.4 is widely utilized for preparing NWs because of its highly ordered structure and low cost. By convention, a conductive layer like Au or Ag is required to be deposited on one side of the AAO template to serve as a cathode since AAO template is an insulator.[46,47,48] A drawback of this method is that the prepared NWs easily collapse after removing AAO template because the thin conductive layer is not a rigid support. [49] It has been reported that AAO template was prepared directly on Si substrate for the electrodeposition of NWs.[50] However, for most optoelectronic applications, substrates are required to be transparent to let the majority of incident or emitted light pass through, which limits the application of opaque Si substrates. Therefore, a method of fabricating nanowires on conductive, transparent, and rigid substrate like Indium Tin Oxide (ITO) is in demand.

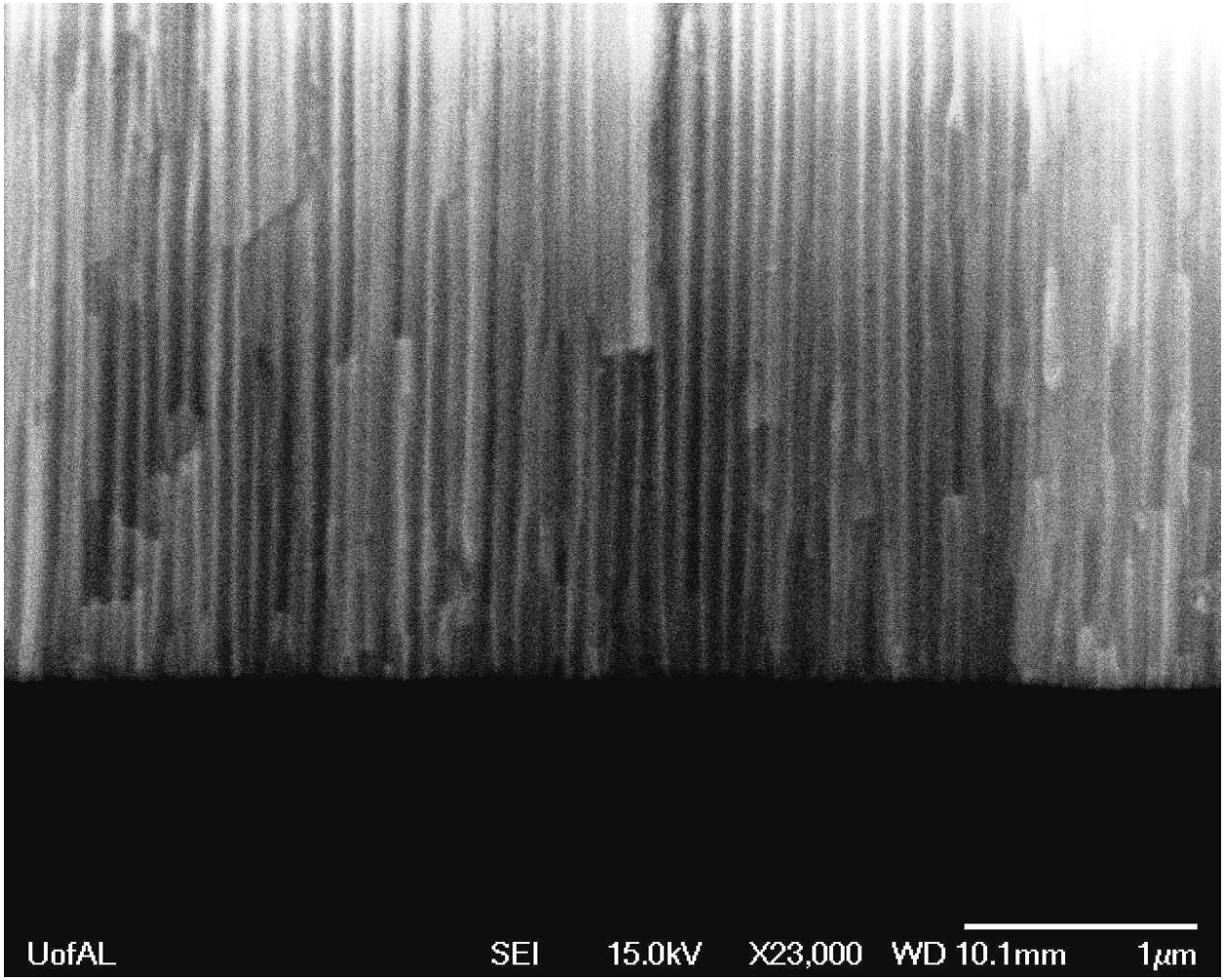

Figure 1.4 Cross section Scanning Electron Microscopy (SEM) image of AAO template.

Some groups prepared AAO template on ITO substrate by directly anodizing the Al film on ITO substrate for preparing NWs.[51,52] The Al layer was deposited on ITO substrate through sputtering or electron-beam evaporation, which are energy consuming and costly. Additionally, to obtain an appropriate Al film for anodization, a 50 μm thick Al layer in high quality is necessary, which is difficult to obtain such a thick layer by sputtering and electron-beam evaporation. Furthermore, because the adhesion between Al and ITO substrate is poor and ITO substrate is easily destroyed under high anodizing voltage, generally, a thin interlayer of Ti or W (between Al layer and ITO substrate) in nanometers or even less than one nanometer is introduced.[53,54] Such thin film is difficult to obtain and the oxide of Ti and W formed during the anodization will create a barrier between AAO template and ITO substrate, which is not beneficial for the electrodeposition. Therefore, a simple and cost-effective method is desirable for a large scale fabrication of NRs and NWs on conductive and transparent substrates.

Recently, Byun et al[55] and Gu et al[56] reported electrodeposition of nanowires on ITO substrate by grafting AAO template on the substrate. The adhesion between AAO template and ITO substrate is poor because AAO template is hydrophilic while ITO substrate has poor hydrophilicity. Therefore, to improve the adhesion between AAO template and ITO substrate, a layer of dihydroxy-terminated polystyrene (PS-dOH)[55] or polyvinyl alcohol (PVA)[56] was spun-coated on ITO substrate before grafting AAO template. However, these two polymers are nonconductive, which may block the electrodeposition. Additionally, ozone treatment is desired to improve the hydrophilicity of PS-dOH and the hot water is required to remove the ungrafted PVA polymer. Meanwhile, either $HgCl_2$[55] or $SnCl_4$[56], both highly toxic and corrosive, were used to dissolve Al substrate to obtain AAO template. Therefore, an environment-friendly method

which employs a conductive polymer to graft AAO template for preparing NWs on transparent substrate is desirable.

Besides using AAO for preparing NWs, sparse research has been carried out on using AAO template to prepare two-dimensional nanoplates[57] which are attractive.[58,59] Current methods for fabricating nanoplates majorly utilize surfactants, such as polyvinylpyrrolidone (PVP)[60] and Cetyltrimethylammonium bromide (CTAB)[61], or halide ions[62] to direct the anisotropic growth of Ag nanostructures and protect them from aggregations, which may introduce heterogeneous impurities and it is adverse for the surface modification. To avoid the usage of surfactants, a galvanic fabrication method has been developed for the fabrication of Ag nanoplates.[63] However, in this method, highly hazardous HF was used to refresh the oxide layer before the galvanic reaction, not to mention the F^- in the HF residue could easily bind with Ag and is a possible reason for the growth of Ag nanoplates. Therefore, a simple, low cost, and environmental-friendly method for the fabrication of Ag nanoplates is in demand. Considering the parallel channels of AAO template could control the migrating direction of ions, Ag nanoplates could be achievable through carrying out electrodeposition under AAO template if we control the distance between AAO template and conductive substrate very well.

1.4 Introduction of Template Free Method for Formation of Three Dimensional Nanostructures

The traditional way to prepare vertically aligned NRs and NWs on rigid substrates is through electrodeposition in AAO templates on conductive substrates which direct the growth of NRs and NWs and will be etched away using a basic solution after the electrodeposition, leaving NRs and NWs on the substrate. There are several limitations of using AAO template, such as non-flexible, time-consuming to prepare and also limited in size when a uniform and ultra-thin template is needed. Meanwhile, mounting AAO template on the substrate is labor intensive and

costly. Therefore, a template-free and low cost technique for the fabrication of vertically standing NRs and NWs in a large scale for practical application is in high demand.

Recently, a process termed filamentary one-dimensional nanocrystal growth in an ultra-dilute electrolyte was reported for preparing vertically standing metal NRs and NWs on conductive substrates without using template. A locally enhanced electric filed similar to the lightning-rod effect was proposed as the growth mechanism.[64,65] A three-electrode system with a Pt wire working as counter electrode and a Ag/AgCl electrode serving as reference electrode was adopted in this method.

Using a Pt wire as the counter electrode would limit the scale-up of the fabrication of vertically standing NRs and NWs because the uniform distribution of the electric field is difficult to maintain for a wire counter electrode. In addition, a three-electrode system is complicated and expensive for mass production. Therefore, a low-cost and template free technique based on a two-electrode system should be developed for mass-production of vertically standing NRs and NWs.

Chapter 2 of this dissertation is dedicated to experimental methods and instruments used in all experiments described in this dissertation. More specific experimental conditions are described in each of the following chapters. Chapter 3 illustrates the optical property and photoelectrochemical performance change of α-Fe_2O_3 after the modification with Au NRs in a top configuration. It was found that the Au NRs attached on α-Fe_2O_3 surface are not very stable and the background current is seriously enlarged by the Au NRs because of the enhanced charge recombination. Meanwhile, the contact area between the Au NRs and α-Fe_2O_3 is relatively small. In chapter 4, a new method is presented to form vertically standing Ag NRs and NWs with a three dimensional (3D) structure. This method deals with the electrochemical deposition of

vertically standing NR and NWs on conductive substrates and these nanostructures have good contact with the conductive substrates. The influences of the surface plasmon of Ag NRs and NWs on the optical properties and photoelectrochemical performance of photocatalyst were investigated. Besides using the surface plasmon of noble metal to increase the absorbance of photocatalyst and hence improve their photoelectrochemical performance, increasing the conductivity of the photocatalyst could be another option to enhance the performance of photocatalyst. In chapter 5, cathodic reduction methods were developed to improve the performance of hematite thin film and the enhancement of the photocurrent density was found to be phenomenal.

It is also attractive to apply surface plasmon resonance in Raman spectroscopy which is nondestructive and fast, but limited by its relatively weak signal. Surface plasmon resonance could magnify the Raman signal up to $10^5 – 10^8$ times[66] through enhancing the local electromagnetic field or/and initiating a charge transfer between the chemisorbed species and metal surface. However, the surface plasomon of metal nanostructures largely depends on their shape, size, and coverage. Therefore, in chapter 6 and 7, vertically aligned Ag nanostructures with a control over the shape, size, and coverage of nanostructures were successfully prepared based on AAO templates. They were found to be sensitive and reproducible substrates for Surface Enhanced Raman Spectroscopy (SERS). Challenging issues and possible solutions to address these issues and future work are discussed in chapter 8.

REFERENCES

(1) http://web.mit.edu/professional/short-programs/courses/solar_energy.html.

(2) http://www.eia.gov/totalenergy/data/monthly/pdf/sec2_13.pdf.

(3) O'Regan, B.; Grätzel, M. A Low-Cost, High-Efficiency Solar-Cell Based on Dye-Sensitized Colloidal TiO_2 Films. *Nature* **1991***, 353*, 737-740.

(4) Kuang, D.; Brillet, J.; Chen, P.; Takata, M.; Uchida, S.; Miura, H.; Sumioka, K.; Zakeeruddin, S. M.; Grätzel, M. Application of Highly Ordered TiO_2 Nanotube Arrays in Flexible Dye-Sensitized Solar Cells. *ACS Nano* **2008***, 2*, 1113-1116.

(5) Tiwana, P.; Docampo, P.; Johnston, M. B.; Snaith, H. J.; Herz, L. M. Electron Mobility and Injection Dynamics in Mesoporous ZnO, SnO_2, and TiO_2 Films used in Dye-Sensitized Solar Cells. *ACS Nano* **2011***, 5*, 5158-5166.

(6) Wang, D.; Liu, Y.; Wang, C.; Zhou, F.; Liu, W. Highly Flexible Coaxial Nanohybrids made from Porous TiO_2 Nanotubes. *ACS Nano* **2009***, 3*, 1249-1257.

(7) Grimes, C. A.; Varghese, O. K.; Ranjan, S. In *Light, water, hydrogen : the solar generation of hydrogen by water photoelectrolysis;* Springer Science+Business Media, LLC: New York, U.S.A, **2008**.

(8) Fujishima, A.; Honda, K. Electrochemical Photolysis of Water at a Semiconductor Electrode. *Nature* **1972***, 238*, 37-38.

(9) Maeda, K.; Domen, K. New Non-Oxide Photocatalysts Designed for overall Water Splitting Under Visible Light. *J. Phys. Chem. C* **2007***, 111*, 7851-7861.

(10) Wang, J.; Tafen, D. N.; Lewis, J. P.; Hong, Z.; Manivannan, A.; Zhi, M.; Li, M.; Wu, N. Origin of Photocatalytic Activity of Nitrogen-Doped TiO_2 Nanobelts. *J. Am. Chem. Soc.* **2009***, 131*, 12290-12297.

(11) Shankar, K.; Basham, J. I.; Allam, N. K.; Varghese, O. K.; Mor, G. K.; Feng, X.; Paulose, M.; Seabold, J. A.; Choi, K.; Grimes, C. A. Recent Advances in the use of TiO_2 Nanotube and Nanowire Arrays for Oxidative Photoelectrochemistry. *J. Phys. Chem. C* **2009***, 113*, 6327-6359.

(12) Tafen, D. N.; Wang, J.; Wu, N.; Lewis, J. P. Visible Light Photocatalytic Activity in Nitrogen-Doped TiO_2 Nanobelts. *Appl. Phys. Lett.* **2009***, 94*, 093101-1-093101-3.

(13) Lee, W. J.; Lee, J. M.; Kochuveedu, S. T.; Han, T. H.; Jeong, H. Y.; Park, M.; Yun, J. M.; Kwon, J.; No, K.; Kim, D. H.; Kim, S. O. Biomineralized N-Doped CNT/TiO_2 Core/Shell Nanowires for Visible Light Photocatalysis. *ACS Nano* **2012***, 6*, 935-943.

(14) Sivula, K.; Formal, F. L.; Grätzel, M. WO_3−Fe_2O_3 Photoanodes for Water Splitting: A Host Scaffold, Guest Absorber Approach. *Chem. Mater.* **2009***, 21*, 2862-2867.

(15) Murphy, A. B.; Barnes, P. R. F.; Randeniya, L. K.; Plumb, I. C.; Grey, I. E.; Horne, M. D.; Glasscock, J. A. Efficiency of Solar Water Splitting using Semiconductor Electrodes. *Int J Hydrogen Energy* **2006***, 31*, 1999-2017.

(16) Tahir, A. A.; Wijayantha, K. G. U.; Saremi-Yarahmadi, S.; Mazhar, M.; McKee, V. Nanostructured α-Fe_2O_3 Thin Films for Photoelectrochemical Hydrogen Generation. *Chem. Mater.* **2009***, 21*, 3763-3772.

(17) Mohapatra, S. K.; John, S. E.; Banerjee, S.; Misra, M. Water Photooxidation by Smooth and Ultrathin α-Fe_2O_3 Nanotube Arrays. *Chem. Mater.* **2009***, 21*, 3048-3055.

(18) Ingler, W. B.; Khan, S. U. M. A Self-Driven p/n-Fe_2O_3 Tandem Photoelectrochemical Cell for Water Splitting. *ECS Solid State Lett.* **2006***, 9*, G144-G146.

(19) Wang, H.; Deutsch, T.; Turner, J. A. Direct Water Splitting Under Visible Light with Nanostructured Hematite and WO_3 Photoanodes and a $GaInP_2$ Photocathode. *J. Electrochem. Soc.* **2008***, 155*, F91-F96.

(20) Balberg, I.; H.L. Pinch The Optical Absorption of Iron Oxides. *J Magn Magn Mater* **1978***, 7*, 12-15.

(21) Kennedy, J. H.; Frese, J.,Karl W. Photooxidation of Water at α-Fe_2O_3 Electrodes. *J. Electrochem. Soc.* **1978***, 125*, 709-714.

(22) Kennedy, J. H.; Jr., K. W. F., Flatband Potentials and Donor Densities of Polycrystalline α-Fe_2O_3 Determined from Mott-Schottky Plots. *J. Electrochem. Soc.* **1978***, 125*, 723-726.

(23) Dare-Edwards, M.; Goodenough, J. B.; Hamnett, A.; Trevellick, P. R. Electrochemistry and Photoelectrochemistry of Iron(III) Oxide. *J. Chem. Soc. , Faraday Trans. 1* **1983***, 79*, 2027-2041.

(24) Kay, A.; Cesar, I.; GrÃ¤tzel, M. New Benchmark for Water Photooxidation by Nanostructured α-Fe_2O_3 Films. *J. Am. Chem. Soc.* **2006***, 128*, 15714-15721.

(25) Pan, S. L.; Gupta, A. Surface-Enhanced Solar Energy Conversion Systems using Gold and Silver Nanoparticles. *Material Matters* **2012***, 7*, 64-66.

(26) Weber, M. L.; Litz, J. P.; Masiello, D. J.; Willets, K. A. Super-Resolution Imaging Reveals a Difference between SERS and Luminescence Centroids. *ACS Nano* **2012***, 6*, 1839-1848.

(27) Yan, B.; Thubagere, A.; Premasiri, W. R.; Ziegler, L. D.; Dal Negro, L.; Reinhard, B. M. Engineered SERS Substrates with Multiscale Signal Enhancement: Nanoparticle Cluster Arrays. *ACS Nano* **2009***, 3*, 1190-1202.

(28) Yap, F. L.; Thoniyot, P.; Krishnan, S.; Krishnamoorthy, S. Nanoparticle Cluster Arrays for High-Performance SERS through Directed Self-Assembly on Flat Substrates and on Optical Fibers. *ACS Nano* **2012***, 6*, 2056-2070.

(29) Dadosh, T.; Sperling, J.; Bryant, G. W.; Breslow, R.; Shegai, T.; Dyshel, M.; Haran, G.; Bar-Joseph, I. Plasmonic Control of the Shape of the Raman Spectrum of a Single Molecule in a Silver Nanoparticle Dimer. *ACS Nano* **2009***, 3*, 1988-1994.

(30) Brus, L. Noble Metal Nanocrystals: Plasmon Electron Transfer Photochemistry and Single-Molecule Raman Spectroscopy. *Acc. Chem. Res.* **2008***, 41*, 1742-1749.

(31) Schalkhammer, T.; Aussenegg, F. R.; Leitner, A.; Brunner, H.; Hawa, G.; Lobmaier, C.; Pittner, F. Detection of Fluorophore-Labelled Antibodies by Surface-Enhanced Fluorescence on Metal Nanoislands. *Proc SPIE Int Soc Opt Eng* **1997***, 2976*, 129-136.

(32) Zhang, H.; Wang, G.; Chen, D.; Lv, X.; Li, J. Tuning Photoelectrochemical Performances of Ag-TiO_2 Nanocomposites Via reduction/oxidation of Ag. *Chem. Mater.* **2008***, 20*, 6543-6549.

(33) Zheng, J.; Yu, H.; Li, X.; Zhang, S. Enhanced Photocatalytic Activity of TiO_2 Nano-Structured Thin Film with a Silver Hierarchical Configuration. *Appl. Surf. Sci.* **2008***, 254*, 1630-1635.

(34) Gorzkowska–Sobas, A.; Kusior, E.; Radecka, M.; Zakrzewska, K. Visible Photocurrent Response of TiO_2 Anode. *Surf. Sci.* **2006***, 600*, 3964-3970.

(35) He, J.; Yang, P.; Sato, H.; Umemura, Y.; Yamagishi, A. Effects of Ag-Photodeposition on Photocurrent of an ITO Electrode Modified by a Hybrid Film of TiO_2 Nanosheets. *J Electroanal Chem* **2004***, 566*, 227-233.

(36) Zhao, G.; Kozuka, H.; Yoko, T. Sol—gel Preparation and Photoelectrochemical Properties of TiO_2 Films Containing Au and Ag Metal Particles. *Thin Solid Films* **1996***, 277*, 147-154.

(37) Sun, L.; Li, J.; Wang, C.; Li, S.; Lai, Y.; Chen, H.; Lin, C. Ultrasound Aided Photochemical Synthesis of Ag Loaded TiO_2 Nanotube Arrays to Enhance Photocatalytic Activity. *J. Hazard. Mater.* **2009***, 171*, 1045-1050.

(38) Thimsen, E.; Le Formal, F.; Grätzel, M.; Warren, S. C. Influence of Plasmonic Au Nanoparticles on the Photoactivity of Fe_2O_3 Electrodes for Water Splitting. *Nano Lett.* **2011***, 11*, 35-43.

(39) Thomann, I.; Pinaud, B. A.; Chen, Z.; Clemens, B. M.; Jaramillo, T. F.; Brongersma, M. L. Plasmon Enhanced Solar-to-Fuel Energy Conversion. *Nano Lett.* **2011***, 11*, 3440-3446.

(40) Xu, X.; Kyaw, A. K. K.; Peng, B.; Zhao, D.; Wong, T. K. S.; Xiong, Q.; Sun, X. W.; Heeger, A. J. A Plasmonically Enhanced Polymer Solar Cell with gold–silica core–shell Nanorods. *Org. Electron.* **2013***, 14*, 2360-2368.

(41) Gao, H.; Liu, C.; Jeong, H. E.; Yang, P. Plasmon-Enhanced Photocatalytic Activity of Iron Oxide on Gold Nanopillars. *ACS Nano* **2012***, 6*, 234-240.

(42) Warren, S. C.; Thimsen, E. Plasmonic Solar Water Splitting. *Energy Environ. Sci.* **2012***, 5*, 5133-5146.

(43) Hu, Y.; Kleiman-Shwarsctein, A.; Forman, A. J.; Hazen, D.; Park, J.; McFarland, E. W. Pt-Doped α-Fe_2O_3 Thin Films Active for Photoelectrochemical Water Splitting. *Chem. Mater.* **2008***, 20*, 3803-3805.

(44) Ling, Y.; Wang, G.; Wheeler, D. A.; Zhang, J. Z.; Li, Y. Sn-Doped Hematite Nanostructures for Photoelectrochemical Water Splitting. *Nano Lett.* **2011***, 11*, 2119-2125.

(45) Miao, C.; Shi, T.; Xu, G.; Ji, S.; Ye, C. Photocurrent Enhancement for Ti-Doped Fe_2O_3 Thin Film Photoanodes by an in Situ Solid-State Reaction Method. *ACS Appl. Mater. Interfaces* **2013***, 5*, 1310-1316.

(46) Sun, X.; Xu, F.; Li, Z.; Zhang, W. Cyclic Voltammetry for the Fabrication of High Dense Silver Nanowire Arrays with the Assistance of AAO Template. *Mater. Chem. Phys.* **2005***, 90*, 69-72.

(47) Riveros, G.; Green, S.; Cortes, A.; Gómez, H.; Marotti, R. E.; Dalchiele, E. A. Silver Nanowire Arrays Electrochemically Grown into Nanoporous Anodic Alumina Templates. *Nanotechnology* **2006***, 17*, 561-570.

(48) Sun, B.; Jiang, X.; Dai, S.; Du, Z. Single-Crystal Silver Nanowires: Preparation and Surface-Enhanced Raman Scattering (SERS) Property. *Materials Letters* **2009***, 63*, 2570-2573.

(49) Xiao, R.; Cho, S. I.; Liu, R.; Lee, S. B. Controlled Electrochemical Synthesis of Conductive Polymer Nanotube Structures. *J. Am. Chem. Soc.* **2007***, 129*, 4483-4489.

(50) Xu, C.; Li, H.; Zhao, G.; Li, H. Electrodeposition and Magnetic Properties of Ni Nanowire Arrays on Anodic Aluminum oxide/Ti/Si Substrate. *Appl. Surf. Sci.* **2006***, 253*, 1399-1403.

(51) Chu, S.; Wada, K.; Inoue, S.; Todoroki, S.; Takahashi, Y.; Hono, K. Fabrication and Characteristics of Ordered Ni Nanostructures on Glass by Anodization and Direct Current Electrodeposition. *Chem. Mater.* **2002***, 14*, 4595-4602.

(52) Cho, S. I.; Xiao, R.; Lee, S. B. Electrochemical Synthesis of Poly(3,4-Ethylenedioxythiophene) Nanotubes Towards Fast Window-Type Electrochromic Devices. *Nanotechnology* **2007***, 18*, 405705.

(53) Foong, T. R. B.; Sellinger, A.; Hu, X. Origin of the Bottlenecks in Preparing Anodized Aluminum Oxide (AAO) Templates on ITO Glass. *ACS Nano* **2008***, 2*, 2250-2256.

(54) Musselman, K. P.; Mulholland, G. J.; Robinson, A. P.; Schmidt-Mende, L.; MacManus-Driscoll, J. L. Low-Temperature Synthesis of Large-Area, Free-Standing Nanorod Arrays on ITO/Glass and Other Conducting Substrates. *Adv Mater* **2008***, 20*, 4470-4475.

(55) Byun, J.; Lee, J. I.; Kwon, S.; Jeon, G.; Kim, J. K. Highly Ordered Nanoporous Alumina on Conducting Substrates with Adhesion Enhanced by Surface Modification: Universal Templates for Ultrahigh-Density Arrays of Nanorods. *Adv Mater* **2010***, 22*, 2028-2032.

(56) Gu, W.; Liao, L. S.; Cai, S. D.; Zhou, D. Y.; Jin, Z. M.; Shi, X. B.; Lei, Y. L. Adhesive Modification of indium–tin-Oxide Surface for Template Attachment for Deposition of Highly Ordered Nanostructure Arrays. *Appl. Surf. Sci.* **2012***, 258*, 8139-8145.

(57) Li, X.; Dong, K.; Tang, L.; Wu, Y.; Yang, P.; Zhang, P. The Fabrication of Ag Nanoflake Arrays Via Self-Assembly on the Surface of an Anodic Aluminum Oxide Template. *Appl. Surf. Sci.* **2010***, 256*, 2856-2858.

(58) Jin, R.; Cao, Y.; Mirkin, C. A.; Kelly, K. L.; Schatz, G. C.; Zheng, J. G. Photoinduced Conversion of Silver Nanospheres to Nanoprisms. *Science* **2001***, 294*, 1901-1903.

(59) Liu, G.; Cai, W.; Kong, L.; Duan, G.; Lu, F. Vertically Cross-Linking Silver Nanoplate Arrays with Controllable Density Based on Seed-Assisted Electrochemical Growth and their Structurally Enhanced SERS Activity. *J. Mater. Chem.* **2010***, 20*, 767-772.

(60) Lee, C.; Syu, C. Electrochemical Growth and Oxygen Reduction Property of Ag Nanosheet Arrays on a Ti/TiO_2 Electrode. *Int J Hydrogen Energy* **2011***, 36*, 15068-15074.

(61) Chen, S.; Carroll, D. L. Synthesis and Characterization of Truncated Triangular Silver Nanoplates. *Nano Lett.* **2002***, 2*, 1003-1007.

(62) Kim, M. H.; Kwak, S. K.; Im, S. H.; Lee, J.; Choi, K.; Byun, D. Maneuvering the Growth of Silver Nanoplates: Use of Halide Ions to Promote Vertical Growth. *J. Mater. Chem. C* **2014***, 2*, 6165-6170.

(63) Sun, Y.; Wiederrecht, G. Surfactantless Synthesis of Silver Nanoplates and their Application in SERS. *Small* **2007***, 3*, 1964-1975.

(64) Park, S. H.; Shin, H. S.; Kim, Y. H.; Park, H. M.; Song, J. Y. Template-Free and Filamentary Growth of Silver Nanowires: Application to Anisotropic Conductive Transparent Flexible Electrodes. *Nanoscale* **2013***, 5*, 1864-1869.

(65) Park, S.; Shin, H.; Kim, Y.; Park, H.; Song, J. Filamentary One-Dimensional Nanocrystal Growth of Cu, AgCu, and Au in Ultra-Dilute Electrolytes. *J. Alloys Compounds* **2013***, 580*, 152-156.

(66) Ko, H.; Singamaneni, S.; Tsukruk, V. V. Nanostructured Surfaces and Assemblies as SERS Media. *Small* **2008***, 4*, 1576-1599.

CHAPTER 2

EXPERIMENTAL TECHNIQUES

2.1 Cyclic Voltammetry (CV)

CV is a measurement for studying electrochemical properties of an analyte in solution with a three-electrode system which is composed of a working electrode, a reference electrode, and a counter electrode. The potential applied on the stationary working electrode is linearly scanned back and forth and the current flowing between the working electrode and counter electrode is recorded. The potential starts from a point where no electrode reaction happens towards a position where the oxidation or reduction reactions occur. The back and forth scanning of potential can be proceeded for many times as desired. The current is plotted as a function of the potential applied on the working electrode to provide electrochemical information about redox reactions.

2.2 Mott–Schottky Plot

Mott-Schottky plot is a plot which is used to obtain fundamental properties of semiconductor–electrolyte system. It is based on the Mott-Schottky relationship:

$$\frac{1}{C_{SC}^2} = \frac{2}{e\,\varepsilon\,\varepsilon_0 N}\left(E - E_{FB} - \frac{kT}{e}\right)$$

where C_{SC} is the capacitance of the space charge region with the unit of $F \cdot m^{-2}$, ε is the dielectric constant of the semiconductor with the unit of F/m, ε_0 is the permittivity of free space 8.854×10^{-12} F/m, N is the donor density with the unit m^{-3}, E is the applied potential with a unit of V, E_{FB} is flatband potential with the unit of V, k is Boltzmann's constant 8.617×10^{-5} $eV \cdot K^{-1}$, T is

the temperature with unit of K, and e is the electronic charge 1.6×10^{-19} C. From the above equation, $1/C^2_{SC}$ is linear with the applied potential E with a slope which could be used to calculate the donor density N. The donor density generally is proportional to the conductivity of the semiconductor. The intersection on the potential axis determining the flatband potential. Flatband potential is an applied potential at which the Fermi energy of the semiconductor stays at the same energy level as the redox potential of the solution, which means there is no net charge transfer and hence there is no band bending. Fermi energy is the energy state that at which the possibility of being occupied by electrons is 0.5. So the flatband potential provides information about the position of the band edge of a semiconductor.

2.3 Photoelectrochemistry Test

A typical photocurrent test system for hematite thin film is exhibited in Figure 2.1. The testing system is using two electrodes or three electrodes depending on the demand. For a two electrode-system, a Pt wire is generally adopted as the counter electrode and the voltage and current is supervised by a Keithley Sourcemeter. When using a three-electrode system, the reference electrode is saturated calomel electrode (SCE) or Ag/AgCl, the counter electrode is usually a Pt wire, and the potential and current are managed by an electrochemical workstation. The light source, an Oriel AM 1.5 filtered Xenon Arc lamp, illuminates from back for the test of hematite thin film since the Fluorine-doped Tin Oxide (FTO) substrate is transparent and the hematite film is very thin. For measuring the photocurrent from Ag NRs and NWs, the light is chosen to come from the front in case they are prepared on opaque substrates. The wavelength of the incident light could be chosen by a monochromator which is an optical device that selectively transmits photons with a narrow band of wavelengths from the input light by using either the optical dispersion in a prism or a diffraction grating. The photocurrent or photocurrent density

(photocurrent divided by the active surface area of the sample) is plotted versus the wavelength of the incident light to generate action spectra for studying the wavelength dependent photoelectrochemical properties.

The action spectra can be used to obtain the IPCE which is defined as the ratio of the rate of photo-generated electrons versus the rate of incident photons as a function of wavelength. IPCE provides information about how efficient a device can be in converting the incident light into the electrical energy at a given wavelength. It is generally calculated by the following equation:

$$IPCE\ (\lambda) = \frac{electrons\ /cm^2/s}{photons\ /cm^2/s} = \frac{|j_{ph}| \times 1240\ (V \times nm)}{P_{mono} \times \lambda}$$

where j_{ph} is the photocurrent density obtained from the chronoramperometry experiment with a unit of mA/cm^2 at a given wavelength, P_{mono} is the light intensity at a given wavelength with a unit of mW/cm^2 which is measured by a calibrated silicon photodiode in this dissertation, and λ is the wavelength of the incident light with a unit of nm.

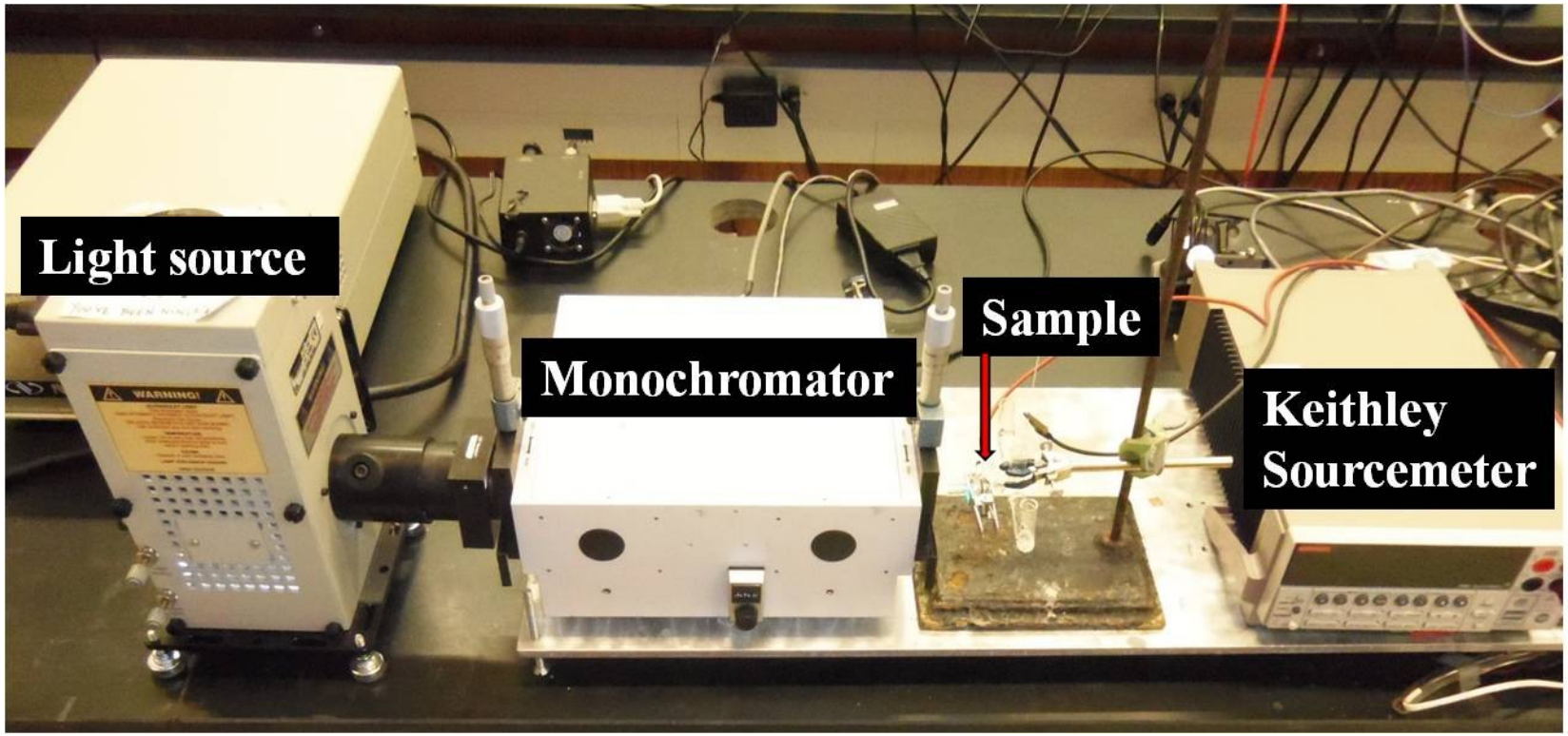

Figure 2.1 Photocurrent testing system.

2.4 Raman Spectroscopy

Raman Spectroscopy, named after the Indian physicist C. V. Raman, is spectroscopic tool based on the Raman Effect which provides information about molecular vibrations, rotations, and other low-frequency modes. It is complementary to Infrared Spectroscopy. Raman Effect describes a laser light interacting with a specimen, involving inelastic scattering of the light and resulting in the energy of the laser photons being shifted up (anti-Stokes) or down (Stokes). Energy-level states associated with Raman scattering are shown in Figure 2.2. The shift in energy shows 'fingerprint' information about the vibration of molecules of the sample and can be used for sample identification and quantitation. For a Raman-active transition, there must be a change in the polarizability of the molecule during the vibration and rotation, which means that the electron cloud of the molecule must undergo a positional change. Compared with the fluorescene measurement, Raman spectroscopy is capable of providing highly resolved vibrational information and does not suffer from the rapid photobleaching. Raman Effect is a very weak phenomenon which produces very small relative energy changes. Raman Spectroscopy is not practical until the advent of lasers which are very intense sources of monochromatic light.

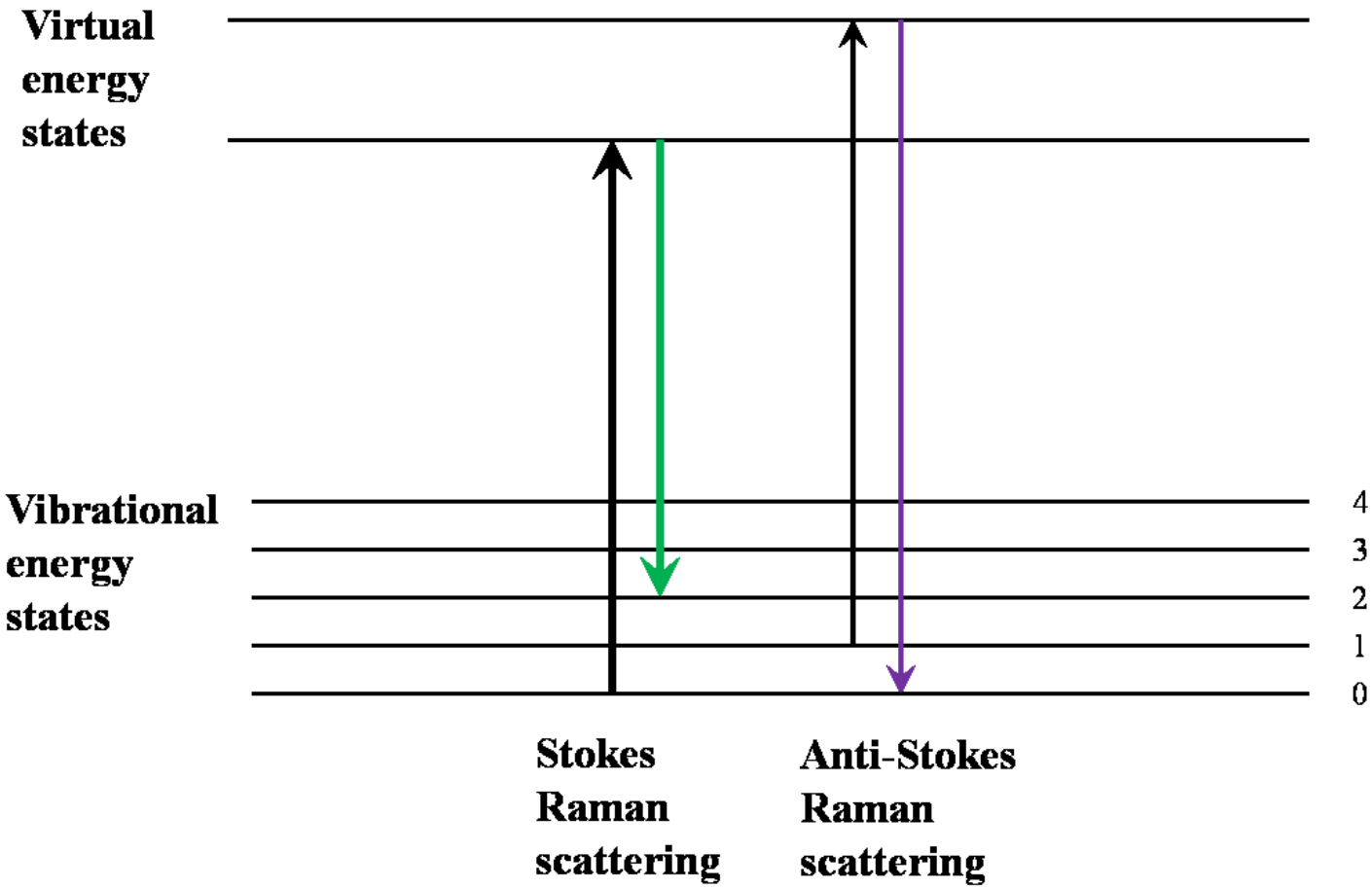

Figure 2.2 Energy-level states associated with Raman scattering.

2.5 SEM

SEM is a technique for imaging a sample through scanning the surface of the sample with a focused beam of high-energy electrons which are generated from a cathode filament and accelerated towards the specimen through applying a voltage. After the acceleration, electrons possess a significant amount of kinetic energy and then collide and interact with atoms in the specimen, producing a mixture of signals such as secondary electrons, backscattered electrons, and characteristics X-ray that contain the information about the surface topography and composition of the specimen. Low-energy secondary electrons (<50 eV) ejected from the k-shell of the specimen atoms by inelastic scattering interactions are the most common and valuable ones for the imaging mode which produce a resolution better than 1 nanometer. High-energy backscattered electrons are electrons originating in the electron beam that are reflected or back-scattered out of the specimen through elastic scattering interactions with atoms in the sample. The heavier element whose backscattered electron signal is stronger than that from a lighter element and appears brighter in the image, thus the contrast between areas provides information about the chemical compositions in the specimen. Characteristic X-rays are released subsequent to the inelastic collisions between the incident electrons and the electrons in the discrete orbitals of atoms in the sample. After the collision, an inner shell electron of the atoms is removed and then a higher energy electron from the outer shell fills the vacancy, giving off the energy difference in the form of X-rays which are used to analyze the sample composition as well as the quantities of each element inside.

2.6 Transmission electron microscopy (TEM)

TEM is an analytical technique conventionally producing two-dimensional, black and white images by using a focused beam of high energy electrons which partially pass through and

interact with an ultra-thin specimen in a high vacuum chamber. It achieves a significantly higher resolution than light microscopes and could provide information about the positions of atoms within the specimen because of the small de Broglie wavelength of electrons which is directly related to the speed of the electrons. The faster the electrons travel, the shorter the wavelength of the electrons and the higher the quality and more detailed of the images. In a sample, the thin areas where more electrons transmit through display brighter than the dense area and the brightness differences provide information on the shape, size, structure, and texture of the sample.

2.7 Ultra-Violet Visible (UV-Vis) Absorbance Spectra

When a white light composed of a broad range of radiation wavelengths in the ultraviolet, visible and infrared area passes through a material with color, characteristic wavelengths are partially absorbed. The absorption is aroused by the interaction between photons and the molecules composed of this material which usually contains π-electrons or non-bonding electrons that can be excited to higher energy anti-bonding molecular orbitals through absorbing the energy of photons in ultraviolet or visible light area. The longer the wavelength of light they absorb, the easier the electrons are excited, indicating a smaller energy gap between the ground state and the excited state. The perceived color of this material will be the complementary color to the wavelengths absorbed. UV-Vis Absorbance Spectra measure the absorption of radiation as a function of wavelength in the ultraviolet-visible spectral region. It obeys the Beer-Lambert's law:

$$A=\varepsilon bc$$

where A is the obtained absorbance, ε is the molar absorptivity or extinction coefficient, in unit of $M^{-1}\cdot cm^{-1}$, b is the light-path length through the sample in cm, and c is the sample

concentration in M. It allows the determination of the concentration of a solution without titration.

2.8 X-Ray Diffraction (XRD)

X-ray crystallography is a non-destructive technique for analyzing the structure of crystalline material since each crystalline solid exhibits a unique characteristic pattern when the incident X-rays are diffracted by the solid. X-ray is an electromagnetic radiation with an energy ranging from 120 eV to 120 keV which is generated from bombarding a metal target with a focused beam of high energy electron. The wavelength of X-ray is close to the distance between the crystal lattice which extends in all direction since its components are organized in a periodic way. Therefore, once the crystal is illuminated with X-ray, the diffraction happens. As shown in Figure 2.2, the constructive interference will occur and generate diffraction peaks at specific incident angles which satisfy Bragg's Law:

$$n\lambda=2d\sin\theta$$

where n is the order of the diffraction, λ is the wavelength of X-ray with a unit of nm, d is the space between the lattices in nm, and θ is the position of peak.

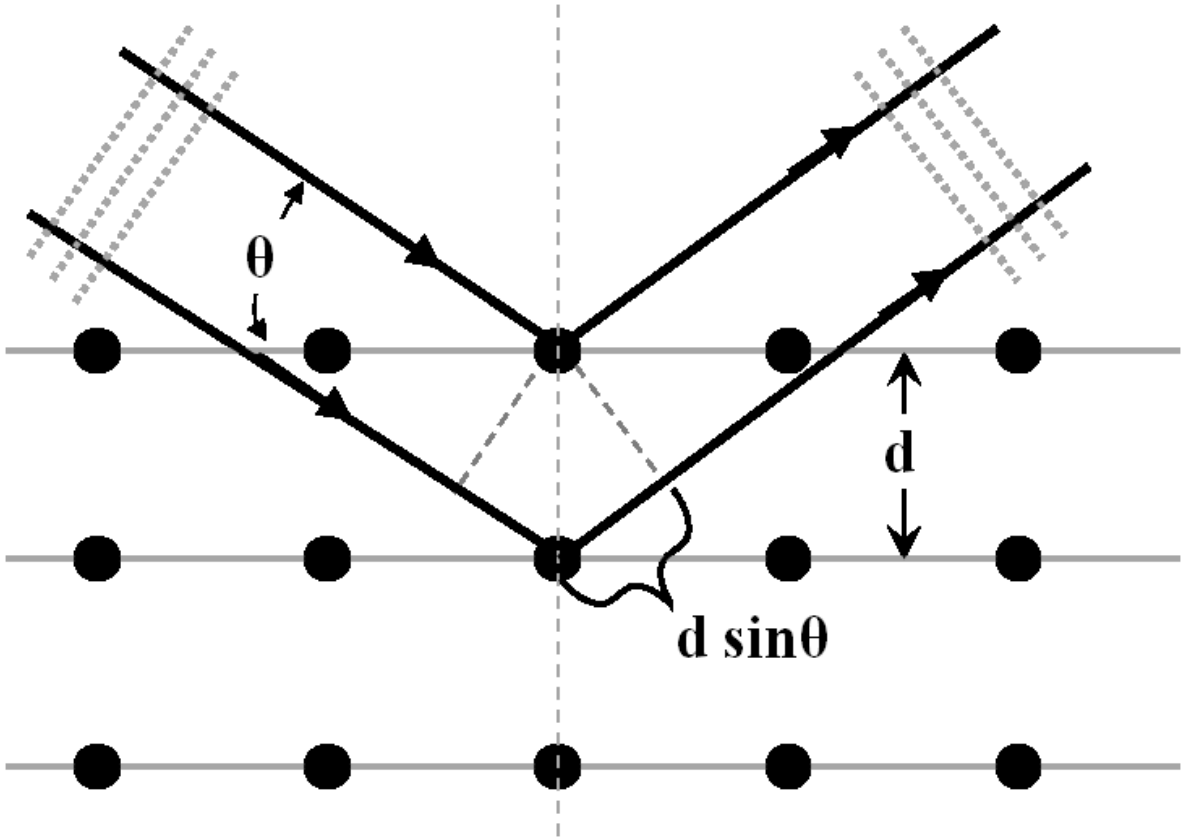

Figure 2.3 Schematic drawing of Bragg's law.

CHAPTER 3

GOLD NANOROD-ENHANCED LIGHT ABSORPTION AND PHOTOELECTROCHEMICAL PERFORMANCE OF HEMATITE

3.1 Introduction

Here we present a study of the plasmon effects of Au NRs, which are coated with CTAB bilayer to help prevent electron-hole recombination at gold surface,[1] on the light absorption and photoelectrochemical performance of a hematite thin film with various film thicknesses at two different electrode potential biases. In comparison to spherical nanoparticles, Au NRs have transverse plasmon bands and longitudinal plasmon bands at a longer wavelength, depending on their aspect ratio. Light scattering and absorption enhancement by Au NRs can be extended from the visible to the near infrared region by adjusting the aspect ratio of the NRs.

3.2 Experimental

3.2.1 Preparation of hematite photoanode

FTO glass substrates (15 mm ×15 mm, Pilkington) were washed in a sequence of deionized (DI) water, acetone, DI water, isopropanol, DI water, and then cleaned by UV-ozone (BioForce Nanosciences) for 15 minutes in each step. The FTO side of the glass substrate was then treated with a 2% titanium (IV) i-propoxide (Fisher Scientific) solution in isopropanol to increase the adhesion of α-Fe_2O_3 to the glass substrate. 1.64 M, 0.82 M, 0.33 M and 0.16 M iron (III) nitrate (ACROS) aqueous solutions were spin-coated onto FTO at two fixed rotation speeds, 400 rpm for 9 s and 4000 rpm for 30 s, respectively. The substrates were then dried on a hot plate

at 80 ºC. The prepared samples were heated at 600 °C in air for 3 hours to form α-Fe_2O_3 layer on FTO.[2] The concentration of $Fe(NO)_3$ was varied to adjust the thickness of α-Fe_2O_3 layer.

3.2.2 Preparation of gold NRs

120 µl of 10 mM freshly prepared ice-cold $NaBH_4$ (Fisher Scientific) solution was added to the mixed solution of 50 µl of 10 mM $AuCl_3$ in HCl and 1.5 ml 100 mM CTAB (99+% ACROS) to obtain a light brown gold seed solution. The seed solution was stored up to 2 hours prior to be used for Au NR growth. To prepare the growth solution for Au NRs, 250 µl 10 mM $AgNO_3$ (Fisher Scientific) and 270 µl 100 mM ascorbic acid solution (Fisher Scientific) were added to a mixed solution of 40 mL CTAB (100 mM) and 1.7 mL 0.1 M $AuCl_3$ in HCl successively, then 0.42 mL of the gold seed solution was added to the growth solution. The growth solution with seed was shaken for 15 s and then kept at 28 ºC for 16 h. CTAB serves as a capping agent and helps direct the formation of Au NRs. Excess CTAB was removed by centrifuging the Au NRs solution for four times and the final Au NR product was stored in DI water.

3.2.3 Modification of hematite thin film electrodes using gold NRs

150 µl 20 mM poly (4-styrenesulfonate) (PSS, Aldrich Chemical Company, average MW ca. 70,000) solution was spin-coated onto the surface of α-Fe_2O_3 electrode and then 150 µl of an Au NRs solution was dropped on top of the α-Fe_2O_3 side of the electrode immediately for Au NRs to self-assemble onto the surface through electrostatic interactions. After 16 hours, the α-Fe_2O_3 electrodes were washed with DI water for four times and dried with nitrogen.

3.2.4 Spectroscopic characterization

Action spectra of the α-Fe_2O_3 electrodes were carried out in 1.0 M NaOH using a programmed Keithley 2400 multimeter and a monochromator (MD-1000, Optical Building

Blocks Corp.) with an Oriel AM 1.5 filtered Xenon Arc lamp (Newport) as light source. A 400 nm long-pass filter was used for action spectra collection, and the full lamp intensity of 100 mW/cm^2 was used for photocurrent-potential measurement without using the monochromator. CV was obtained with Electrochemical Station (CH Instruments, Inc., Austin, TX). Absorbance spectra of solutions and films were obtained using a Varian Cary 50 UV-Vis spectrophotometer. A JOEL 7000 FE SEM and A FEI Tecnai F-20 TEM were used to characterize samples.

3.3 Results and Discussions

3.3.1 Surface enhancement experimental geometry and absorption spectra

To couple local field enhancement of the surface plasmon resonance of gold to a hematite layer, we used a configuration (denoted as top) as shown in Figure 3.1. The capping ligand CTAB for the Au NRs synthesis is not only naturally attached to the Au NRs to make them well dispersed in aqueous solution, but also provides positive charge on their surface to allow Au NRs to self-assemble onto the surface of a hematite electrode electrostatically should its surface be negatively charged in the presence of polyelectrolyte such as PSS.[3]

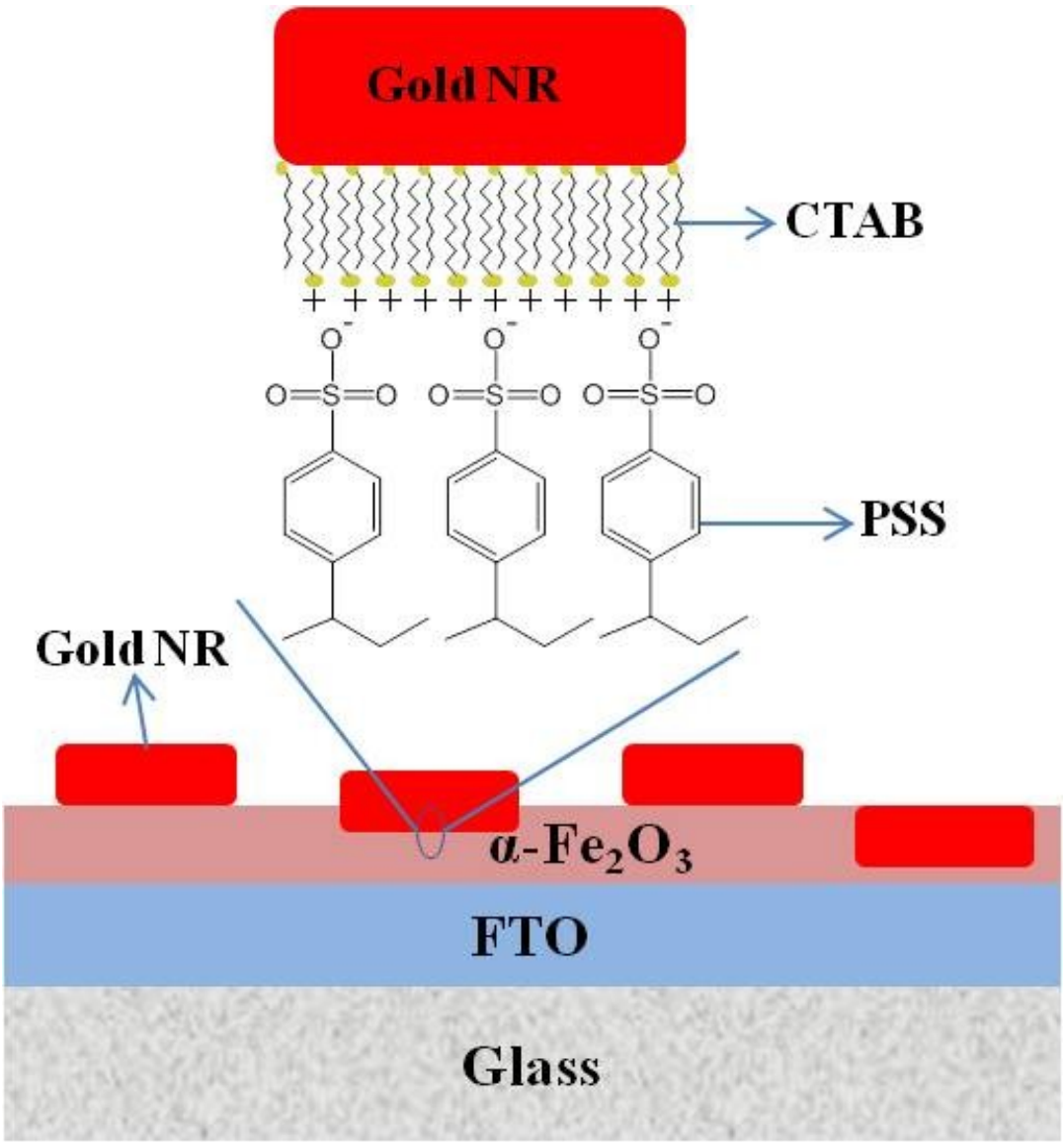

Figure 3.1 Schematic of Au NRs modified hematite thin film electrode on top of FTO glass in a top coating configuration through electrostatic interaction between CTAB modified Au NRs and negatively charged hematite surface. Adapted with permission from ref. [4].

Figure 3.2 illustrates the absorbance spectra of Au NRs in solution. There are two major peaks in the spectra. The peak near 500 nm is due to the transverse mode of plasmon resonance and the peak near 750 nm is referred to as the longitudinal mode of plasmon resonance. Figure 3.2 also shows that the Au NRs have very strong light absorbance with the wavelengths larger than 600 nm in comparison to the absorption of the hematite film. When coupling Au NRs to a thin film electrode of α-Fe_2O_3 in the top configuration (Figure 3.1), one would expect the surface plasmon enhanced light absorption of α-Fe_2O_3 to be in the near infrared range. However, the surface plasmon is very sensitive to coupling between Au NRs as they become close to each other when self-assembled onto a hematite surface with high coverage. The plasmon peak position and intensity are expected to be different from the one shown in Figure 3.2.

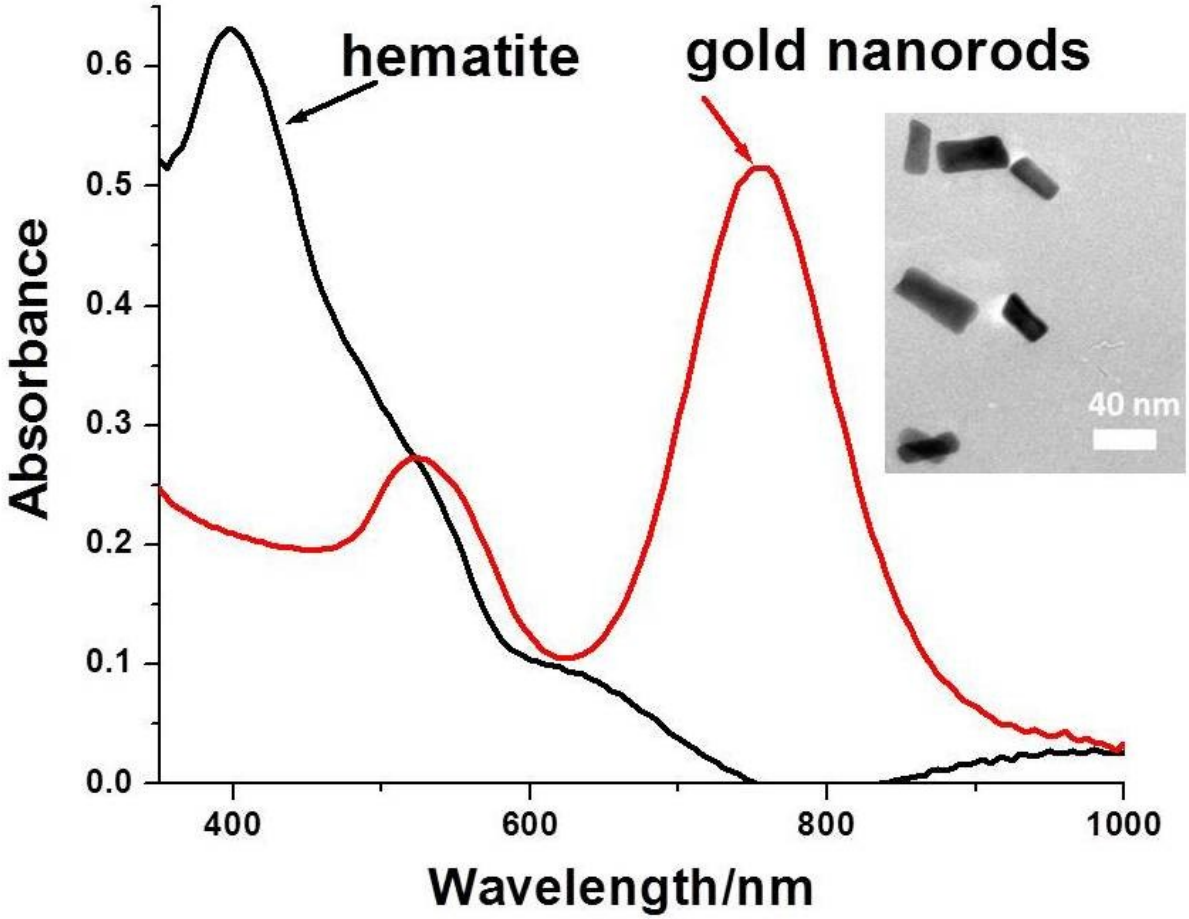

Figure 3.2 Absorbance spectra of Au NRs solution prior to being coated onto hematite electrode in comparison to the absorption of hematite film. Inset is a typical TEM image of Au NRs. Adapted with permission from ref. [4].

The synthesis of Au NRs using a seeding method has been well explored in the literature.[5] Their size and aspect ratio can be easily tuned to change the light absorption wavelength and intensity. This provides a great opportunity for plasmon tunable photoelectrochemical systems in a wide wavelength range. The surface capping ligand CTAB for growing Au NRs serves three purposes. (1) It helps to prevent Au NRs from agglomeration. (2) The CTAB bilayer on gold surface provide positive charges that can anchor gold nanords onto a negatively charge hematite surface. (3) CTAB serves as a dielectric layer (Figure 3.1) to prevent charge recombination for charge carriers in hematite which decreases photoelectrochemical efficiency for the water oxidation reaction. Au NRs obtained using our synthesis approaches have an average diameter of 12 nm and average length of 45 nm as shown in the inset of Figure 3.2.

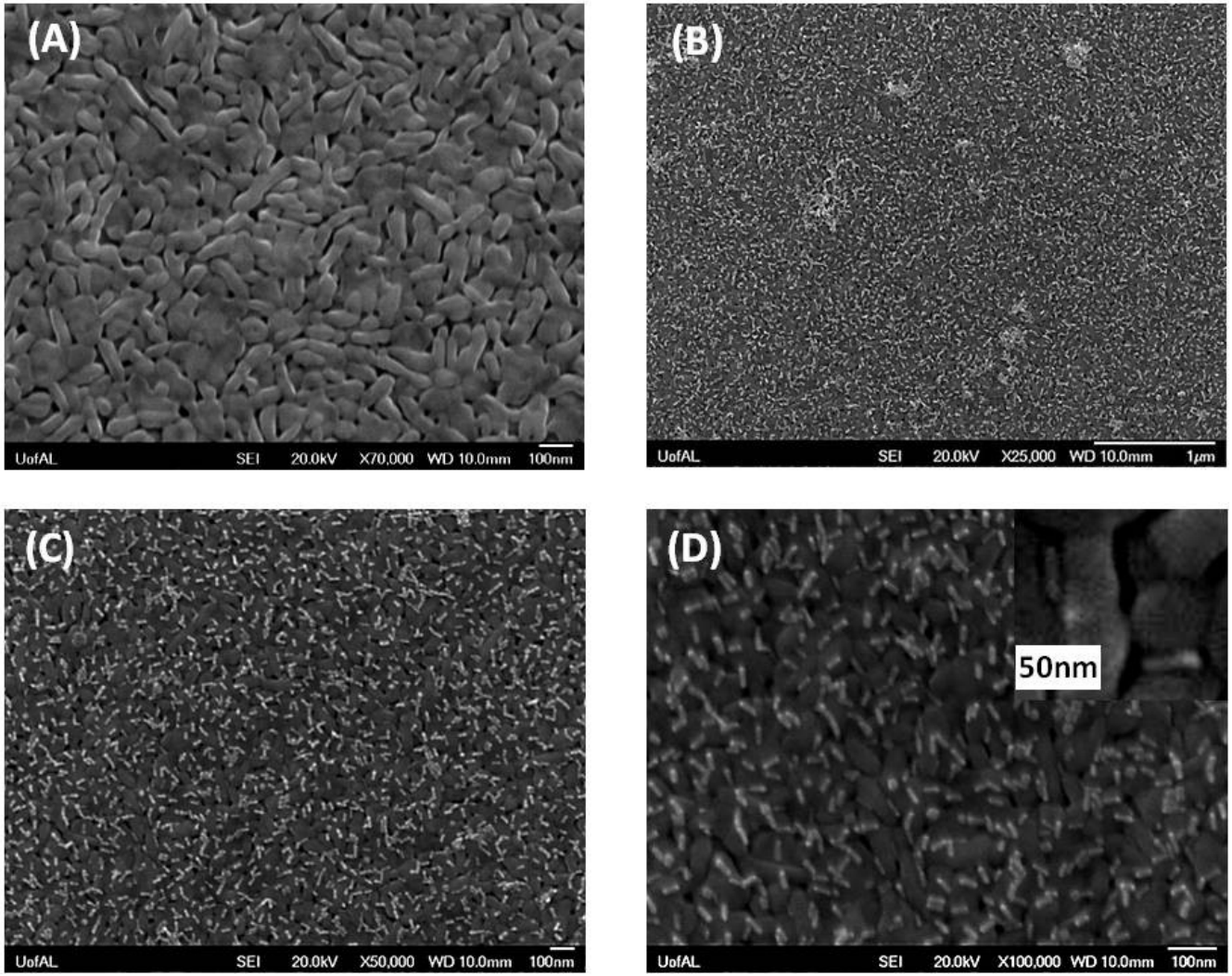

Figure 3.3 Characterization of sample surface morphology (A): SEM image of hematite electrode surface. (B): Au NRs modified hematite electrode with different magnification. (C) and (D) are zoom-in images of panel B. Adapted with permission from ref. [4].

3.3.2 Characterization of sample surface morphology and α-Fe_2O_3 film thickness control

Figure 3.3 shows a typical SEM image of a bare hematite surface and images of Au NRs spontaneously adsorbed onto the hematite electrodes. The α-Fe_2O_3 electrode made from the decomposition of $Fe(NO_3)_3$ forms an amorphous phase of hydrous iron oxide via hydrolysis reactions which can then form anhydrous a-Fe_2O_3 at 600 ºC. The α-Fe_2O_3 layer shows a densely packed nanostructures with longitudinal domains of about 100 nm in length and 50 nm in width. Figures 3.3 B, C and D are SEM images of an α-Fe_2O_3 electrode modified with Au NRs. All samples show a similar quality of coating. NRs with narrow size and aspect ratio distribution were obtained by centrifuging the Au NRs in their growth solution four times before self-assembling them onto the surface of hematite to prevent the presence of spherical gold nanoparticles on α-Fe_2O_3 film. Au NRs are well distributed on the α-Fe_2O_3 film due to the strong interaction between the positively charged surfaces of Au NRs and the negatively charged surfaces of hematite. Some Au NRs occupy the sites of the interstitials in the nanostructured domains of α-Fe_2O_3 particles as shown by the high resolution SEM image (Figure 3.3D). Aggregations of Au NRs also appear on the surface due to the destruction of the surface charge by PSS and high coverage of Au NRs on hematite's surface.

To understand how Au NR self-assembling affects the light absorption and photoelectrochemical performance of hematite thin film electrode, the thickness of the underlying hematite layer needs to be controlled. This is because field-enhancement of Au NRs is a distance dependent process. The absorption of the hematite layer within the local field of the Au NRs can be enhanced; such a local field enhancement distance is usually less than 10 nm. Therefore only a small plasmon enhancement effect is expected for very thick hematite layer, and significant plasmon enhancement is expected for a thin hematite electrode with a thickness

less than 10 nm. The absorbance spectra of an α-Fe_2O_3 film on an FTO substrate prepared by different concentrations of $Fe(NO)_3$ were measured. The thickness of the hematite layer is controlled by adjusting the concentration of $Fe(NO)_3$. The thickness of a relative thick hematite film prepared by spin coating 1.64 M iron (III) nitrate was measured by SEM. According to Lambert–Beer law, the absorption coefficient of hematite film was calculated to be 0.0032 nm^{-1} at 500 nm, close to the literature value 0.005 nm^{-1}.[6] Because there is a layer of 300 nm FTO substrate with a rough surface, it is impractical to measure the thicknesses of thinner films either by SEM or profilometer, their thicknesses are calculated by using the obtained absorption coefficient (0.0032 nm^{-1}) from the relative thick film. The calculated optical thickness of the resulting α-Fe_2O_3 film and corresponding concentration of $Fe(NO)_3$ are listed in Table 3.1. All α-Fe_2O_3 films show an absorbance onset around 600 nm as shown in Figure 3.2, corresponding to a band gap of 2.08 eV. There is a strong peak around 390 nm attributable to $O^{2-} \rightarrow Fe^{3+}$ charge transfer from O_{2p} nonbonding orbitals to lowest empty metal d orbitals.[7]

Sample	A at 500 nm	Thickness (nm)	i_{dark} (μA)	i_{photo} (μA)	$\lvert i_{photo} - i_{dark} \rvert$ (μA)
1	0.38524	120.4	2.567	-84.950	87.517
2 (Au NR)	0.31667	99.0	-8.78	-109.50	100.72
3	0.20623	64.4	1.25	-54.37	55.62
4 (Au NR)	0.18917	59.1	-11.47	-76.30	64.83
5	0.07140	22.3	-8.04	-35.05	27.01
6 (Au NR)	0.07023	22.0	-30.52	-46.18	15.66
7	0.02920	9.1	-18.53	-29.59	11.06
8 (Au NR)	0.02677	8.4	-37.90	-49.76	11.86

Table 3.1 Estimated thicknesses of α-Fe_2O_3 thin films, optical absorbance A at 500 nm, and the corresponding dark- and photo-current at 0.5 V vs. Ag/AgCl in the presence and absence of Au NRs in a top configuration. Adapted with permission from ref. [4].

Figure 3.4A illustrates the absorbance spectra of α-Fe_2O_3 films with different thicknesses before and after coating with Au NRs. Hematite films with Au NRs show absorption peaks around 775 nm which are attributed to the surface plasmon of Au NRs. This plasmon peak position and shape is different from the one in Figure 3.2, because of strong plasmon coupling of Au NRs in the solid state on a hematite surface, and changes in their surrounding environment in comparison to Au NRs in aqueous solution. To better resolve the influence of Au NRs on α-Fe_2O_3 films with different thicknesses, the absorbance spectra are normalized at a peak value around 400 nm and the result is shown in Figure 3.4B. The absorbance of α-Fe_2O_3 is broadened by Au NRs from 400 nm to 600 nm. Relative plasmon absorbance increases as the hematite film thickness decreases. We expect to observe a significant plasmon enhancement effect for ultra-thin hematite layers because the plasmon effect will play a major role when a hematite layer can sufficiently experience the local field enhancement in the presence of gold.[8]

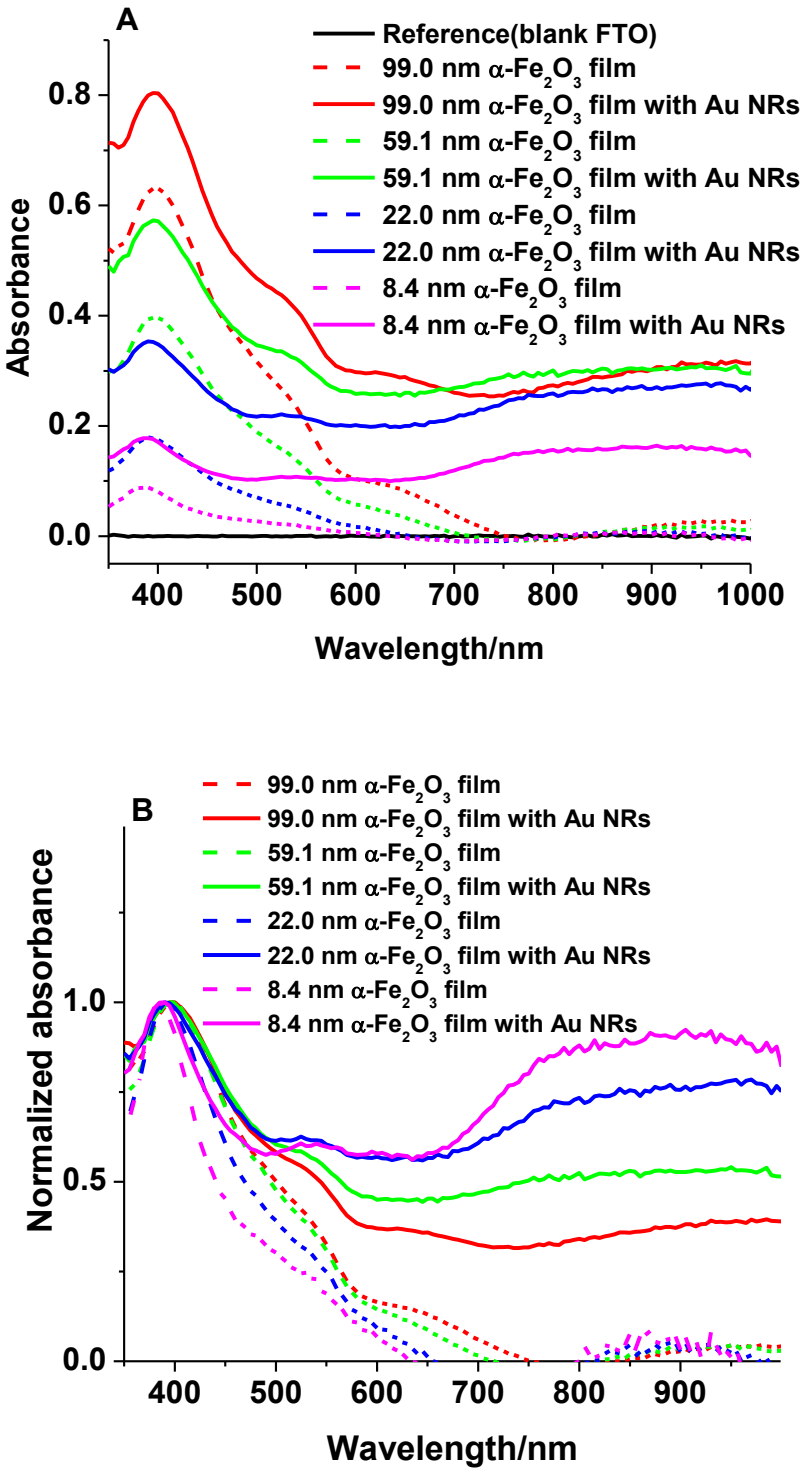

Figure 3.4 (A): Absorbance spectra of α-Fe_2O_3 electrode film before and after coating with Au NRs on the surface; (B): Normalized absorbance spectra of α-Fe_2O_3 film at 400 nm before and after coating with Au NRs. Adapted with permission from ref. [4].

3.3.3 Surface enhanced photocurrent dependence on excitation wavelength and electrode potential

Figure 3.5 presents the effects of Au NRs on the CV of α-Fe_2O_3 thin film electrodes in the dark and the CV of electrodes illuminated with a simulated 1.5 AM white light (100 mw/cm^2). The onset potential of water oxidation in the dark and under visible irradiation is lower in the presence of Au NRs than for pristine α-Fe_2O_3 film, suggesting a favorable charge transfer rate for water oxidation at Au NRs thank prinstine hematite layer. This result is consistent with other studies on Au NRs.[9] For an α-Fe_2O_3 film with optical thickness less than 25 nm, an oxidation peak appeared around 0.55 V (vs. Ag/AgCl). This is due to the oxidation of OH^- directly on the FTO substrate where is not completely covered by hematite layer. Table 3.1 summarizes the dark current and photo current of α-Fe_2O_3 thin film electrodes with and without Au NRs at 0.5 V. The bias 0.5 V (vs. Ag/AgCl) is important to withdraw electrons from hematite to FTO to prevent recombination of holes and electrons at the surface of Au NRs. Photocurrent enhancement is significant for hematite electrodes with thicknesses of 59.1nm and 99 nm, and the dark current of these thick films are low in comparison to those of thin hematite electrodes. The dark current density is high for thinner hematite layers due to pinholes in the thin films and the background is enhanced by Au NRs because of their good conductivity. The CTAB bilayer on Au NRs is not particularly stable in high pH solution as it is susceptible to being oxidized or desorbed from the Au NR surface. Therefore it would not serve as a good insulating layer to prevent charge recombination. Such an enhanced background current would cause efficient electron hole recombination[10] when the hematite electrodes are illuminated with light, yielding no photocurrent enhancement. This indicates that the ultra-thin layer of the α-Fe_2O_3 film has to be pinhole free to minimize the background dark current in order to obtain a significant photocurrent enhancement as compared to the thick hematite layer.

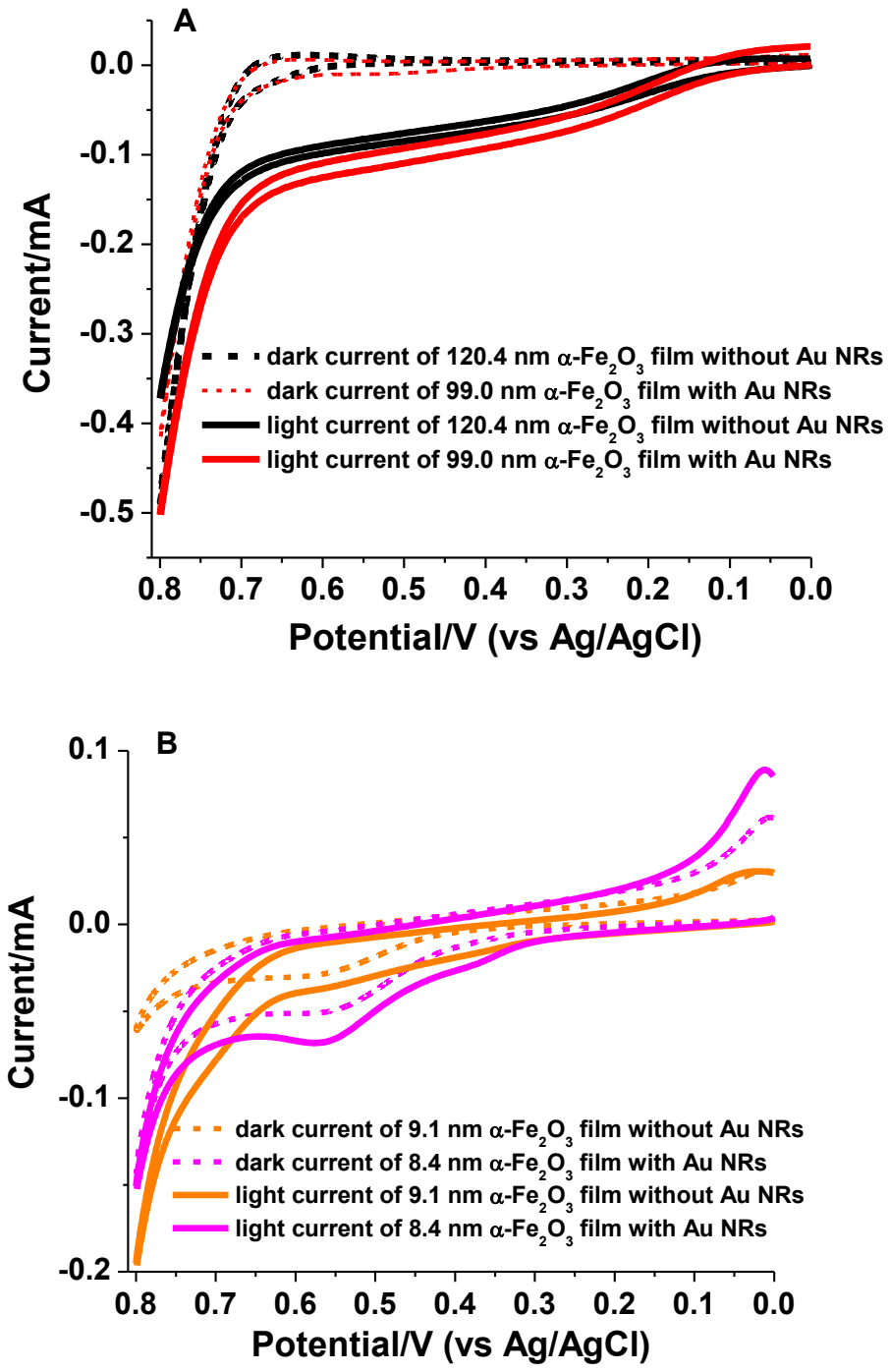

Figure 3.5 (A): Comparison of dark current and light current response of α-Fe_2O_3 thin film electrodes with thickness of 120.4 nm without Au NRs and 99.0 nm with Au NRs; (B): Comparison of dark current and light current response of α-Fe_2O_3 thin film electrodes with thickness of 9.1 nm without Au NRs and 8.4 nm with Au NRs. Active surface area is 0.18 cm^2. Adapted with permission from ref. [4].

To observe the influence of Au NRs on the photoelectrochemical properties of α-Fe_2O_3, the wavelength dependence of the photocurrent at two different electrode potentials was investigated. The action spectra shown in Figure 3.6 show the effect of coating of Au NRs on the photocurrent of α-Fe_2O_3 film with various thicknesses. This experiment was done in 1 M NaOH with the electrode potential of 0.2 V (vs. Ag/AgCl, Figure 3.6A) and 0.5 V (vs. Ag/AgCl, Figure 3.6 C) on the photoelectrode and using platinum wire as the counterelectrode. The electrode potential at 0.5 V is used to prevent the recombination of holes and electrons as described previously. The action spectra results show that all photocurrent responses track the absorption of hematite (cf. Figure 3.4A). At a bias potential of 0.2 V, the photocurrent of α-Fe_2O_3 with Au NRs is lower than that of the α-Fe_2O_3 electrode without Au NRs. This is due to the increased recombination of holes and electrons because electrons will be injected to the gold in the absence of an external bias high enough to help separate the photo-induced charge pairs. Meanhwhile, it should be noted that the background current in the action spectra is increased because of the improved conductivity of having Au NRs on the surface, yielding a high double layer charging current density and faradiac current from direct OH^- oxidation. To observe the surface plasmons effects, all action spectra are normalized at the peak value around 410 nm in Figure 3.6B. The action spectra of all hematite films are greatly broadened in the region from 400 nm to 600 nm in the presence of Au NRs. The action spectra broadening effect is greatly enhanced for thinner hematite film due to the strong plasmon coupling between gold and hematite layer when the thickness is close to 10 nm. From 600 nm to 800 nm, the samples with have a higher background current and the background current increases as the thickness of the hematite decreases. This is caused by increased defects in the hematite layer for thin hematite layers, and these defects expose the surface of the FTO substrate to increase its double layer charging current and faradic

current from oxidation of OH^-. To further show that the trend of wavelength dependence of photocurrent on plasmon of Au NR are not affected by the double layer charging current, we scanned the excitation wavelength backward from 800 nm to 400 nm and obtained the same results as that received by scanning from 400 nm to 800 nm.

Figure 3.6C shows the action spectra under a bias of 0.5 V where one would expect a dramatic increase in background current and a pronounced photoelectrochemical effect as shown in Figure 3.5. Clearly the current density of gold modified hematite electrode at this potential is higher than that of pristine hematite film. The enhancement is two-fold. First, the presence of Au NRs increases the background current as shown in Figure 3.6 because gold is a better conductor than hematite and the Au NRs bridge the gap of hematite and solution to pass double layer charging at the FTO-Au NRs surface. Second, the normalized action spectra indicate that the plasmonic effect broadens the photocurrent response near the resonance wavelength because the light absorption cross section of the hematite electrode is increased. For ultrathin hematite layers the plasmonic broadening effect is more significant than in the thick film because of the close distance of hematite layer to the plasmonic field. However, the background current increased as well because of increased defect sites in the thin hematite layer to conduct current directly when FTO is not covered by the hematite layer. More current response is expected in the presence of Au NRs because the gold is a better conductor and improves double layer charging effect. Improved results can be obtained by decreasing the density of pin holes and defect sites in hematite layer to receive low background current for significant photocurrent enhancement observation.

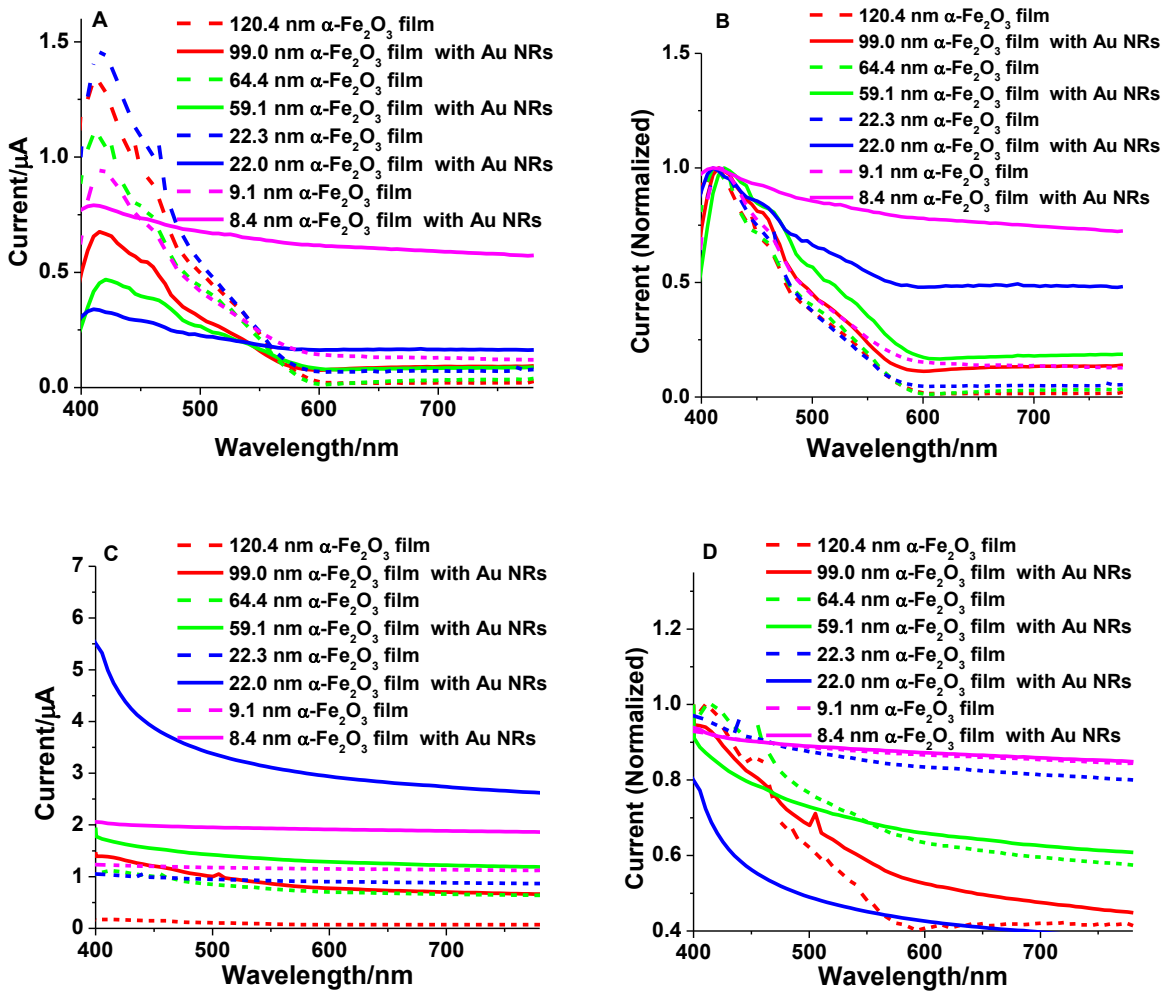

Figure 3.6 (A): Effect of Au NRs coating on action spectra of α-Fe_2O_3 thin film electrodes with various thicknesses; (B): Effect of Au NRs coating on normalized action spectra of photocurrent of α-Fe_2O_3 thin film electrodes with various thickness. Hematite electrode is held at 0.2 V versus Pt counter electrode. Incident light wavelengths were scanned from 400 nm to 800 nm. (C) shows action spectra of the electrodes biased at 0.5 V versus Pt counter electrode, and (D) is the normalized action spectra. Active surface area is 0.18 cm^2. Adapted with permission from ref. [4].

3.3.4 Local field calculation for understanding plasmon enhanced photocurrent by Au NRs

To further understand the local field enhancement of light absorption of hematite by Au NRs, the local field produced by a single Au NR due to a strong interaction between the surface plasmon and incident electromagnetic wave is calculated with the the "discrete dipole approximation" (DDA) method[11] using the DDSCAT 7.1 program.[12] Figure 3.7 shows the local field intensity of a single Au NR when it is attached to the surface of a hematite thin film when its surface plasmon is excited at 633 nm with the polarization direction along its longitudinal and transverse directions. The calculations show that the local field intensity is quite sensitive to the polarization angle of the incident light, and not all polarization angles can cause a constructive contribution to the local field intensity. It also suggests that the highest local field intensity is found in a range of less than 10 nm. This distance is very close to the surface of Au NRs when the polarization angle is along the longitudinal axis of the nanorod. Such a short enhancement distance does not change much when the nanorod is on top of the hematite layer, or buried inside the hematite layer. An Au NR in hematite has a much smaller enhancement cross section due to the plasmon damping in the presence of the high dielectric constant hematite layer. Our simulation results also suggest that incident light polarization dependence of the photocurrent enhancement upon plasmonic antenna modification should be addressed in future studies.

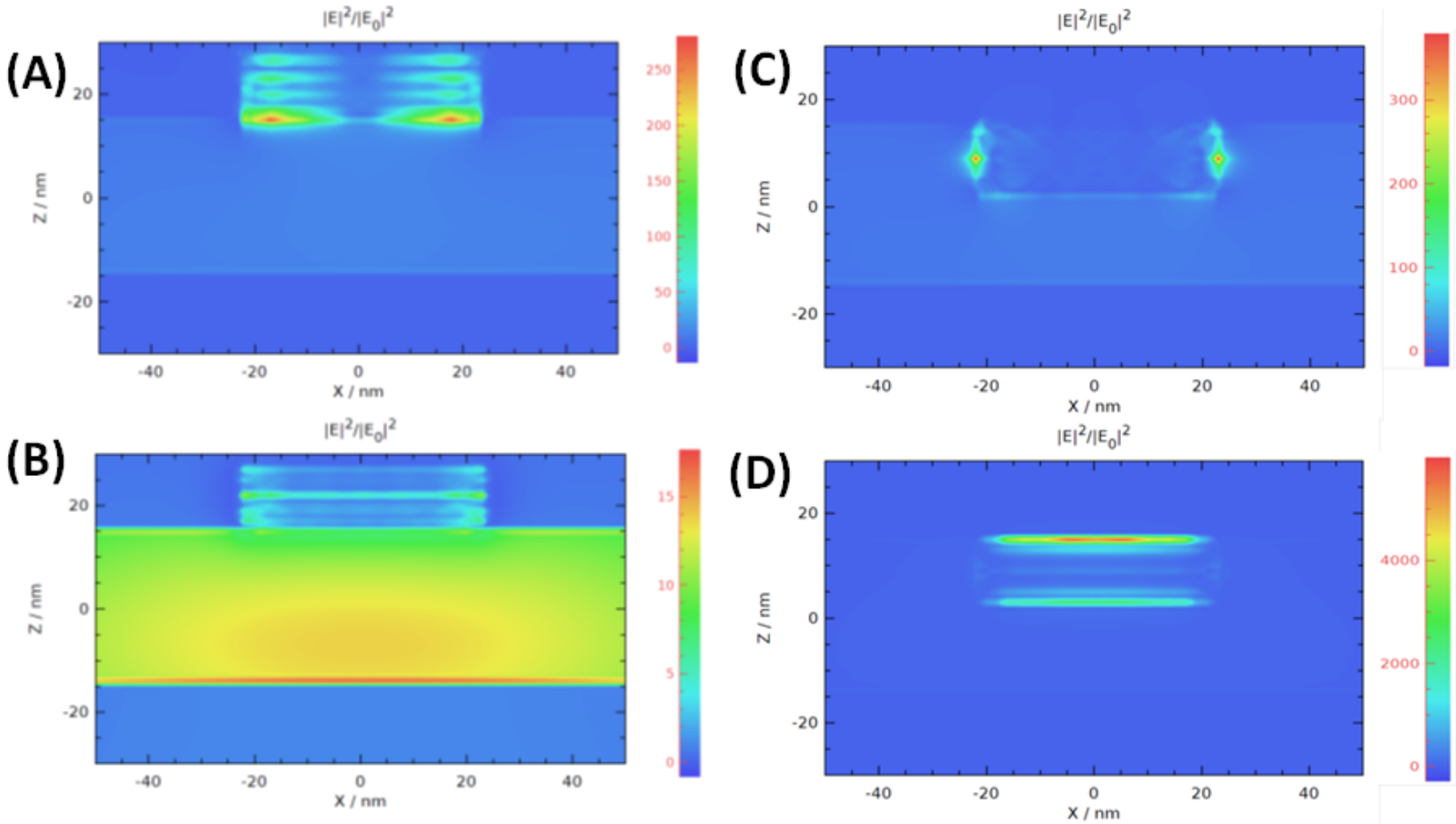

Figure 3.7 Calculated local field intensity around a Au NR with size of 45 nm in length and 12 nm in its diameter on top of a 50 nm thick hematite film. The gold nanoparticle and the hematite substrate are meshed to 1 × 1× 1 nm ^{3} cubic as one dipole and the local field intensity is calculated using discrete dipole approximation method. (A) and (B) are the local field intensity map in the x-z plane around a nanorod with incident light polarization direction along the longitudinal and transverse directions of the single nanorod, respectively. (C) and (D) are the calculated local field intensity distribution in the x-z plane of a Au NR buried 12 nm in depth inside a hematite thin film when the polarization direction of the incident light is along the longitudinal and transverse directions of the single nanorod, respectively. Adapted with permission from ref. [4].

3.4 Conclusions

Surface enhanced photoelectrochemical response of hematite electrode by Au NRs depends on hematite layer thickness. The plasmon enhancement process yields action spectra broadening and increases in the plasmon resonance wavelength region. Such a spectra broadening increases when the hematite electrode thickness decreases. No plasmon enhancement on photocurrent efficiency is observed at low electrode bias of 0.2 V (vs. Ag/AgCl), which is near the rest potential of the photoanode, due to the increased recombination of holes and electrons. A large amplitute of the electrode bias of 0.5 V (vs. Ag/AgCl) helps surface enhanced photocurrent collection. Our study suggests that surface plasmon effect can be obtained by insulating the Au NRs and preparing defect-free ultra-thin layer of α-Fe_2O_3 with thickness around 10 nm. This concept can be extended to other photocatalytic electrodes and other metallic plasmon sources such as silver by enhancing a thin layer of photocatalyst with enhanced plasmon light absorption cross-section, yielding efficient charge collection and transport in a short distance.

REFERENCES

(1) Pérez-Juste, J.; Liz-Marzán, L. M.; Carnie, S.; Chan, D. Y. C.; Mulvaney, P. Electric-Field-Directed Growth of Gold Nanorods in Aqueous Surfactant Solutions. *Advanced Functional Materials* **2004***, 14*, 571-579.

(2) Cesar, I.; Sivula, K.; Kay, A.; Zboril, R.; Grätzel, M. Influence of Feature Size, Film Thickness, and Silicon Doping on the Performance of Nanostructured Hematite Photoanodes for Solar Water Splitting. *J. Phys. Chem. C* **2009***, 113*, 772-782.

(3) Gole, A.; Stone, J. W.; Gemmill, W. R.; zur Loye, H.; Murphy, C. J. Iron Oxide Coated Gold Nanorods: Synthesis, Characterization, and Magnetic Manipulation. *Langmuir* **2008***, 24*, 6232-6237.

(4) Wang, J.; Pan, S.; Chen, M.; Dixon, D. A. Gold Nanorod-Enhanced Light Absorption and Photoelectrochemical Performance of α-Fe_2O_3 Thin-Film Electrode for Solar Water Splitting. *J. Phys. Chem. C* **2013***, 117*, 22060-22068.

(5) Johnson, C. J.; Dujardin, E.; Davis, S. A.; Murphy, C. J.; Mann, S. Growth and Form of Gold Nanorods Prepared by Seed-Mediated, Surfactant-Directed Synthesis. *J. Mater. Chem.* **2002***, 12*, 1765-1770.

(6) Souza, F. L.; Lopes, K. P.; Nascente, P. A. P.; Leite, E. R. Nanostructured Hematite Thin Films Produced by Spin-Coating Deposition Solution: Application in Water Splitting. *Solar Energy Mater. Solar Cells* **2009***, 93*, 362-368.

(7) Marusak, L. A.; Messier, R.; White, W. B. Optical Absorption Spectrum of Hematite, αFe_2O_3 Near IR to UV. *Journal of Physics and Chemistry of Solids* **1980***, 41*, 981-984.

(8) Moskovits, M. In Surface-enhanced Raman Scattering: Physics and Applications; Kneipp, K., Moskovits, M., Kneipp, H., Eds.; Topics in Applied Physics; Springer: Berlin, Germany, 2006.

(9) Thimsen, E.; Le Formal, F.; Grätzel , M.; Warren, S. C. Influence of Plasmonic Au Nanoparticles on the Photoactivity of Fe_2O_3 Electrodes for Water Splitting. *Nano Lett.* **2011***, 11*, 35-43.

(10) Hisatomi, T.; Dotan, H.; Stefik, M.; Sivula, K.; Rothschild, A.; Grätzel, M.; Mathews, N. Enhancement in the Performance of Ultrathin Hematite Photoanode for Water Splitting by an Oxide Underlayer. *Adv Mater* **2012***, 24*, 2699-2702.

(11) Draine, B. T.; Flatau, P. J. Discrete-Dipole Approximation for Scattering Calculations. *Journal of the Optical Society of America A: Optics and Image Science, and Vision* **1994***, 11*, 1491-1499.

(12) Draine, B. T.; Flatau, P. J. User Guide for the Discrete Dipole Approximation Code DDSCAT 6.1. **2004**.

CHAPTER 4

TEMPLATE-FREE ELECTROCHEMICAL DEPOSITION OF VERTICALLY STANDING METALLIC PLASMONIC STRUCTURES FOR SURFACE ENHANCED CATALYTIC APLLICATIONS

4.1 Introduction

To avoid the problems of top configuration of surface enhancement using Au NRs as mentioned in Chapter 3, vertically standing plasmonic structures (e.g., Ag NRs and NWs) are needed as described in this chapter. They are supposed to be in good contact with the substrate and the highly conductive plasmonic nanostructure will transport the electrons from photocatalytic top layer rapidly to decrease the charge recombination events for improved photoelectrochemical performance.

Ag NRs and NWs were successfully prepared using a newly invented template-free method in a two-electrode system. Planer cathode and anode electrodes parallel to each other were used to create a uniform electric field between the two electrodes for homogeneous growth of NRs and NWs over the entire cathode surface. This method is not constrained by the size of the cathode substrate as long as the anode is larger than the cathode; therefore scale-up of the production of vertically standing NRs and NWs using this technique now can be easily achieved in single batches of electrodeposition without using any sacrificial template. The type of cathode substrates can be flexible to allow for desired customization of nanomaterials to be fabricated. Herein, fabrication of vertically standing Ag NRs and NWs are presented with substrates such as FTO glass, ITO glass, and n-type Si. Fe NRs can also be electrodeposited on ITO substrate. Based on the experiment results, a growth mechanism is proposed.

In addition, Ag NRs and NWs typically exhibit both transverse and longitudinal plasmon resonance modes, which would enhance the absorbance of photocatalyst in a broad wavelength range. These Ag NRs and NWs could be attractive for application in photocatalysis and SERS. The effect of the surface plasmon of Ag NRs and NWs on the photocatalyts and SERS are presented in this chapter with emphasis of the effect of longitudinal mode of surface plasmon using a polarized light.

4.2 Experimental

4.2.1 Fabrication of vertically standing metal NRs and NWs

The conductive substrates were sonicated sequentially in DI water, acetone, isopropanol, and DI water for 15 minutes. Samples were dried using a nitrogen stream and then kept under UV ozone for 15 minutes. 50 µL 2% (v/v) titanium (IV) isopropoxide in isopropanol was spin coated on FTO substrate and then the samples were annealed in air at 500 °C for 30 minutes to convert titanium (IV) i-propoxide to TiO_2 in order to smooth the rough FTO surface. The pre-coating of TiO_2 was not applied for ITO glass and n-type Si substrates. The electrodeposition of Ag was carried out in a 10^{-4} M $AgNO_3$ aqueous solution with a two-electrode system under a 5 V direct current (DC) voltage for various hours (H). 7.0 V and 10^{-4} M $Fe(NO_3)_3$ were adopted for Fe deposition. The clean substrates served as working electrodes and a large piece of ITO glass worked as an anode. The two electrodes are set parallel to each other with a distance optimized to 3 cm. The size of the anode and cathode could be altered upon the needs as long as the anode is larger than the cathode that an even electric field could be maintained between the two electrodes. When it reached the designated time, the power source was turned off and samples were washed with DI water and dried in air.

4.2.2 Chemical Bath Deposition (CBD) of Cds on Ag NRs and NWs

0.25 mL 0.1 M cadmium acetate (Alfa Aesar) was added to 3.75 mL 0.2 M triethanolamine (Alfa Aesar). Then 0.025 mL 30% (wt) ammonia aqueous solution (ACROS) and 0.2 mL 0.2 M thiourea (Alfa Aesar) were added to the mixture sequentially and stirred for 5 minutes to blend them well at room temperature. Insert Ag NRs and NWs on ITO substrate and bare ITO substrate into the above-mentioned mixture and let it stay for 3 minutes. The above mixture was heated 70°C in a water bath for depositing CdS onto Ag nanostructured substrates.

4.2.3 Characterization

Ag NRs and NWs were characterized using A JOEL 7000 field emission scanning electron microscopy. Absorbance spectra of solutions and films were acquired using a Varian Cary 50 UV-Vis spectrophotometer. Raman measurements were carried out using a spectrometer (Jobin Yvon, HR800 UV) with a 633 nm He−Ne laser (2.5 mW) with a collection time 5 s.

4.2.4 Electrochemical measurements

Action spectra were carried out in 0.1 M sodium citrate at the open circuit potential using an Electrochemical Station (CH Instruments, Inc., Austin, TX) coupled with a monochromator (MD-1000, Optical Building Blocks Corp.). A three-electrode system was employed, with as-prepared Ag NRs and NWs as working electrode, a Pt wire as the counter electrode, and SCE as the reference electrode. An Oriel AM 1.5 filtered Xenon Arc lamp (Newport) with a full lamp intensity of 100 mW/cm^2 was the light source. CV was obtained from the same electrochemical station in 0.1 M NaOH using the same counter and reference electrodes as the action spectra measurements. The scanning rate was 0.05 V/s.

4.3 Results and Discussions

4.3.1 Experimental geometry, morphology and growth mechanism of metallic NRs and NWs

Figure 4.1 describes the experiment setup which adopts a two-electrode system for the electrodeposition of Ag NRs and NWs onto conductive substrates such as FTO glass, ITO glass, or n-type Si. An optimized distance of 3 cm was maintained between the parallel cathode and anode. The two parallel electrodes provide a uniform electric field between them. A voltage large enough to reduce Ag^+ was applied on the electrodes. A highly diluted electrolyte was chosen for the electrodeposition to ensure that the electric field is able to control ion migration. A thin layer of TiO_2 was pre-coated on FTO substrates to reduce their surface roughness. The influence of TiO_2 coating on the morphology of Ag NRs and NWs is displayed in Figure 4.2, which clearly shows the TiO_2 coating improves the uniformity and yields more well-defined Ag NRs and NWs. The above electordeposition method can be extended to other conductive substrates such as ITO and Si substrates, which is demonstrated in the Figure 4.3. These NRs and NWs on ITO substrate are confirmed to be Ag by the CV in Figure 4.4 where typical peaks corresponding to the oxidation Ag to Ag^+ and the reduction of Ag^+ to Ag. As shown in in Figure 4.5, vertically aligned Fe NRs with small aspect ratio can be successfully prepared on ITO substrate using this technique. Overall, this technique is proved to be versatile in preparing diverse metal NRs and NWs on various conductive substrates.

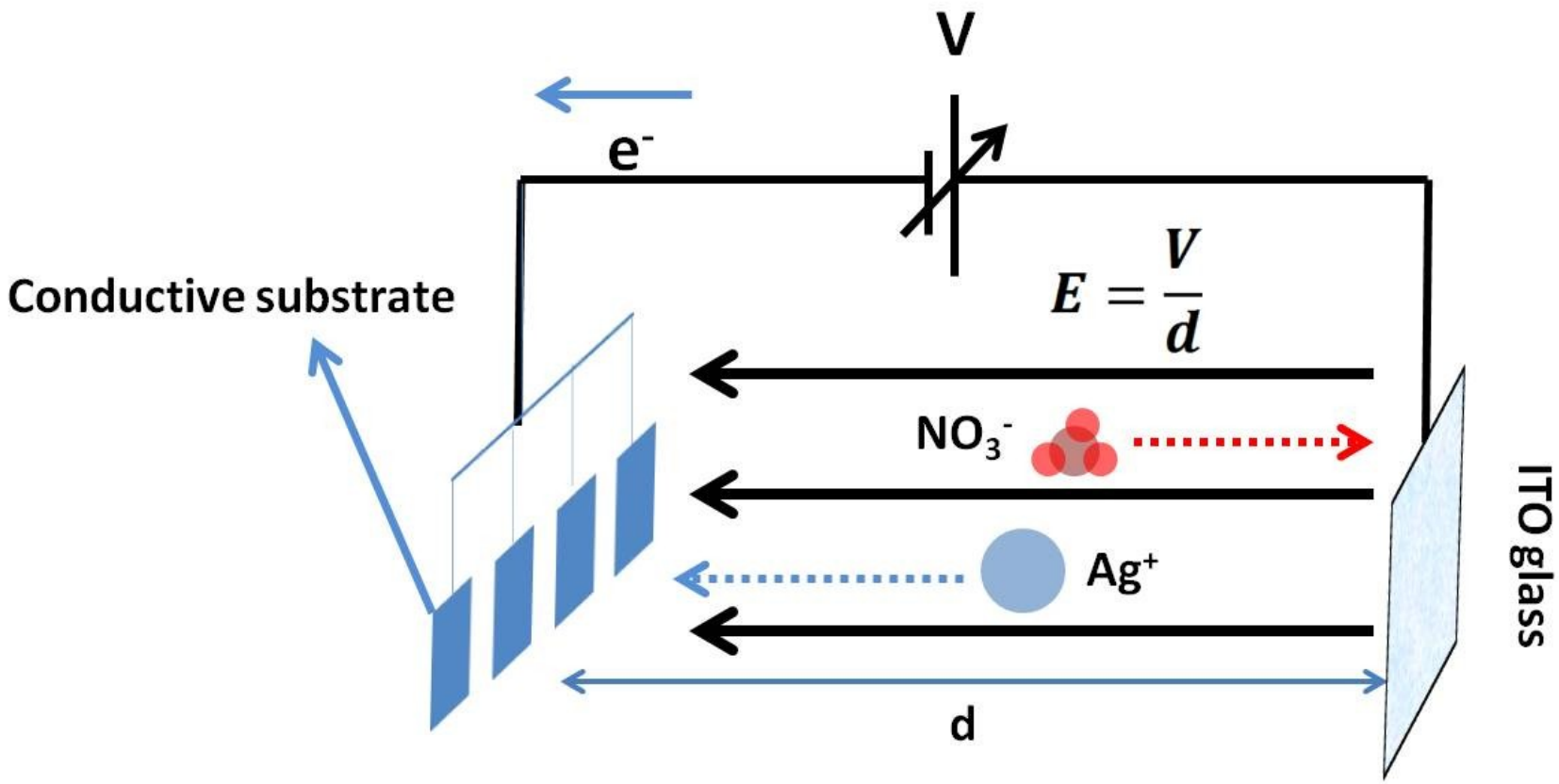

Figure 4.1 Schematic of a two-electrode system without strong electrode for formation of vertically standing nanostructures in the presence of low concentration of metal precursor.

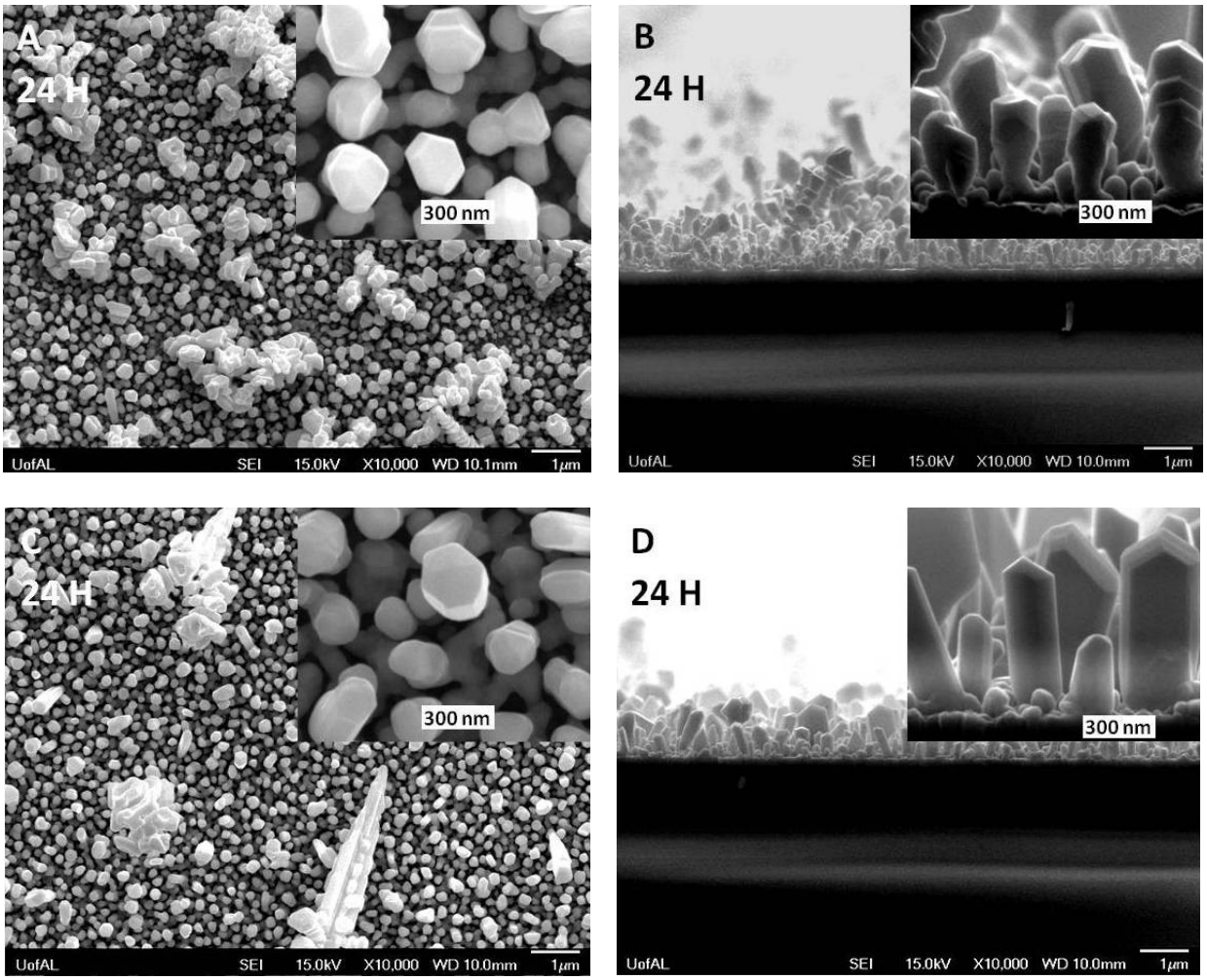

Figure 4.2 (A) top-view and (B) cross-section view of 24 H Ag NRs and NWs grown on FTO substrates without TiO_2 coating; (C) top-view and (D) cross-section view of 24 H Ag NRs and NWs grown on FTO substrates with TiO_2 coating.

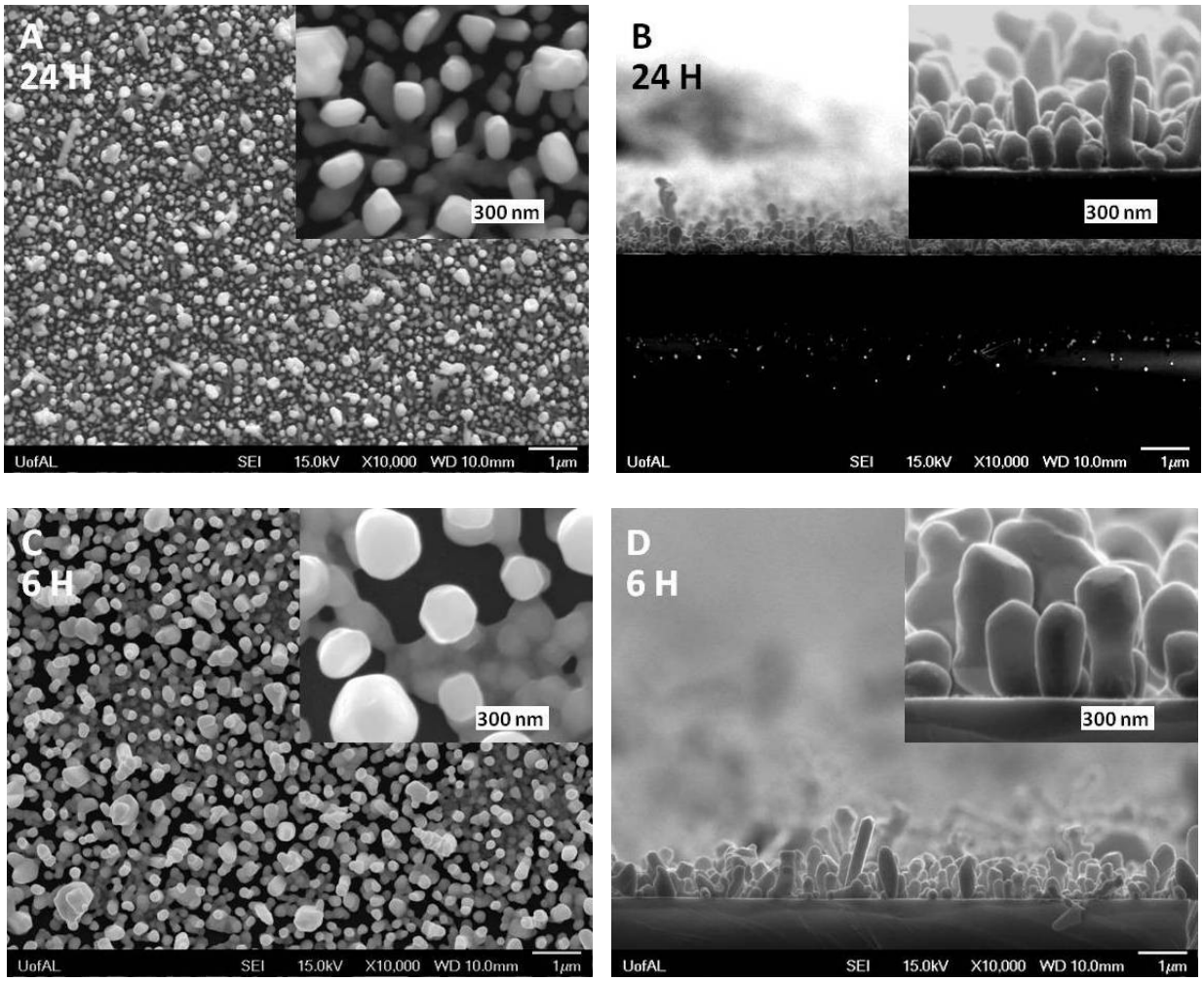

Figure 4.3 (A) top-view and (B) cross-section view of 24 H Ag NRs and NWs grown on ITO substrates; (C) top-view and (D) cross-section view of 6 H Ag NRs and NWs grown on n-type Si substrates.

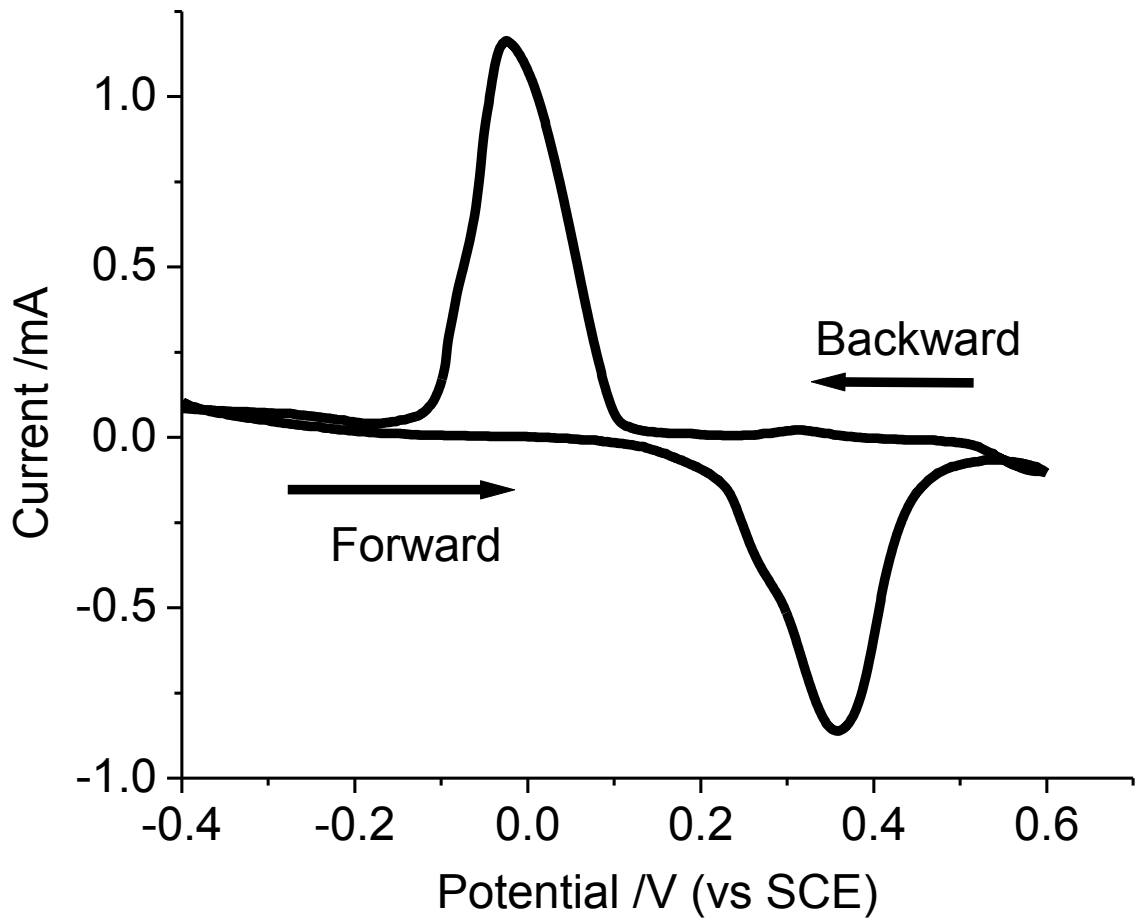

Figure 4.4 CV of 24 H Ag NRs and NWs on ITO substrate using 0.1 M NaOH as the electrolyte.

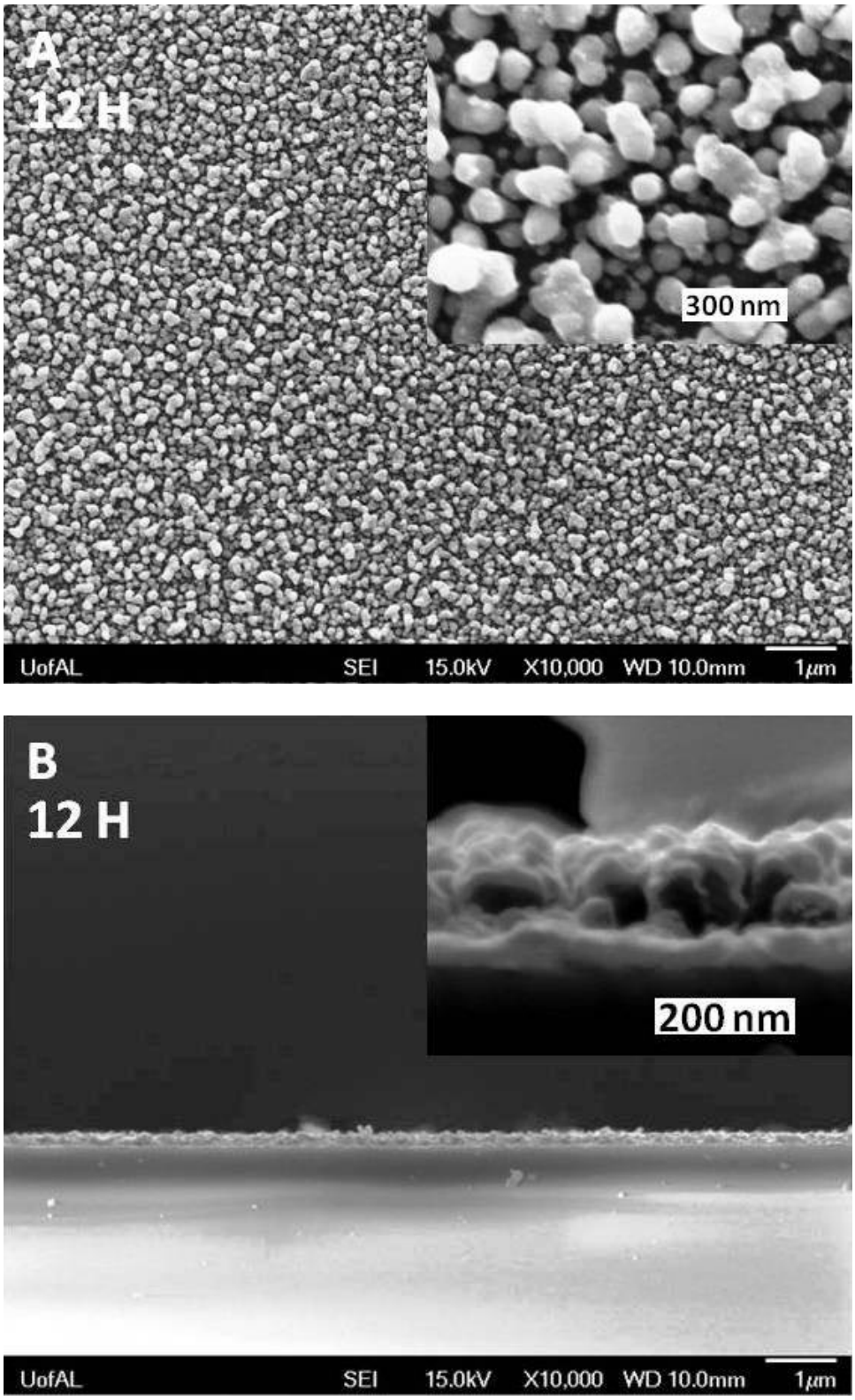

Figure 4.5 (A) top-view and (B) cross-section view of 6 H Fe NRs and NWs on ITO substrates.

To study the growth mechanism of NRs and NWs in this technique, the morphology evolution of Ag NRs and NWs were followed by taking the top-view and cross-section SEM images of Ag NRs and NWs with various electrodeposition time from 0.5 to 24 H, which are displayed in Figure 4.6 and Figure 4.7. The cross-section SEM images demonstrate that these Ag NRs and NWs are in good contact with substrates, which was further confirmed in a test that majority of the NRs and NW survived in a 10 minutes sonication in DI water. The diameter, length, and average aspect ratio (the average length divided by the average diameter) are listed in Table 4.1 and plotted against electrodeposition time in Figure 4.8. The average diameter and length are obtained by measuring the NRs and NWs in SEM images through the software Nanomeasure. The length of 0.5 and 1 H Ag NRs and NWs is not available because the particles are too small to be distinguished from the TiO_2 coated FTO substrate in the SEM images. In Figure 4.8, overall speaking, the diameter, length, and average aspect ratio of Ag NRs and NWs increase along with the electrodeposition time, excepting 1 H Ag NRs and NWs whose diameter decreases a little compared to 0.5 H sample because a large amount of small Ag seeds were generated during this period. The diameter, length, and aspect ratio increase rapidly before 6 H, and then the growing rate slows down. Especially the diameter increases extremely slowly since the enlargement of NRs and NWs is limited by the competition between adjacent NRs and NWs. When we focus on the bottom of the Ag NRs and NWs, it is noticed that they grow right from the substrate and become longer and longer in the direction perpendicular to the substrate with time goes on. From Figure 4.6A to 4.6F, it is obvious that some huge Ag particles with a diameter close to 1 μm in 0.5 H sample gradually disappear over time. This is due to the reaction of Ag with the dilute nitric acid which etches away the large Ag particles. The dilute nitric acid is generated because H_2O is oxidized by the positive potential applied on the anode through the

reaction $2H_2O - 4e^- \rightarrow O_2 + 4H^+$ and the resultant H^+ combines with NO_3^- in the solution which is original from $AgNO_3$. Ag reacts with a dilute nitric acid following the reaction $3Ag + 4\ HNO_3$ (cold and diluted) $\rightarrow 3\ AgNO_3 + 2\ H_2O + NO$, explaining why the huge Ag particles with a very large surface is progressively etched away. In the inset picture of Figure 4.7F, Ag seeds are observed right on the Ag NRs and NWs, but it is rare to see the formation of branch structure on the Ag NRs and NWs. There are two reasons for this phenomenon. One is that the solution becomes more and more acidic with the time lasts since more H_2O is oxidized and more H^+ is generated, which promotes the etching of Ag nanoparticles and inhibits the growth of Ag seeds. On the other hand, the electric field is perpendicular to the substrate, which prevents the migration of Ag^+ horizontally. These two facts act in an error correction mode together. When the seeds on NRs and NWs begin to grow horizontally to form branches, the branches will be etched away by the acid along the direction of electric field.

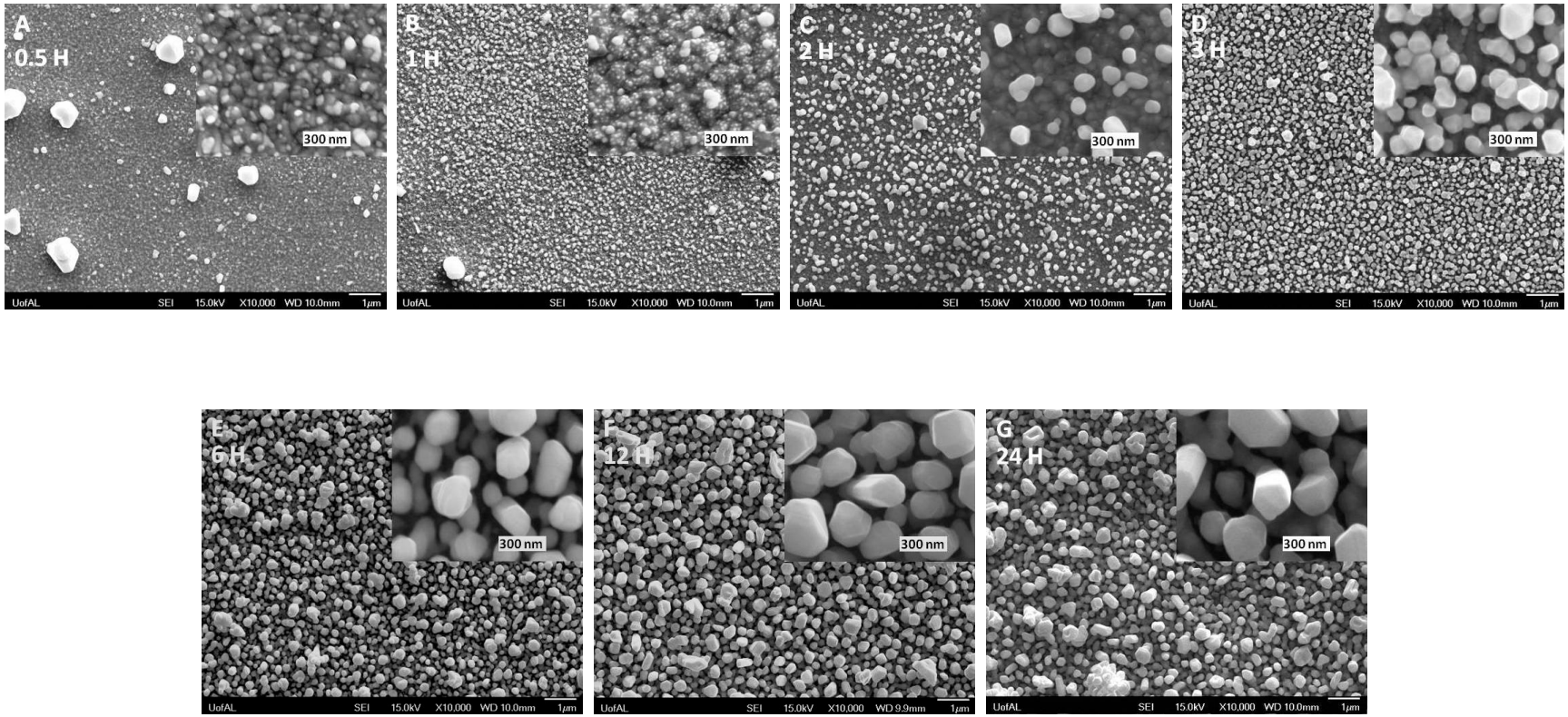

Figure 4.6 Top-view SEM images of Ag NRs and NWs with various electrodeposition time (A) 0.5 H; (B) 1 H; (C) 2H; (D) 3 H; (E) 6 H; (F) 12 H, and (G) 24 H.

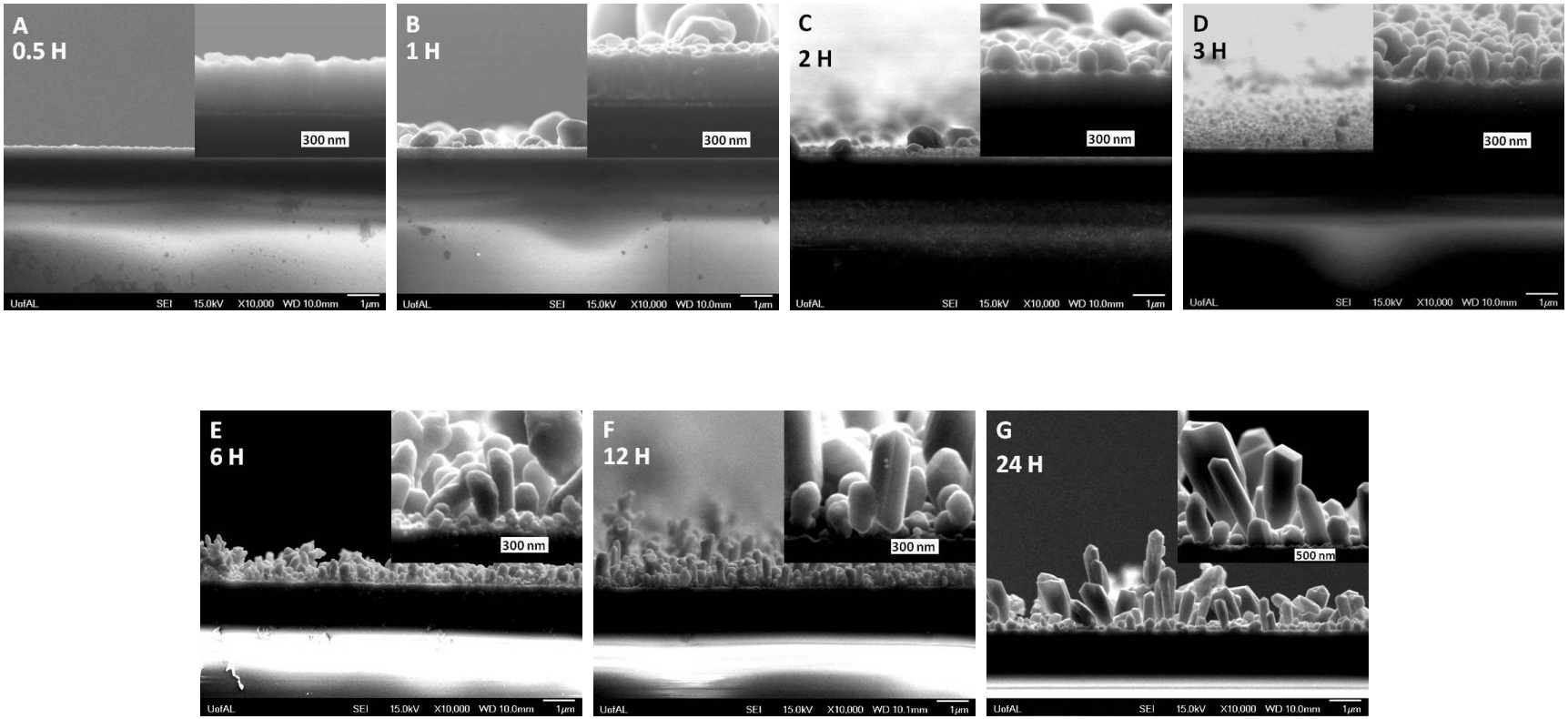

Figure 4.7 Cross-section SEM images of Ag NRs and NWs with various electrodeposition time (A): 0.5 H; (B): 1 H; (C): 2H; (D): 3 H; (E): 6 H; (F) 12 H, and (G) 24 H.

Electrodeposition time (Hour)	Diameter of Ag NRs and NWs /nm	Height of Ag NRs and NWs /nm	Average aspect ratio
0.5	34±9	N/A	N/A
1	27±16	N/A	N/A
2	89±23	134±41	1.5
3	97±15	191±45	2.0
6	170±42	436±145	2.6
12	221±44	587±213	2.7
24	247±45	799±451	3.1

Table 4.1 The average diameter, length, and aspect ratio of Ag NRs and NWs with various electrodeposition time.

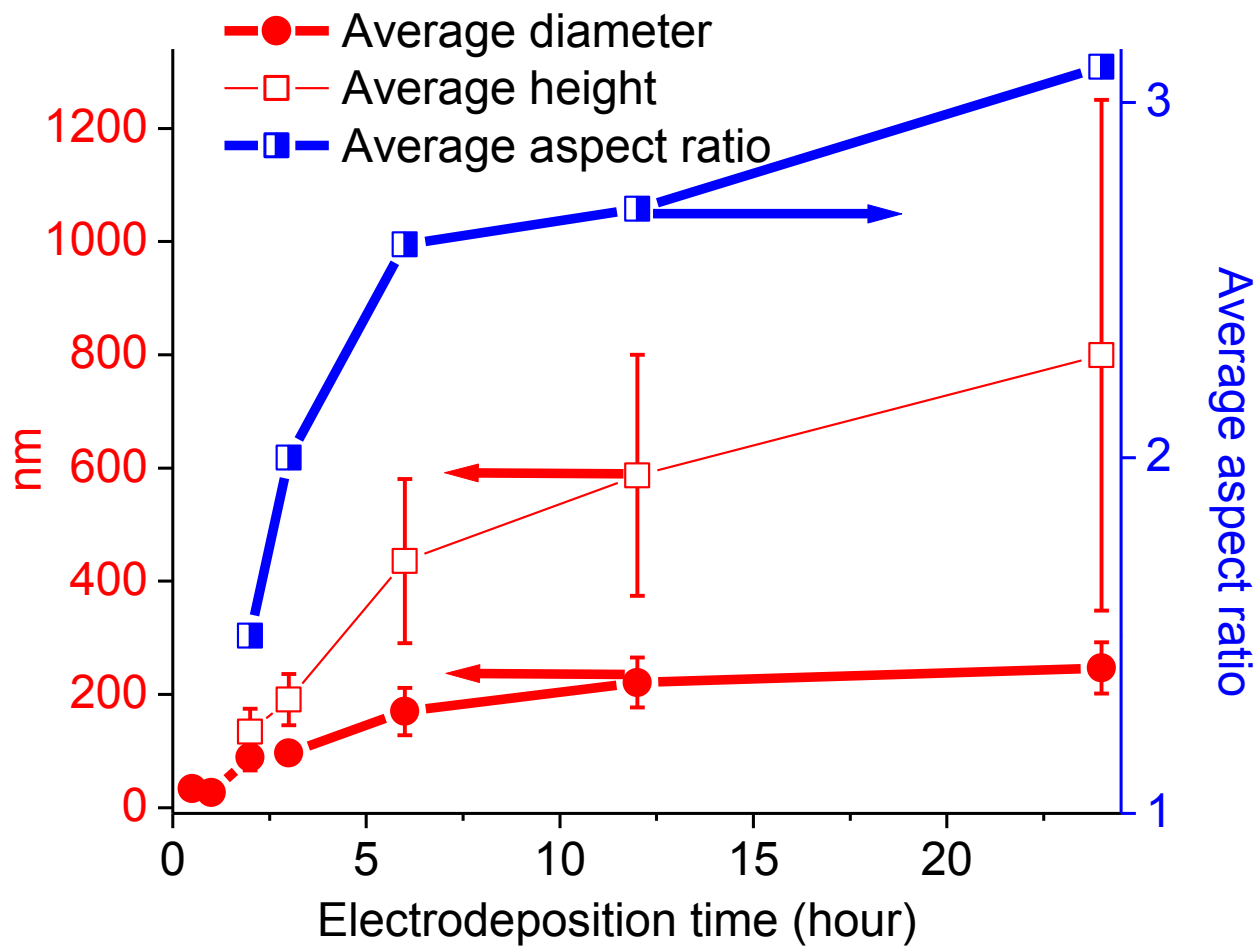

Figure 4.8 The development of the average diameter, length, and aspect ratio of Ag NRs and NWs against the electrodeposition time.

According to above results, the growth mechanism of Ag NRs and NWs is proposed as shown in Figure 4.9. At the beginning, Ag nuclei are formed on the surface of the cathode when a potential more negative than the nucleation potential is applied. Then the Ag seeds begin to grow in a direction guided by the electric filed since the positive charged Ag^+ migrates to the cathode along the direction of the electric field. During the growth of Ag seeds, new Ag seeds are still generated on the substrate because the potential on the cathode is maintained more negative than the nucleation potential, and the solution is not acidic enough to destroy the seeds, yielding an increase of coverage of Ag nanostructure on the substrate. The Ag NRs and NWs continue to grow in their diameter and aspect ratio. The increases of the coverage of Ag nanostructures, diameter, and length slow down when the coverage reaches a certain level because of the space limitation, growth competition, and the preference of reduction of Ag^+ on the formed Ag NRs and NWs, and more and more severe etching in a more acidic solution. With the electrodeposition process proceeding, vertically standing Ag NRs and NWs are constructed on the substrate.

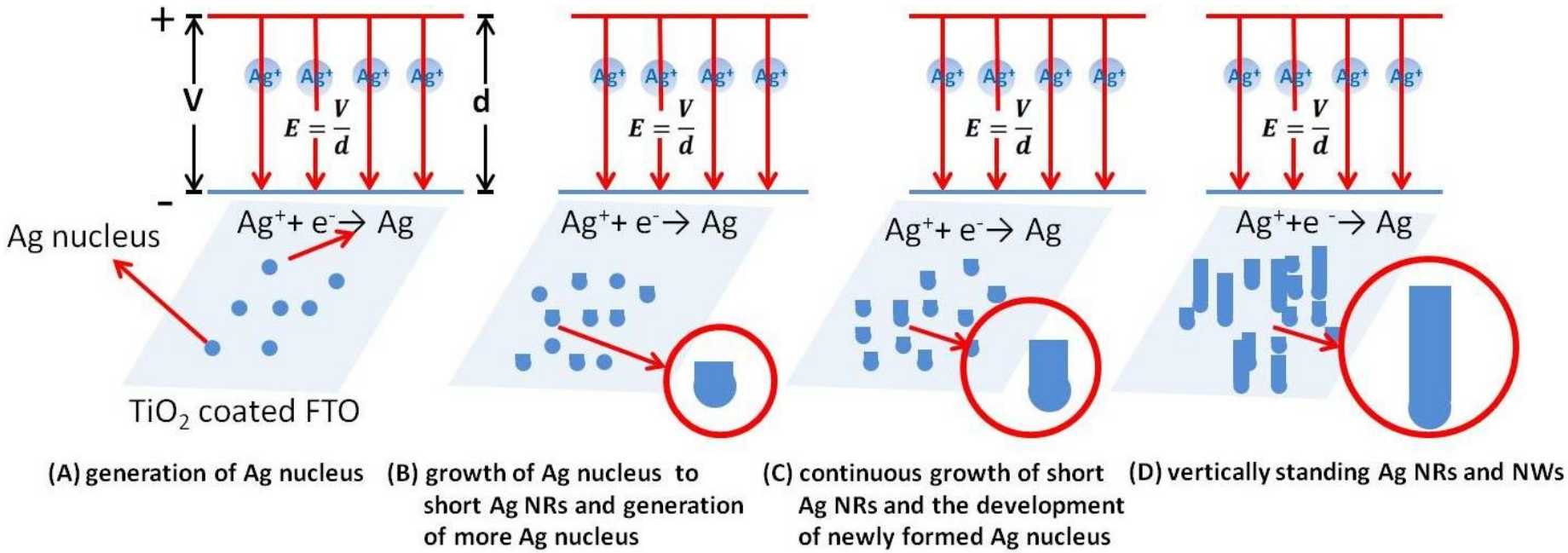

Figure 4.9 Proposed growth mechanism of Ag NRs and NWs.

4.3.2 Absorbance spectra and photoelectrochemical performance of Ag NRs and NWs

The absorbance spectra of Ag NRs and NWs on TiO_2 coated FTO glass with various electrodeposition time are displayed in Figure 4.10. A blank FTO glass was used as the reference. The absorbance of 0.5 H Ag NRs and NWs is very small because of the low density of Ag nanostructures on the substrate. With electrodeposition proceeds, the color of the samples turns from transparent to semitransparent, and then becomes opaque. When the electrodeposition time reaches 2 H, an absorbance peak around 370 nm aroused by the Ag surface plasmon becomes predominant while it is very weak for 0.5 and 1 H samples.

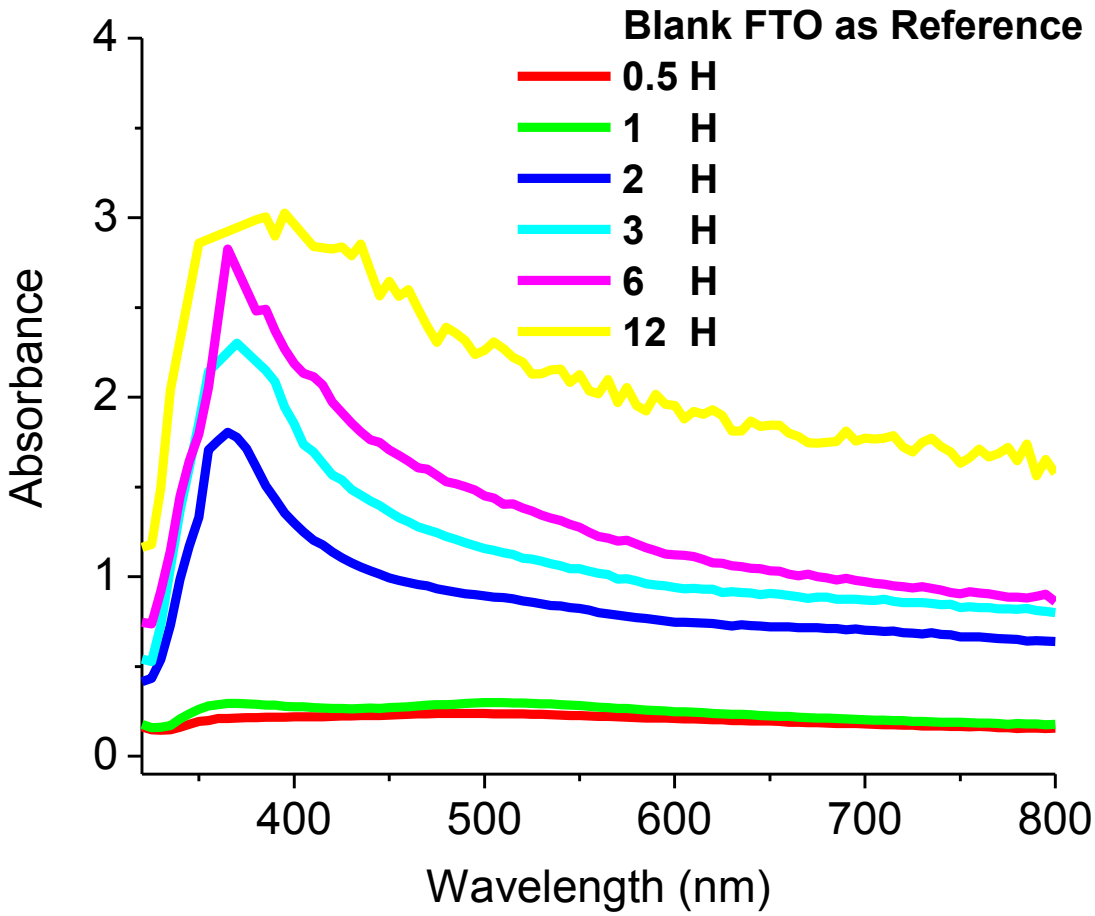

Figure 4.10 Absorbance spectra of Ag NRs and NWs with various electrodeposition time.

To study the influence of surface plasmon on the performance of photocatalyst, action spectra of 6 H Ag NRs and NWs on TiO_2 coated FTO substrate and 24 H Ag NRs and NWs on ITO substrate were measured and compared with the lamp profile and absorbance spectra, which are shown in Figure 4.11A and 4.11B, respectively. The action spectra were carried out in 0.1 M sodium citrate using a three-electrode system, with a Pt wire as counter electrode and SCE as reference electrode. The photocurrent comes from the oxidation of sodium citrate by the Ag_2O formed on the surface of Ag NRs and NWs in air. A peak around 370 nm attributed to Ag surface plasmon appears on both action spectra, which is consistent with the absorbance spectrum. When the Ag NRs and NWs were illuminated at 370 nm, the surface plasmon resonance was excited and the electromagnetic field around the Ag NRs and NWs is considerably enhanced, giving rise an enhancement of the absorbance of Ag_2O and therefore improving its photoelectrochemical performance.. The peak around 460 nm is from the light source as the lamp profile exhibits a peak exactly at the same position and no absorbance peak of Ag NRs and NWs exists there.

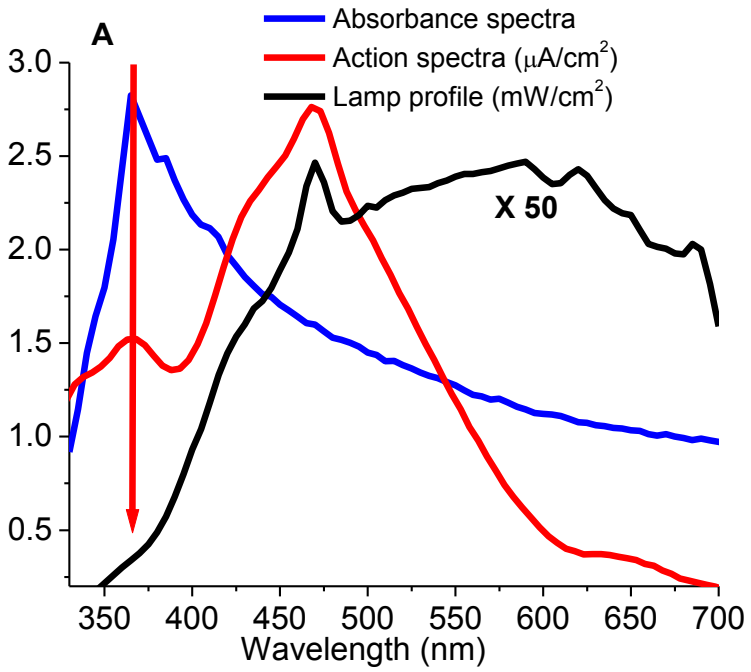

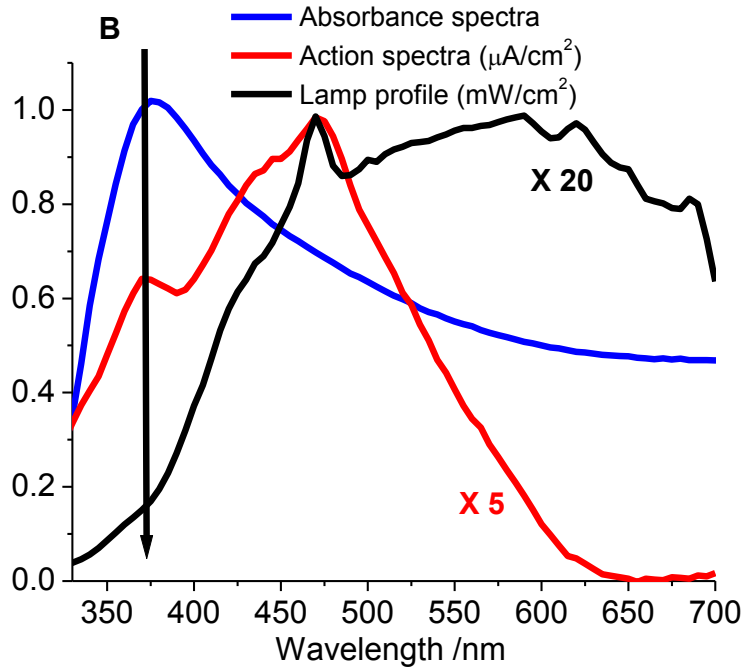

Figure 4.11 Action spectra of (A) 6 H Ag NRs and NWs on TiO_2 coated FTO substrate and (B) 24 H Ag NRs and NWs on ITO substrate in comparison with the lamp profile and absorbance spectra.

Ag NRs and NWs typically exhibit two modes of surface plasmon, transverse mode and longitudinal mode. The peak position of the transverse mode usually resides around 370 nm as mentioned above while the longitudinal mode depends on the aspect ratio of the Ag NRs and NWs which typically varies from 450 nm to 1000 nm or even longer.[17] In Figure 4.10, because the light comes from the top of Ag NRs and NWs and only the transverse mode could be excited, only one peak from the transverse mode shows up. To study the longitudinal-mode surface plasmon of Ag NRs and NWs, absorbance spectra with a p-polarized light were measured. The setup is shown in Figure 4.12. First, the light goes through a p-polarizer to be polarized in the horizontal direction. Then the light reaches the Ag NRs and NWs which are aligned perpendicular to the polarization direction and parallel to the light path. A second horizontal polarizer is set after the specimen to prevent non-polarized light from arriving at the detector. The Ag NRs and NWs samples were rotated 10°, 20°, 30°, 40°, and 50° in a horizontal plane in the clockwise direction from top view and then were returned to the original position which was designated as 0°. It is to assure the position of specimen and the light path are not changed during the rotation process. In theory, the Ag NRs and NWs are parallel to the polarized direction when they are rotated 90° and the longitudinal mode of surface plasmon is completely excited. It means from 10° to 50°, the larger angle the specimen is rotated, Ag NRs and NWs are more parallel to the polarization direction, and the larger extent of the longitudinal mode of Ag surface plasmon is excited by the polarized light. Because of the limit of the substrate holder, the sample cannot be rotated more than 50°, or the light path will be obstructed. Figure 4.13A and Figure 4.13B display the absorbance spectra of 0.5 H and 6 H Ag NRs and NWs with various rotation angle under a polarized light, respectively. The samples with a growth time of 1 H, 2 H, 3 H, and 12 H are displayed in Figure 4.14. In Figure 4.13A for the 0.5 H sample, when the

sample is rotated, the intensity of the transverse mode of Ag surface plasmon enhances swiftly while the absorbance above 400 nm does not exhibit much change. The reason is that there are only nanospheres existing for 0.5 H sample, which means no contribution from the longitudinal surface plasmon. When the specimen is rotated, more Ag nanospheres are exposed to the light, which naturally absorb more light. For the 6 H sample, the Ag nanostructures with NR and NW shape dominate. The position of the longitudinal mode of Ag NRs and NWs surface plasmon would red shift with a larger aspect ratio, displaying a much longer wavelength than the transverse mode. So one expects little change to the peak around 370 nm and the absorbance above 400 should increase with the rotation angle enlarges because the excited longitudinal-mode surface plasmon of Ag NRs and NWs absorbs majority of the photons larger than 400 nm. Meanwhile, with a larger angle the Ag NRs and NWs is rotated, a higher extent of longitudinal mode is excited, we expect a peak above 400 nm caused by the longitudinal mode will appear when the samples are rotated to a large angle. However, no such a peak shows up from 400 to 800 nm in Figure 4.13B when the sample is rotated from 10° to 50°. The reason why the peak doesn't show up is that the position of the longitudinal-mode surface plasmon of Ag NRs and NWs could be far beyond 800 nm, which is out of the range of our spectrometer. To quantitatively study the influence of longitudinal mode of surface plasmon on the absorbance of Ag NRs and NWs, the relationship between the rotation angle and the absorbance at 650 nm is depicted in Figure 4.13C and their normalized profiles are plotted in Figure 4.13D. Since the absorbance at 650 nm is way off the peak of the transverse mode 370 nm and very little contribution to the absorbance at 650 nm comes from the transverse mode, the longitudinal mode should be the major factor for absorbing light at 650 nm. From the samples are rotated from 0° to 50° and then to 0°, the absorbance of 0.5 H sample at 650 nm doesn't change much at all.

However, for the 6 H sample, the absorbance at 650 nm steadily increases and then returns to original value measured at 0°. It confirms the longitudinal mode of surface plasmon is able to enhance the absorbance. The results shown in Figure 4.14 are consistent with Figure 4.13.

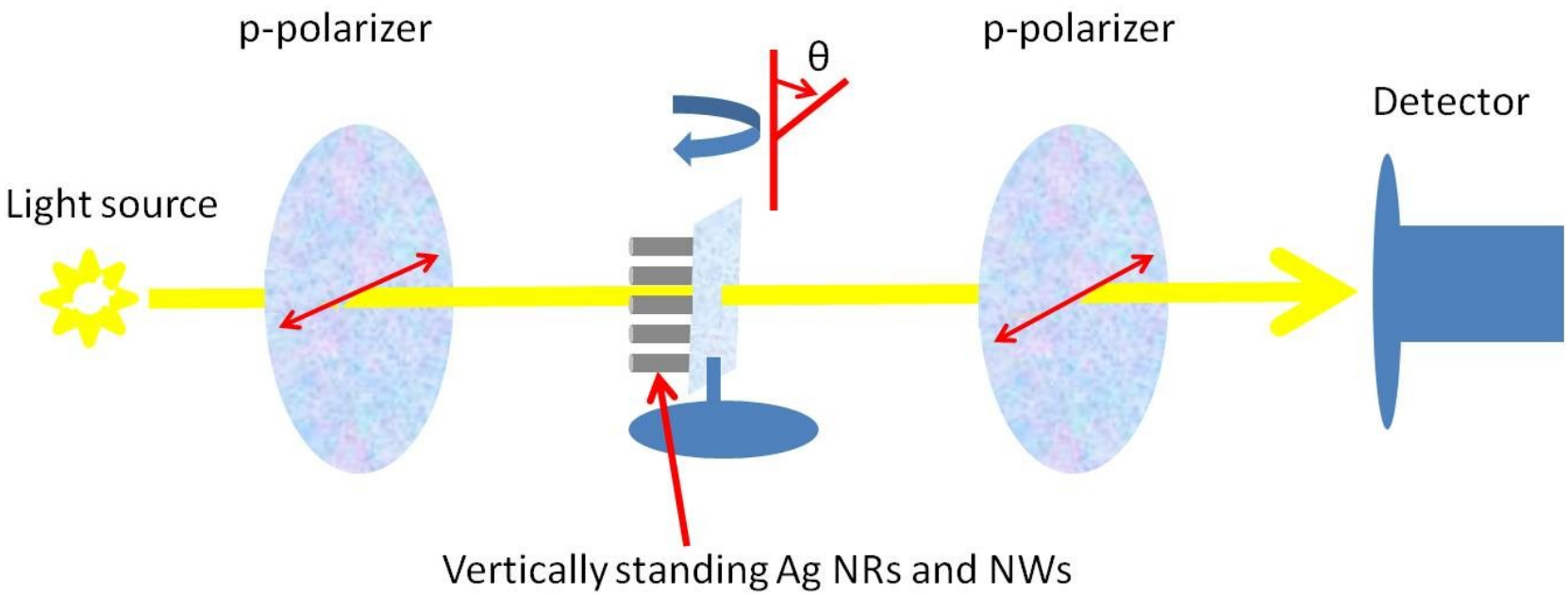

Figure 4.12 Experiment design for measuring the absorbance of Ag NRs and NWs with a p-polarized light.

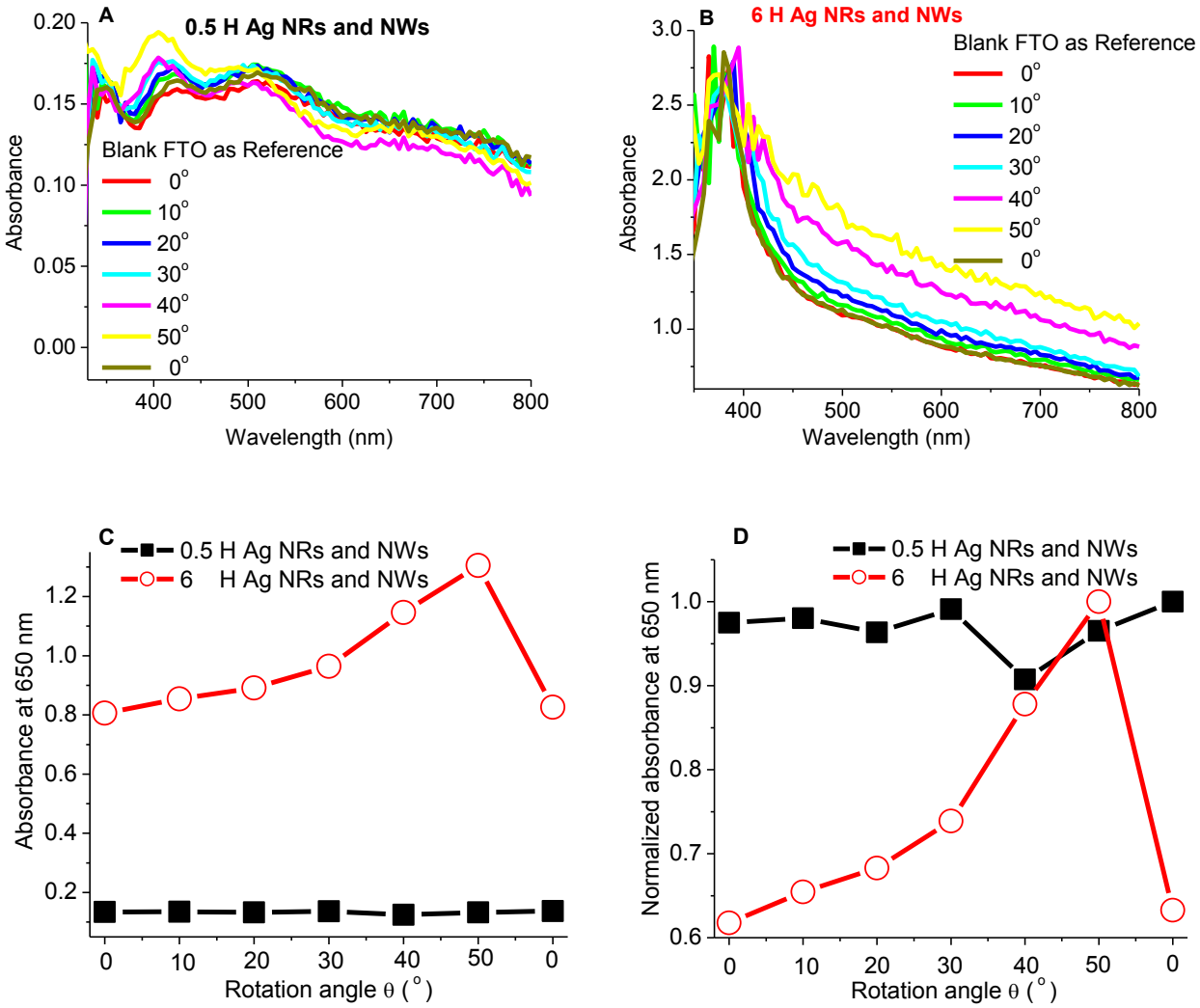

Figure 4.13 The absorbance spectra of (A) 0.5 H and (B) 6 H Ag NRs and NWs with various incident angles under a polarized light; (C) the relationship between the rotation angle and absorbance of Ag NRs and NWs at 650 nm and (D) the normalized profiles of (C).

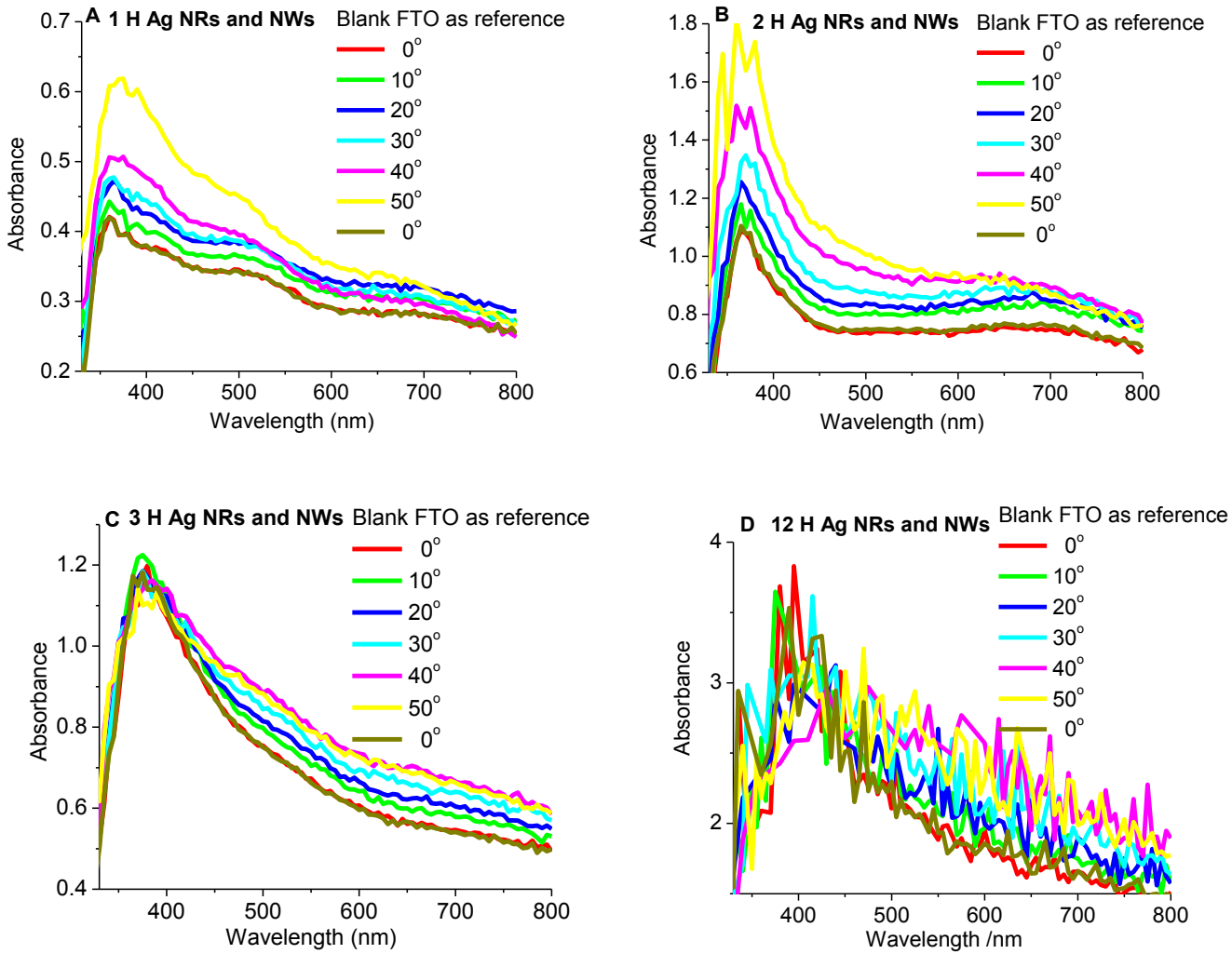

Figure 4.14 The absorbance spectra of (A) 1 H, (B) 2 H, (C) 3 H, and (D) 12 H Ag NRs and NWs with various incident angles under a polarized light.

To explore the influence of the longitudinal mode of surface plasmon on the photoelectrochemical performance, action spectra with a polarized light was carried out. The setup is similar to the absorbance experiment, only removing the second polarizer. The Ag NRs and NWs samples were rotated 30°, 45°, 60°, and 75° in a horizontal plane in a clockwise direction from top view. A 400 nm long pass filter was installed to rule out the photocurrent from TiO_2. Figure 4.15A presents the action spectra of 12 H Ag NRs and NWs on TiO_2 coated FTO substrate in 0.1 M sodium citrate. To better observe the plasmonic effect, the action spectra were normalized to the peak current and exhibited in Figure 4.15B. In Figure 4.15A, a peak around 400 nm emerges because the 400 nm long-pass filter cuts off any photos with a wavelength smaller than 400 nm. Another peak around 460 nm also shows up, which is due to the lamp profile. After the samples were rotated, no peak other than the 400 and 460 nm peak, because of the same reason as the polarized absorbance experiment that the peak of the longitudinal-mode surface plasmon of Ag NRs and NWs could be far from 800 nm which is not detectable in the device. However, the broadening of the action spectra above 400 nm is obvious in the normalized spectrum Figure 4.15B and that is attributed to the longitudinal-mode surface plasmon of Ag NRs and NWs.

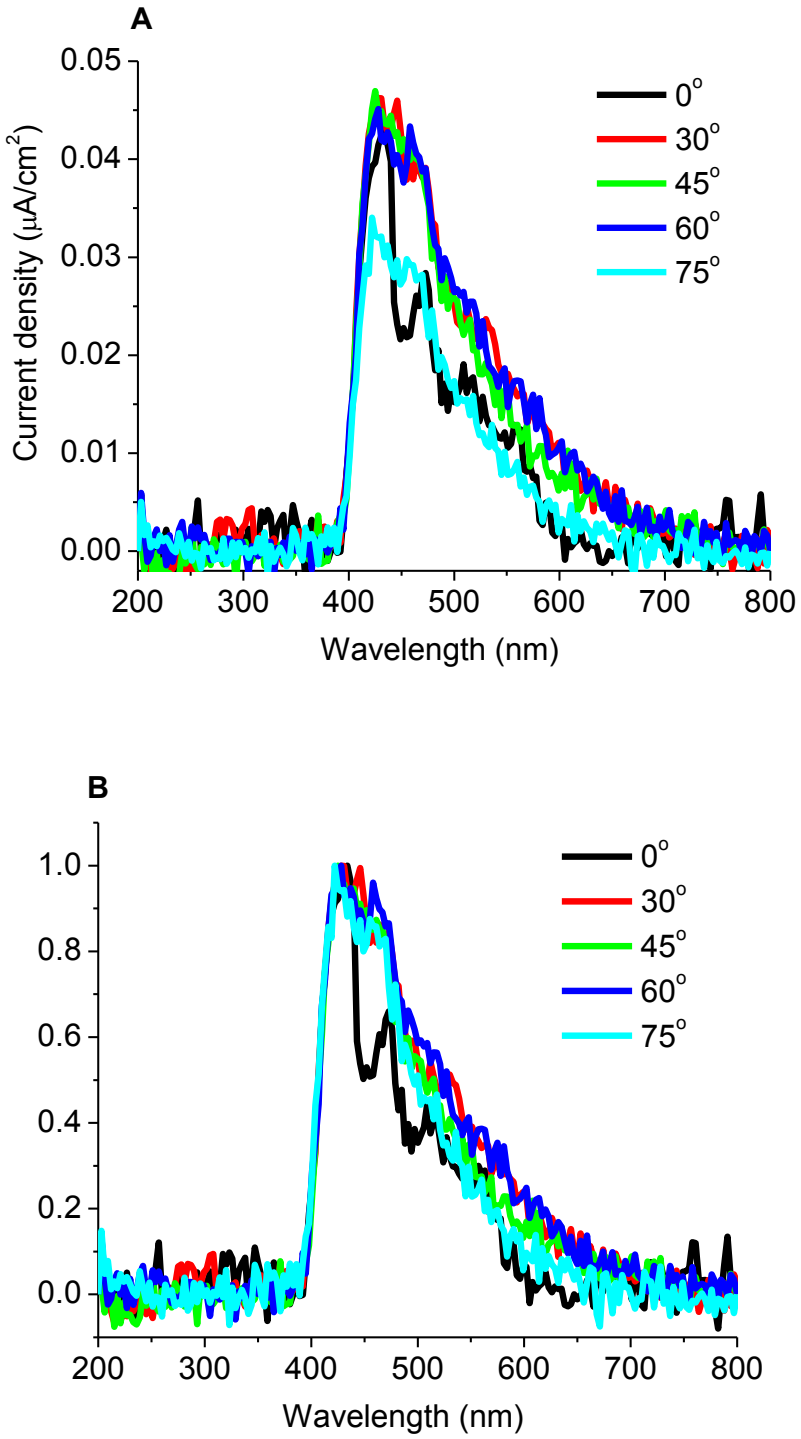

Figure 4.15 (A) The action spectra of 12 H Ag NRs and NWs on TiO_2 coated FTO substrate with various incident angles and (B) the normalized profiles of (A)

To further explore the influence of surface plasmon of Ag NRs and NWs on the photoelectrochemical system, CdS was coated on Ag NRs and NWs through CBD. CdS was chosen because it could be prepared at a low temperature which will not damage the nanostructures of Ag NRs and NWs. When CdS is illuminated, the electrons will be excited to the conduction band and the holes left on the valence band could oxidize the sodium citrate. The thickness of CdS is tuned through controlling the deposition time, 30 min was chosen for this experiment for obtaining a continuous thin film. As shown in the action spectra in Figure 4.16, bare Ag NRs and NWs display a low photocurrent density while CdS exhibits a relative high photocurrent density because of its high quantum yield. After CdS is coated on the Ag NRs and NWs, the photocurrent density of this structure is around twice of the sum of the photocurrent density from the bare Ag NRs and NWs and 30 min CdS. The enhancement of photoelectrochemical property of CdS is attributed to three factors. The first on is that the surface area of the substrate is enlarged because of the 3D structure of NRs and NWs. The second one is the surface plasmon of Ag NRs and NWs which enhances the electromagnetic field around CdS and therefore improves the absorbance of CdS. The last one is the excellent conductivity of Ag NRs and NWs which enhances the separation of excited holes and electrons and herein reduces their combination.

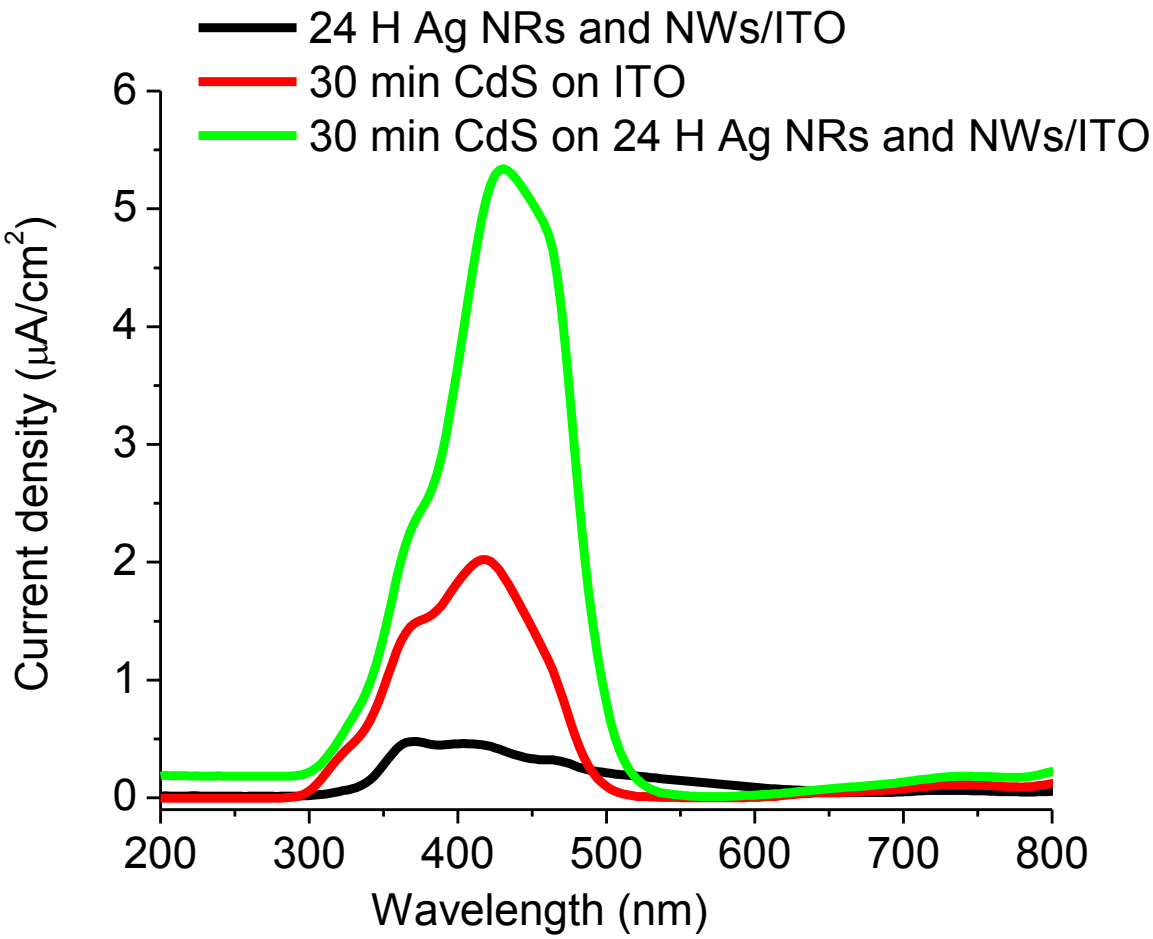

Figure 4.16 Action spectra of CdS coated Ag NRs and NWs compared with bare Ag NRs and NWs and CdS coated ITO glass.

4.3.3 Ag NRs and NWs as SERS substrates

Raman Spectroscopy, a non-destructive and speedy technique for analyzing the vibrational, rotational, and other low frequency transitions of molecules, is restricted in application because of its high detection limit. Surface plasmon of metal (e.g. Ag and Au) could strengthen the Raman signal by a factor of $10^5 – 10^8$ and achieve an extremely low detection limit. Considering the large specific surface area of the Ag NRs and NWs and the tunable distance between these NRs and NWs, they are attractive substrates for SERS application. R6G molecules were chosen as the probing molecules for studying the sensibility and stability of the Ag NRs and NWs as SERS substrates. 0.5 mL of 10^{-6} M R6G solution was dropped onto Ag NRs and NWs and let dry in air to allow R6G molecules to be adsorbed on the surface of Ag NRs and NWs. For each sample, Raman signals were measured from at least six randomly-picked points and all the peaks appear at approximately the same position with a similar intensity, which confirms the SERS reproducibility of these substrates. In Figure 4.17, Raman spectra from Ag NRs and NWs with various growth time were assembled to study the influence of the growth time on the Raman signal. For 0.5 H and 1 H Ag NRs and NWs, Raman signals from rhodamine 6G (R6G) molecules are so weak that it is hard to distinguish them from the fluorescence background. This is attributed to the low density of Ag nanostructure on the substrate as well as the large distance between them which weakens the coupling effect between Ag nanoparticles. A strong peak around 1510 cm^{-1} assigned to aromatic C-C stretching from R6G molecules appears when growth time extends to 2 H and other small peaks from R6G also become visible.[18] When the Ag NRs and NWs keep growing, the peaks from R6G intensify as the density of Ag NRs and NWs increases and the distance between each NRs and NWs narrows, resulting in a stronger coupling effect between Ag NRs and NWs which significantly enhances

the electromagnetic field around Ag NRs and NWs and herein the intensity of incident and scattered light is dramatically enhanced. Peaks at 1363, 1569, and 1649 cm^{-1} are assigned to aromatic C-C stretching. Peaks at 1184 and 1313 cm^{-1} are from the combination of the four stretching modes at 1363, 1510, 1569, and 1649 cm^{-1}.[18]

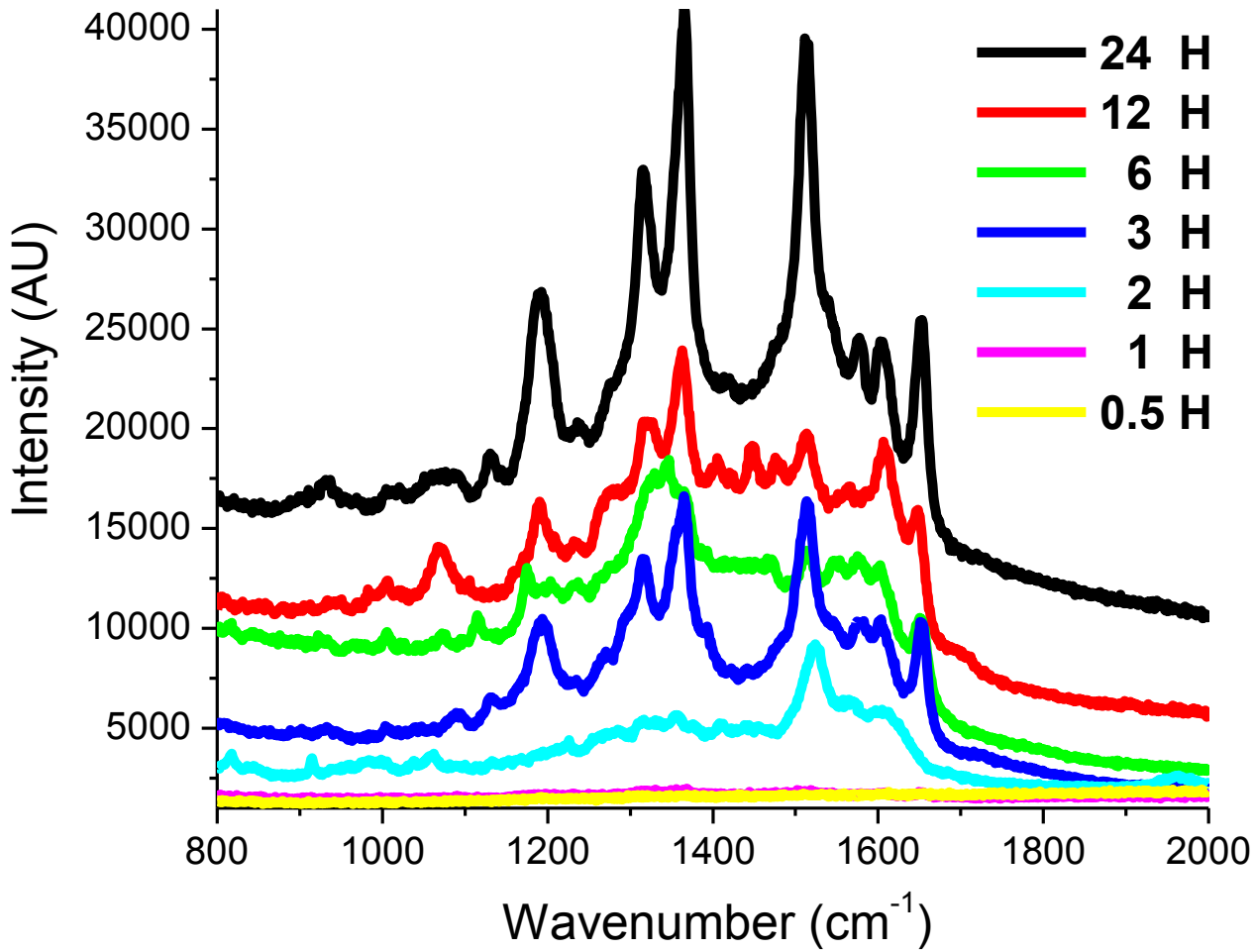

Figure 4.17 Raman spectra of R6G molecules on Ag NRs and NWs with various electrodeposition time.

4. 4 Conclusions

A template-free and low cost method was developed for the fabrication of vertically aligned metal NRs and NWs in a large scale on various conductive substrates, which opens a door for the wide application of the 3D structure. The diameter, length, and aspect ratio of NRs and NWs could be tuned through adjusting the deposition time. The Ag NRs and NWs are found to grow from bottom to top directed by the electric field between two parallel electrodes. The surface plasmons of Ag NRs and NWs are able to enhance photocatalytic reactions and serve as sensitive and reproducible substrates for SERS. Because of their large specific surface area, a strong surface plasmon, and a wide tunability over their diameter, length, and aspect ratio, they are promising to applied in the photocatalyst area and spectroscopy.

REFERENCES

(1) Grassian, V. H. When Size really Matters: Size-Dependent Properties and Surface Chemistry of Metal and Metal Oxide Nanoparticles in Gas and Liquid Phase Environments. *J. Phys. Chem. C* **2008***, 112*, 18303-18313.

(2) Ouyang, G.; Wang, C. X.; Yang, G. W. Surface Energy of Nanostructural Materials with Negative Curvature and Related Size Effects. *Chem. Rev.* **2009***, 109*, 4221-4247.

(3) Lee, S. S.; Song, W.; Cho, M.; Puppala, H. L.; Nguyen, P.; Zhu, H.; Segatori, L.; Colvin, V. L. Antioxidant Properties of Cerium Oxide Nanocrystals as a Function of Nanocrystal Diameter and Surface Coating. *ACS Nano* **2013***, 7*, 9693-9703.

(4) Tee, B. C. K.; Wang, C.; Allen, R.; Bao, Z. An Electrically and Mechanically Self-Healing Composite with Pressure- and Flexion-Sensitive Properties for Electronic Skin Applications. *Nat Nano* **2012***, 7*, 825-832.

(5) Nurmi, J. T.; Tratnyek, P. G.; Sarathy, V.; Baer, D. R.; Amonette, J. E.; Pecher, K.; Wang, C.; Linehan, J. C.; Matson, D. W.; Penn, R. L.; Driessen, M. D. Characterization and Properties of Metallic Iron Nanoparticles: Spectroscopy, Electrochemistry, and Kinetics. *Environ. Sci. Technol.* **2005***, 39*, 1221-1230.

(6) Lee, J.; Park, G. S.; Kim, S. T.; Liu, M.; Cho, J. A Highly Efficient Electrocatalyst for the Oxygen Reduction Reaction: N-Doped Ketjenblack Incorporated into Fe/Fe3C-Functionalized Melamine Foam. *Angewandte Chemie International Edition* **2013***, 52*, 1026-1030.

(7) Kawahara, Y.; Hodges, S.; Cook, B. S.; Zhang, C.; Abowd, G. D. Instant Inkjet Circuits: Lab-Based Inkjet Printing to Support Rapid Prototyping of Ubicomp Devices. *UbiComp 2013 - Proceedings of the 2013 ACM International Joint Conference on Pervasive and Ubiquitous Computing* **2013**, 363-372.

(8) Li, X.; Yang, Z.; Fu, Y.; Qiao, L.; Li, D.; Yue, H.; He, D. Germanium Anode with Excellent Lithium Storage Performance in a Germanium/Lithium-Cobalt Oxide Lithium-Ion Battery. *ACS Nano* **2015***, in publication*.

(9) Liu, J.; Li, N.; Goodman, M.; Zhang, H. G.; Epstein, E.; Huang, B.; Pan, Z.; Kim, J.; Choi, J. H.; Huang, X.; Liu, J.; Hsia, K. J.; Dillon, S. J.; Braun, P. V. Mechanically and Chemically Robust Sandwich-Structured C@Si@C Nanotube Array Li-Ion Battery Anodes. *ACS Nano* **2015***, in publication*.

(10) Chu, S.; Wada, K.; Inoue, S.; Todoroki, S.; Takahashi, Y.; Hono, K. Fabrication and Characteristics of Ordered Ni Nanostructures on Glass by Anodization and Direct Current Electrodeposition. *Chem. Mater.* **2002***, 14*, 4595-4602.

(11) Foong, T. R. B.; Sellinger, A.; Hu, X. Origin of the Bottlenecks in Preparing Anodized Aluminum Oxide (AAO) Templates on ITO Glass. *ACS Nano* **2008***, 2*, 2250-2256.

(12) Byun, J.; Lee, J. I.; Kwon, S.; Jeon, G.; Kim, J. K. Highly Ordered Nanoporous Alumina on Conducting Substrates with Adhesion Enhanced by Surface Modification: Universal Templates for Ultrahigh-Density Arrays of Nanorods. *Adv Mater* **2010***, 22*, 2028-2032.

(13) Liang, Y.; Zhen, C.; Zou, D.; Xu, D. Preparation of Free-Standing Nanowire Arrays on Conductive Substrates. *J. Am. Chem. Soc.* **2004***, 126*, 16338-16339.

(14) Hill, J. J.; Haller, K.; Gelfand, B.; Ziegler, K. J. Eliminating Capillary Coalescence of Nanowire Arrays with Applied Electric Fields. *ACS Appl. Mater. Interfaces* **2010***, 2*, 1992-1998.

(15) Park, S. H.; Shin, H. S.; Kim, Y. H.; Park, H. M.; Song, J. Y. Template-Free and Filamentary Growth of Silver Nanowires: Application to Anisotropic Conductive Transparent Flexible Electrodes. *Nanoscale* **2013**, *5*, 1864-1869.

(16) Park, S.; Shin, H.; Kim, Y.; Park, H.; Song, J. Filamentary One-Dimensional Nanocrystal Growth of Cu, AgCu, and Au in Ultra-Dilute Electrolytes. *J. Alloys Compounds* **2013***, 580*, 152-156.

(17) Hormozi-Nezhad, M. R.; Jalali-Heravi, M.; Robatjazi, H.; Ebrahimi-Najafabadi, H. Controlling Aspect Ratio of Colloidal Silver Nanorods using Response Surface Methodology. *Colloids Surf. Physicochem. Eng. Aspects* **2012***, 393*, 46-52.

(18) Hildebrandt, P.; Stockburger, M. Surface-Enhanced Resonance Raman Spectroscopy of Rhodamine 6G Adsorbed on Colloidal Silver. *J. Phys. Chem.* **1984***, 88*, 5935-5944.

CHAPTER 5

CATHODIC REDUCTION METHODS FOR IMPROVING PHOTOELETROLYSIS PERFORMANCE OF HEMATITE PHOTOANODES

5.1 Introduction

Not only does Ag has very strong surface plasmon but also possesses the highest electrical conductivity among metals. Since hematite has two major problems serving as the photoanode, a low absorbance in visible area and a short hole diffusion length, the high conductivity of Ag could be used to enhance the conductivity of hematite and therefore elongate the hole diffusion length of hematite in addition to using the surface plasmon to increase the absorbance. Meanwhile, the economical and convenient electrochemical methods are other options to better the photoelectrochemical performance of hematite, such as doping hematite to reduce the resistance of the photocatalyst and lower the charge recombination rate consequently. Thus, in this chapter, Ag nanoparticles mixed hematite and cathodic reduction techniques were developed to improve the electrochemical performance of hematite thin film and the results displays are quite promising, which may broaden the application of these techniques to other photoanodes.

5.2 Experimental

5.2.1 Cathodic reduction of α-Fe_2O_3 thin film

Hematite thin film was prepared using the same method from the chapter 3. The concentration of $Fe(NO_3)_3$ solution was varied to manage the thickness of the film. The hematite thin film was cathodically reduced using an Electrochemical Station.

5,2.2 Characterization

Action spectra of the α-Fe_2O_3 electrodes were obtained using an Electrochemical Station (CH Instruments, Inc., Austin, TX) and a monochromator (MD-1000, Optical Building Blocks Corp.) with an Oriel AM 1.5 filtered Xenon Arc lamp (Newport) as light source. The light was illuminated from the back of hematite, which means it goes through the glass first, then FTO layer, and finally reaches the hematite layer. CV and Mott-Schottky measurements were carried out using Electrochemical Station (CH Instruments, Inc., Austin, TX), with SCE as the reference electrode and a Pt wire as counter electrode. The electrolyte is 0.1 M $NaNO_3$ unless otherwise noted. The light was chopped using a PTI OC-4000 optical chopper with 5-sector disk at 0.3 Hz. Absorbance spectra were obtained using a Varian Cary 50 UV-Vis spectrophotometer. A JOEL 7000 FE SEM was used to characterize the morphology of the sample. XRD pattern was measured on a Brukker D8 XRD with a Co source (Kα1, 1.79 Å, 40 kV and 35 mA) in air at room temperature.

5.3 Results and Discussions

Ag nanospheres with a diameter of 100 nm were mixed into 100 μL 3.3 M $Fe(NO_3)_3$ solution. The total volume of the solution being spin-coated on FTO glass substrate was balanced to 200 μL with DI water to obtain a film thickness around 80 nm for all samples. The amount of Ag nanospheres was designated as the percentage weight compared to 200 μL final solution whose weight is assumed to be 200 μg. Figure 5.1 illustrates the light current of hematite thin film after mixing with a different amount of Ag nanoparticles. It clearly shows that the photocurrent of hematite is improved by Ag nanopartitlces, which is caused by the increased conductivity of hematite film after mixing with Ag nanoparticles.

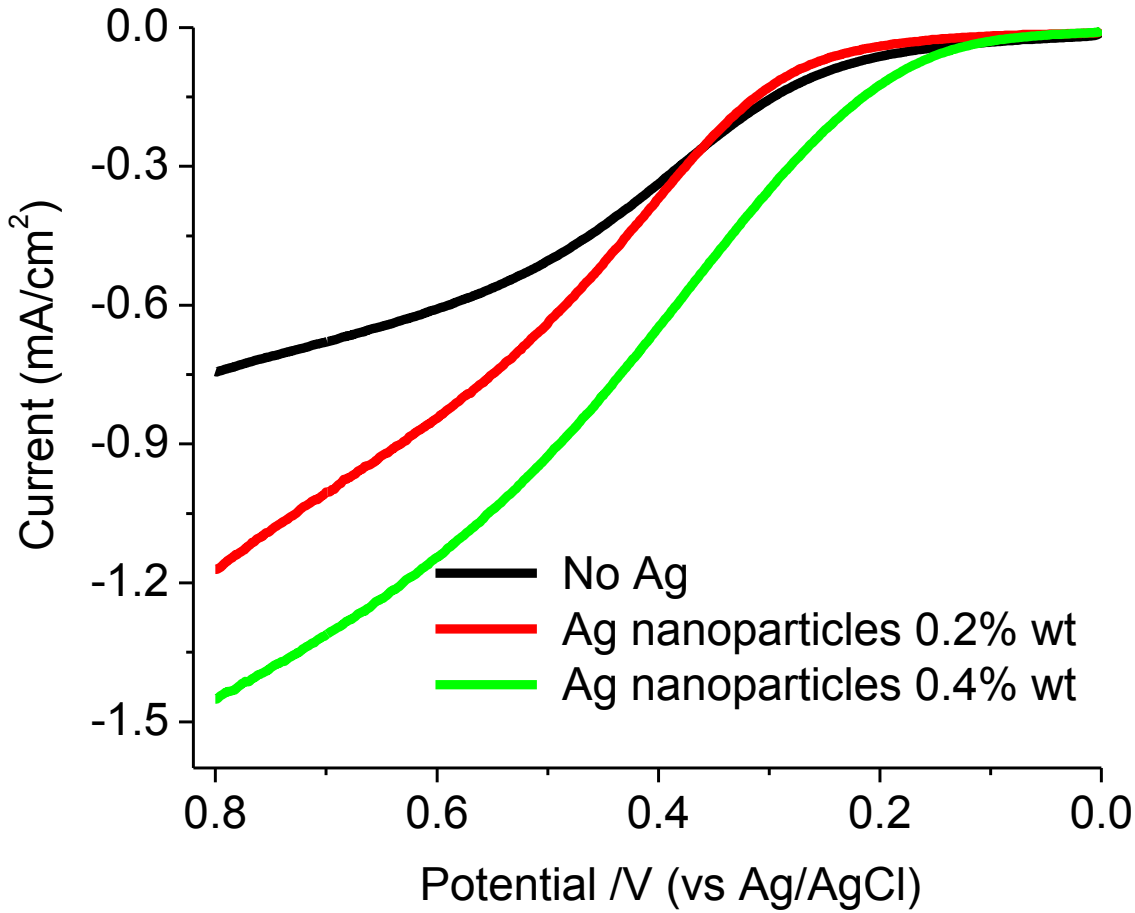

Figure 5.1 Light current of hematite thin film mixed with a different amount of Ag nanoparticles.

As mixing hematite with Ag nanoparticles could be expensive and has no control of the dispersion of Ag nanoparticles in the thin film, a cathodic reduction technique, which is low cost and has an easy control of the experimental paramerters, was studied for its potential in improving the photoelectrochemcial performance of hematite. To study the electrochemical properties of hematite thin film, CV of hematite in 0.1 M $NaNO_3$ is scanned toward a very negative potential with a scanning speed of 0.05 V/s which is displayed in Figure 5.2. Meanwhile, TiO_2 coated FTO substrate prepared in the same way except no hematite coating was adopted as a control to exclude the substrate effect. All the potentials used in this chapter are against the reference electrode SCE unless otherwise specified. For the hematite thin film, the onset potential for the cathodic current is around -0.35 V. An evident reduction peak appears around -0.8 V, corresponding to the reduction of Fe^{2+} to Fe^0, while a tiny oxidation peak shows up around -0.68 V, which means the redox reaction is not reversible and the charge could be stored in the hematite thin film through reduction reactions. The reduction peak corresponding to Fe^{3+} to Fe^{2+} is not found from the CV curve because that peak is too small compared to the peak of Fe^{2+} to Fe^0. For the TiO_2 coated FTO substrate, no redox peaks are observed, which confirms the mentioned redox peaks are from the hematite, not from the FTO substrate nor TiO_2 coated on the FTO substrate.

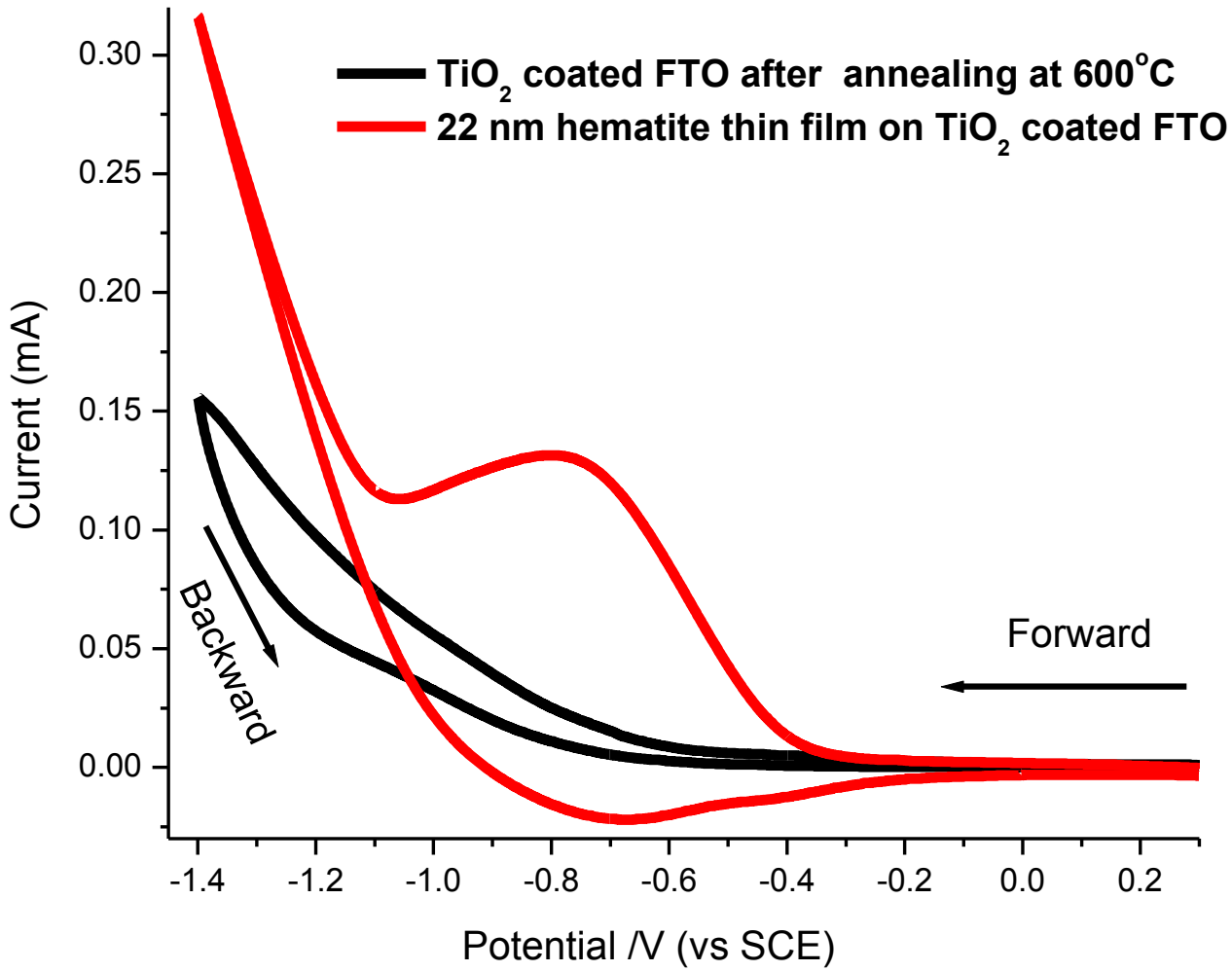

Figure 5.2 CV of 22 nm thin hematite thin film in 0.1 M $NaNO_3$.

To evaluate the influence of different cathodic potentials on the photoelectrochemical performance of hematite, action spectra of hematite thin film photoanodes with a thickness around 22 nm were measured before and after applying various cathodic in the same setup without changing anything except applying the cathodic potential. The thickness of hematite thin film was estimated using the absorption coefficient 0.005 $nm^{-}$from chapter 3. The action spectra were measured at +0.35 V, which is used to magnify the photocurrent by enhancing the oxidation of water. Figure 5.3A and Figure 5.3B illustrates the action spectra of 22 nm hematite thin film before and after applying -0.2 V for 10 s while Figure 5.3C and Figure 5.3D display the action spectra measured before and after applying -1.5 V for 10 s. After being cathodized at -0.2 V for 10 s, it is clear that the photocurrent density of the hematite thin film photoanode has not been altered after removing the background while the background barely decreases. The decrease of the background current is possible due to the +0.35 V applied during the measurement diminishes the amount of defects in the thin film. However, in Figure 5.3C when the thin film hematite is cathodized at -1.5 V for 10 s, the photocurrent density becomes remarkable compared with the one before the cathodic reduction. In Figure 5.3D, after taking off the background, the augmentation of photocurrent is tremendous, above 7 times higher than the original one,. The results of action spectra are consistent with the CV curves. From CV curve, no much change of photocurrent density is expected for -0.2 V because the -0.2 V is more positive than the onset potential of reducing Fe^{2+} to Fe^{0}, -0.35 V, which means no Fe^{0} was generated at this potential and no change happens in the hematite film. On the other side, -1.5 V, which is much more negative than -0.35 V, is able to generate a large amount of Fe^{0} in hematite thin film which is believed to enhance the conductivity of the film as well as charge separation, resulting in an

enhancement of the photocurrent density. The increase of the background also verifies that the hematite thin film becomes less resistive after applying -1.5 V for 10 s.

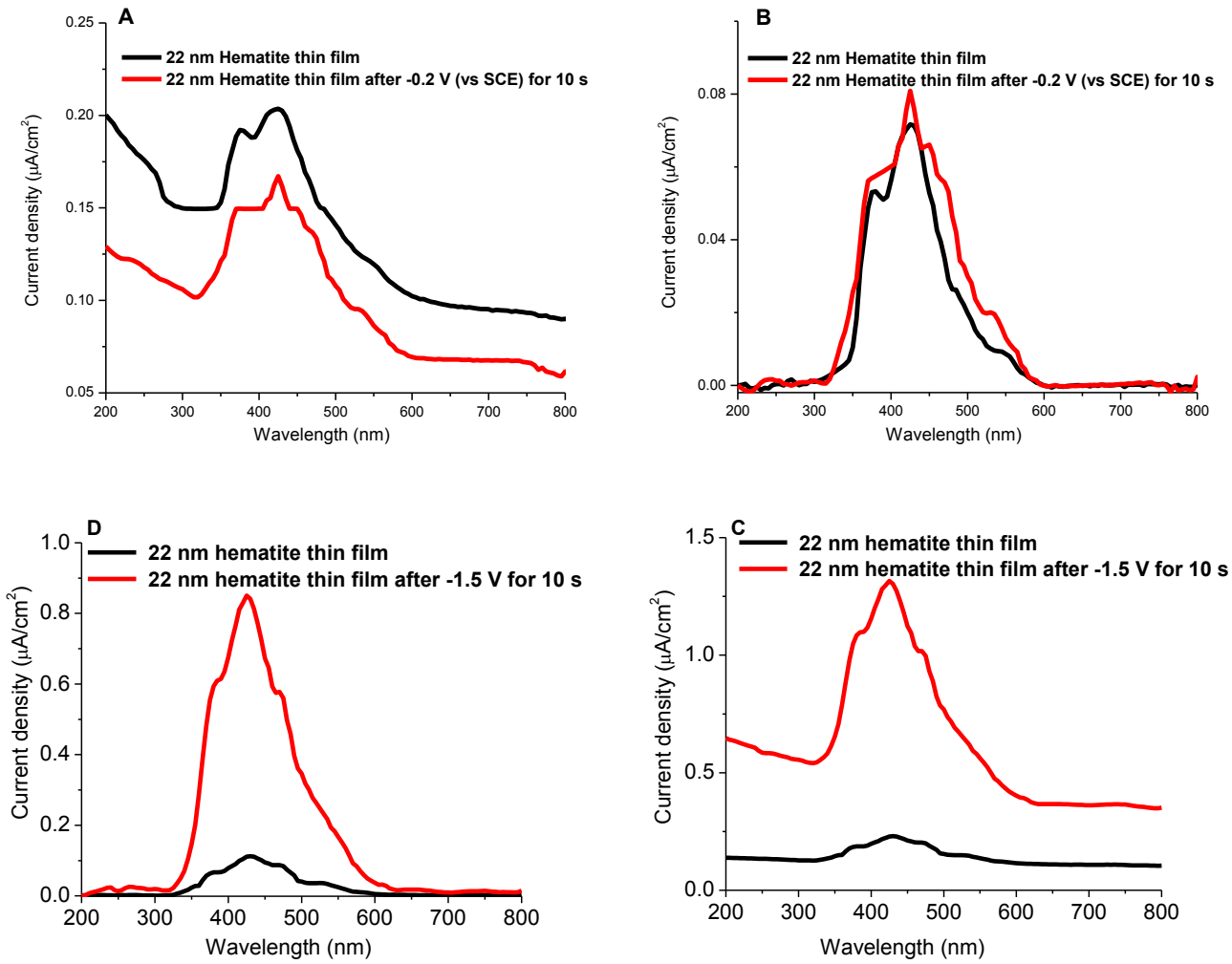

Figure 5.3 Action spectra of 22 nm hematite after applying -0.2 V for 10 s (A) before and (B) after removing the background current; after applying -1.5 V for 10 s (C) before and (D) after removing the background current.

Figure 5.4A presents the dark and light current coming from a 22 nm hematite before and after applying -1.5 V for 10 s and Figure 5.4B illustrates a manually chopped light current after the light current measurement to confirm the photocurrent after the cathodic reduction is not from background. Before the cathodization, the dark and light current of the hematite thin film are small, which is reasonable considering the action spectra is measured in a neutral solution whose pH is close to 7 and it is not favorable for the oxidation of water. After applying -1.5 V for 10 s, the dark current of the hematite thin film slightly increases in the range from 0 V to 0.6 V, but returns to a value close to that before the cathodic reduction is applide from 0.6 V to 0.8 V. However, the light current density was booted from an unnoticeable -0.01178 mA/cm^2 to -0.12411 mA/cm^2 at 0.8 V. The chopped light current was taken right after the light current was measured and is exhibited in Figure 5.4B, which confirms the incredible enhancement of current density is due to photocurrent from the hematite thin film photoanode, not because of the background current.

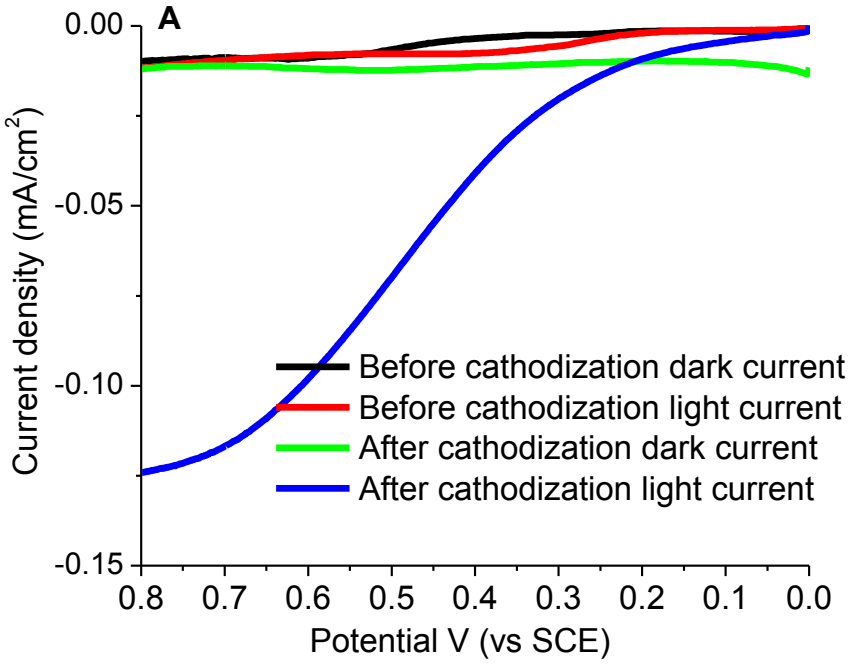

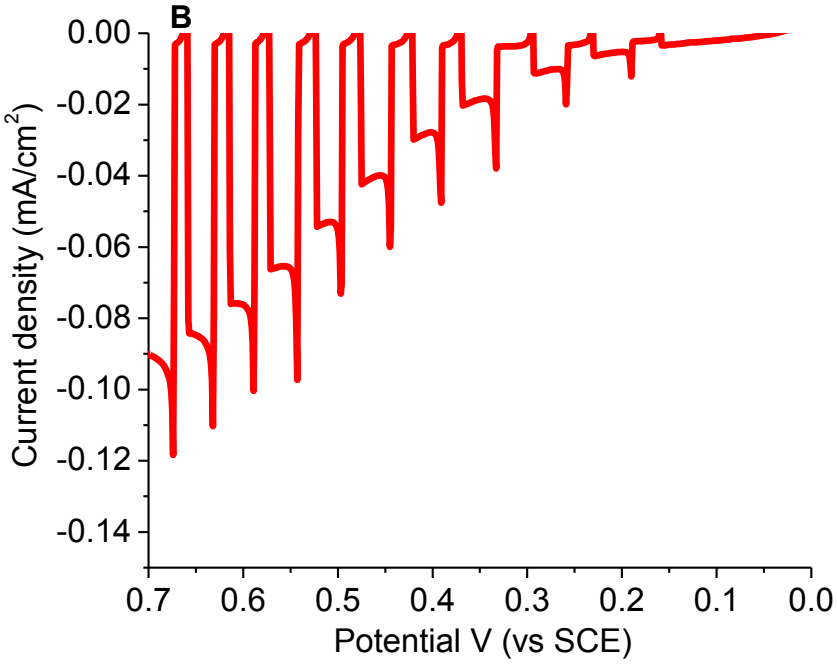

Figure 5.4 (A) Dark and light current of 22 nm hematite before and after applying -1.5 V; (B) chopped photocurrent after the light current measurement.

To study the mechanism for the enhancement of the photocurrent of thin film hematite after the cathodic reduction, photocurrent density time-dependent curves of hematite with various thicknesses after different cathodization potentials were recorded and demonstrated in Figure 5.6. Figure 5.5 shows the absorbance spectra of hematite thin films prepared with various concentration of $Fe(NO_3)_3$ which are used to estimate the thickness of hematite thin film. A three-electrode system was adopted for the photocurrent measurement, with a piece of hematite thin film as the working electrode, a Pt wire as the counter electrode, and a SCE as the reference electrode. During the measurement, the light was chopped by a 5-sector chopper at a frequency of 0.3 Hz. When the bands in Figure 5.6A and Figure 5.6B are zoomed in, serrated lines are observed as shown in the inset images because of the chopper blocks and unblocks the incident light, resulting the dark and light current density. Therefore, the width of the band which equals to the difference between the current density with and without blocking the incident light displays the magnitude of the photocurrent density. The potential is applied in following sequences as shown in Figure 5.6A: +0.8 V for 20 s; apply 0.0 V for 20 s, then +0.8 V for 20 s; apply -0.5 V for 20 s, then +0.8 V for 20 s; apply -1.0 V for 20 s, then +0.8 V for 50 s; apply -1.5 V for 20 s, then +0.8 V for 500 s. Applying +0.8 V is to obtain a noticeable photocurrent density from the hematite thin film photoanode. Keep measuring the photocurrent density for 500 s after applying -1.5 V is to explore the stability of photocurrent density after the treatment and verify the photocurrent is not from the transient current. In Figure 5.6, it is obvious that the cathodization potential has a larger effect on the photocurrent density of thin films than on the thicker films. For 10 and 28 nm hematite thin films, the photocurrent density increases obviously when a more negative cathodization potential is applied while not much change happens to the photocurrent density for the 62 and 147 nm thin films. The magnitude of the photocurrent

density of hematite obtained at 20 s after each cathodic reduction and at 500 s after -1.5 V is listed in Table 5.1 and their enhancement factors of photocurrent density are plotted in Figure 5.7 to display the influence from the thickness and cathodic potential on the photoelectrochemical performance of hematite. The enhancement factor is defined as the ratio of the photocurrent density over the initial photocurrent density which is measured before applying any potential. From the cathodic potential aspect in Figure 5.7, there is no enhancement when 0.0 V is applied for 20 s for all the samples. After -0.5 V is applied, the photocurrent density of two thin films 10nm and 28 nm begins to increase while the thicker films are not affected. When a more negative potential -1.0 V and -1.5 V is applied, the photocurrent density is remarkably enhanced for the thin film, about 5.6 and 6.2 times of the original current density for the 28 nm thin film and for 10 nm after applying -1.5 V for 10 s, respectively. On the contrary, the photocurrent density is only 1.82 and 1.43 times of the original one even after applying -1.5 V for the 62 nm and 147 nm samples. It is worth nothing that the cathodic potential should not be too negative, or the hematite thin film will be totally reduced to Fe^0 and no photo response anymore. The photocurrent density of 28 nm hematite thin film after applying -1.5 V could be as large as 1 mA/cm^2 in the first few senconds, then decreases to 0.708 mA/cm^2 after 20 s, further down to 0.330 mA/cm^2 after 500 s because Fe^0 is reoxidized to Fe^{3+} when +0.8 V is applied on the hematite thin film to help oxidize water during the photo response test. However, even after 500 s, the photocurrent density is still ~3 times of the original photocurrent density, demonstrating the enhancement of the photocurrent density is not due to transient current and showing a relative stability of the photoelectrochemical performance of hematite after the cathodic reduction.

A question arises that where the reduction $Fe^{3+} \rightarrow Fe^{2+} \rightarrow Fe^{0}$ majorly happens in the hematite thin film, close to the interface between TiO_2 and hematite or the area close to the electrolyte? For hematite, the 10~20 nm region close to the hematite/electrolyte interface is the most important area for the photo oxidation of water because the hole diffusion distance in hematite is around only 2-4 nm[21,22] or 20 nm[23]. The district in the hematite thin film far away from that 10~20 nm region only acts more and more like a connection wire. That is the reason why the 10 and 28 nm hematite thin films are very sensitive to the cathodic potential, the 62 nm samples are less sensitive, and the cathodic potential has little impact on the 147 nm hematite thin film. Therefore, the reduction of $Fe^{3+} \rightarrow Fe^{2+} \rightarrow Fe^{0}$ should majorly happen close to the TiO_2-hematite interface where it doesn't influence the photoelectrochemical performance of the thick film much, but affect the thin film with thicknesses around 20 nm principally.

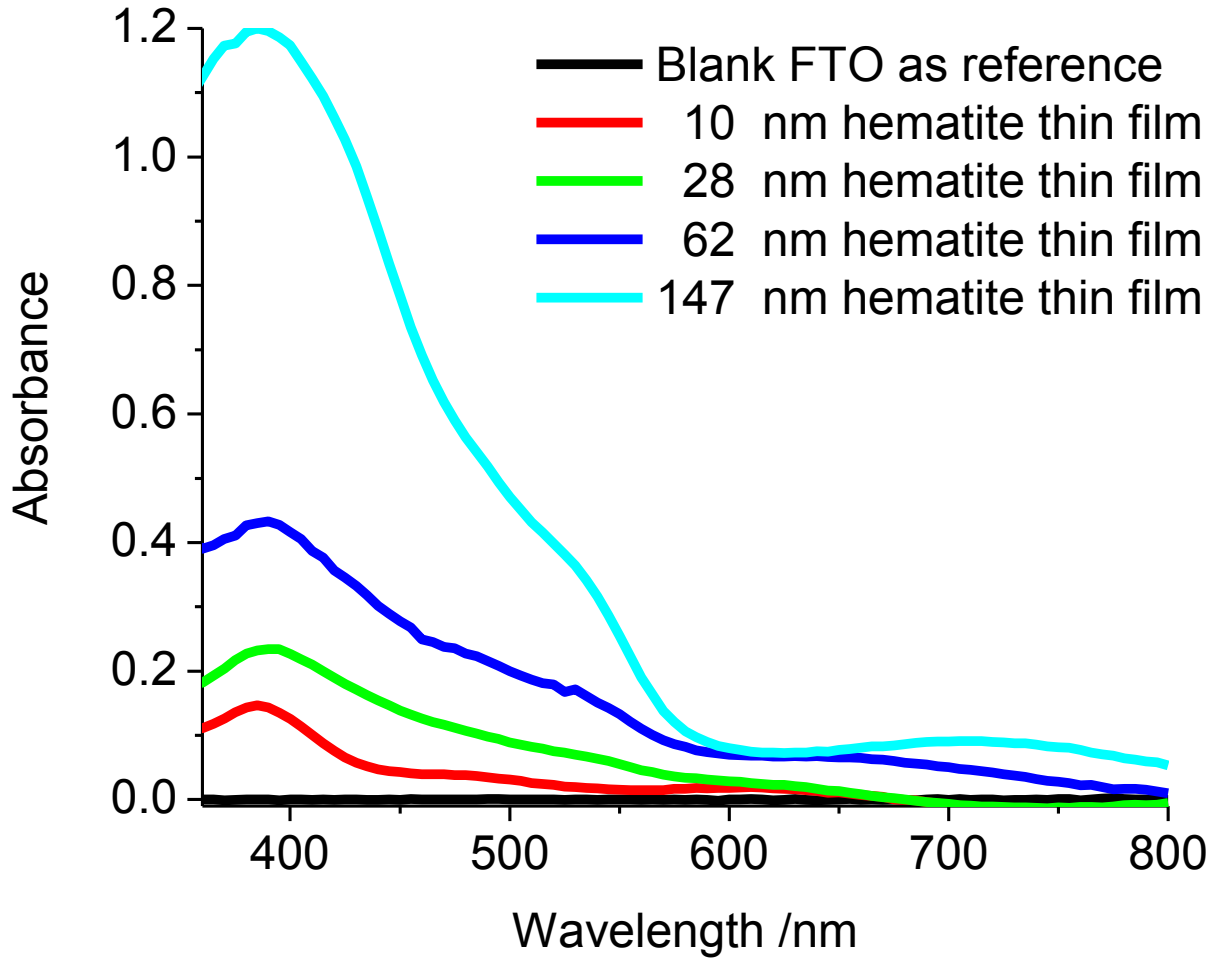

Figure 5.5 Absorbance of hematite thin film with various thicknesses.

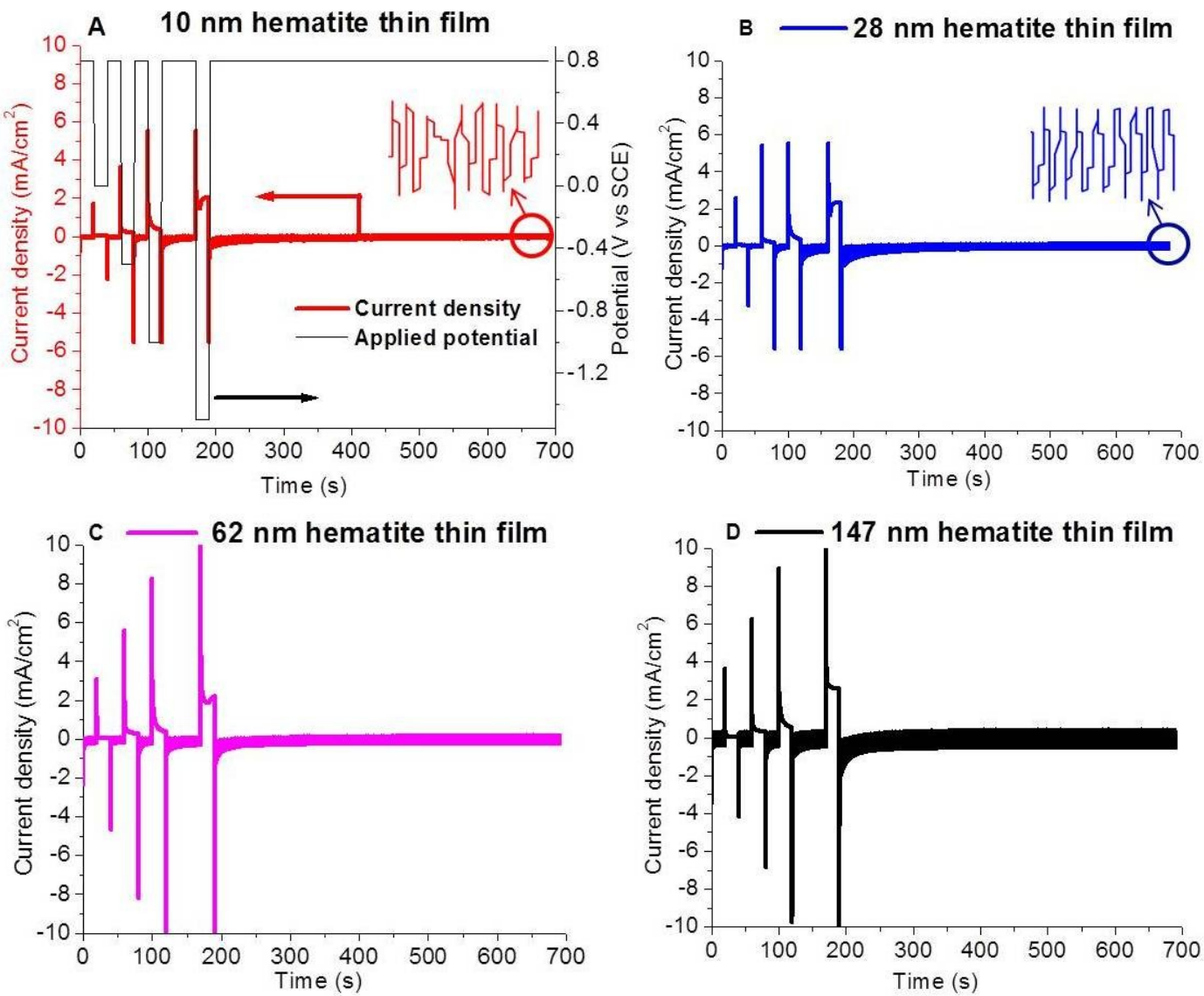

Figure 5.6 Photocurrent density of hematite (measured at +0.8 V) with various film thickness (A) 10 nm, (B) 28 nm, (C) 62 nm, and (D) 147 nm after different cathodic potentials (0 V for 20 s, -0.5 V for 20 s, -1.0 V for 20 s, and -1.5 V for 20 s).

Thickness of the hematite thin film	Initial photocurrent density (mA/cm^2)	20 s after 0 V (mA/cm^2)	20 s after -0.5 V (mA/cm^2)	20 s after -1.0 V (mA/cm^2)	20 s after -1.5 V (mA/cm^2)	500 s after -1.5 V (mA/cm^2)
10 nm	0.075	0.084	0.127	0.249	0.417	0.155
28 nm	0.114	0.114	0.168	0.449	0.708	0.330
62 nm	0.283	0.286	0.307	0.465	0.515	0.437
147 nm	0.736	0.739	0.788	0.913	1.056	0.969

Table 5.1 Photocurrent measured at 0.8 V vs SCE responses to cathodic potentials and hematite film thickness. This data is obtained from Figure 5.6 by using the highest current around the specified time minus the lowest current around that time.

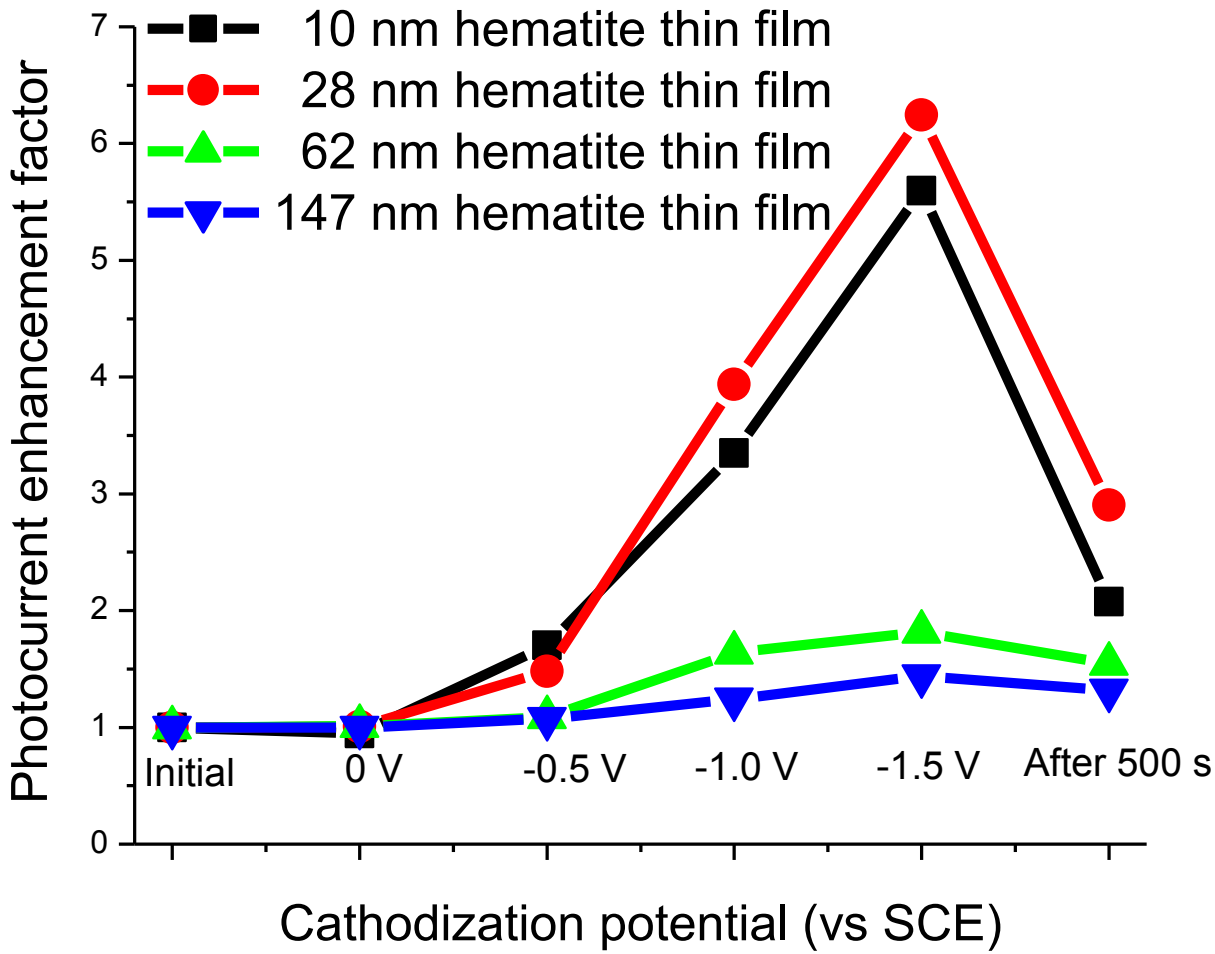

Figure 5.7 Photocurrent density enhancement of hematite thin film with various thicknesses after applying different potentials (0 V for 20 s, -0.5 V for 20 s, -1.0 V for 20 s, and -1.5 V for 20 s). This graph is plotted by using the data from Table 5.1.

To reassure the enhancement of the photocurrent density of hematite is not specific to just one electrolyte, 0.1 M $NaON_3$ was replaced by 0.1 M NaOH and action spectra of 22 nm hematite thin film were measured before and after applying -0.8 V for 10 s and presented in Figure 5.8. The photocurrent was doubled after the cathodic reduction, which confirms the electrolyte is not the reason for the enhancement of the photocurrent and it should be related to the change inside the hematite thin film after the cathodic reduction.

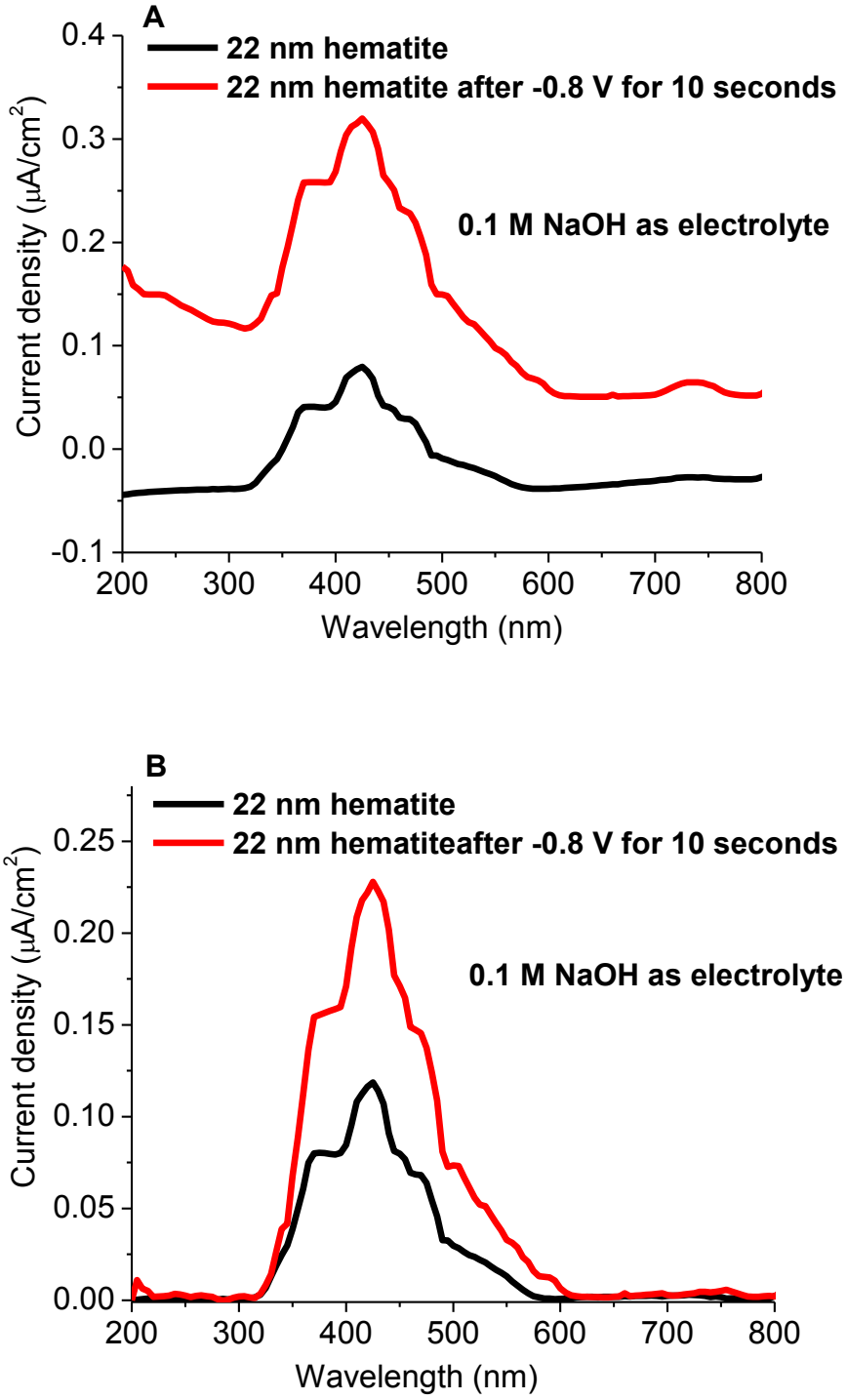

Figure 5.8 (A) action spectra of 22 nm hematite in 0.1 M NaOH after applying -0.8 V for 10 s; (B) after removing the background current of (A).

To study why the photoelectrochemcial performance of hematite was improved after the cathodization, SEM images and XRD pattern of hematite thin film were taken before and right after cathodization and shown in Figure 5.9 and 5.10 respectively. Neither morphology nor crystal structure change was noticed for the hematite after the cathodic reduction. The absorbance spectra and absorbance difference (the absorbance value after cathodic reduction minus the value at the same wavelength before the treatment) before and after cathodic reduction are displayed in Figure 5.11A and 5.11B respectively. The absorbance peak at 390 nm attributed to $O^{2-} \rightarrow Fe^{3+}$ charge transfer from O_{2p} nonbonding orbitals to lowest empty Fe d orbitals drops the most, indicating the amount of Fe^{3+} in the film reduces and vindicating that reduction of Fe^{3+} to Fe^{0}.

To further investigate this phenomenon, Mott-Schottky Plot was taken before and after the cathodic reduction and displayed in Figure 5.12. The slope of the plot which indicates the carrier intensity increases from 4.278×10^{19} cm^{-3} to 1.296×10^{20} cm^{-3}after cathodic redution, which explains the enhancement of the photocurrent density after the cathodic reduction.

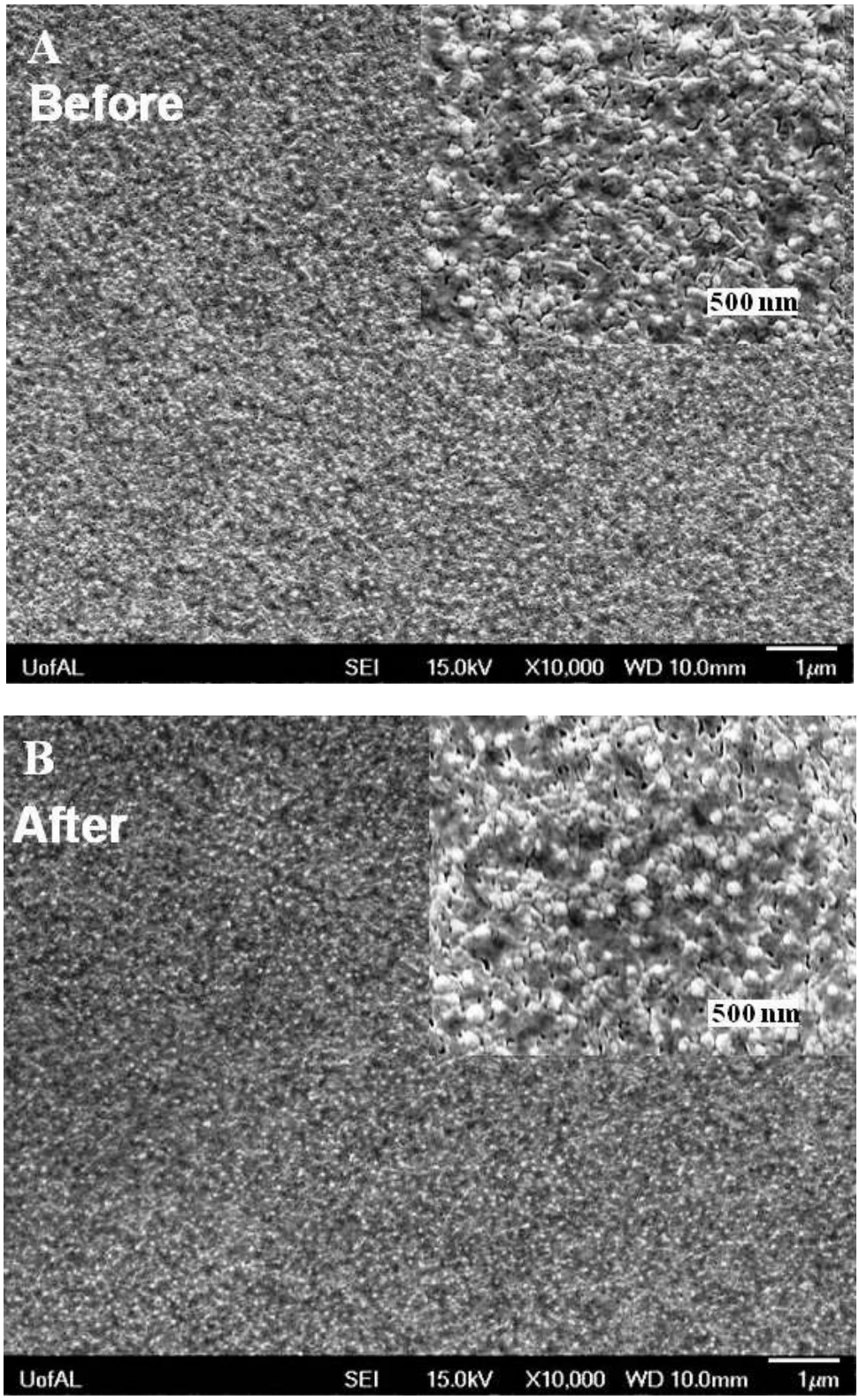

Figure 5.9 SEM of 22 nm hematite (A) before and (B) after applying -1.5 V for 10 s.

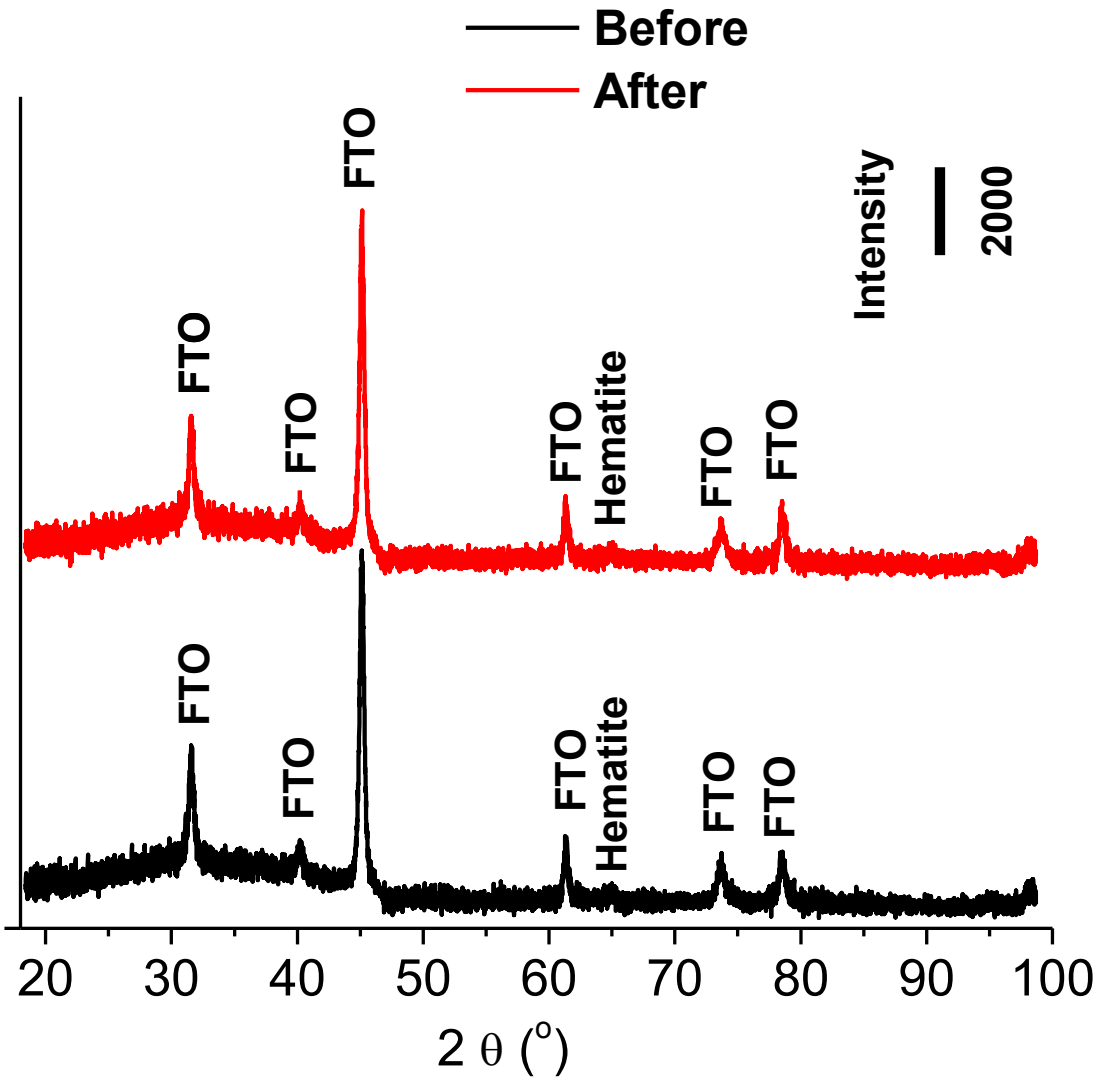

Figure 5.10 XRD pattern of 22 nm hematite on TiO_2 coated FTO substrate before and after applying -1.5 V for 10 s.

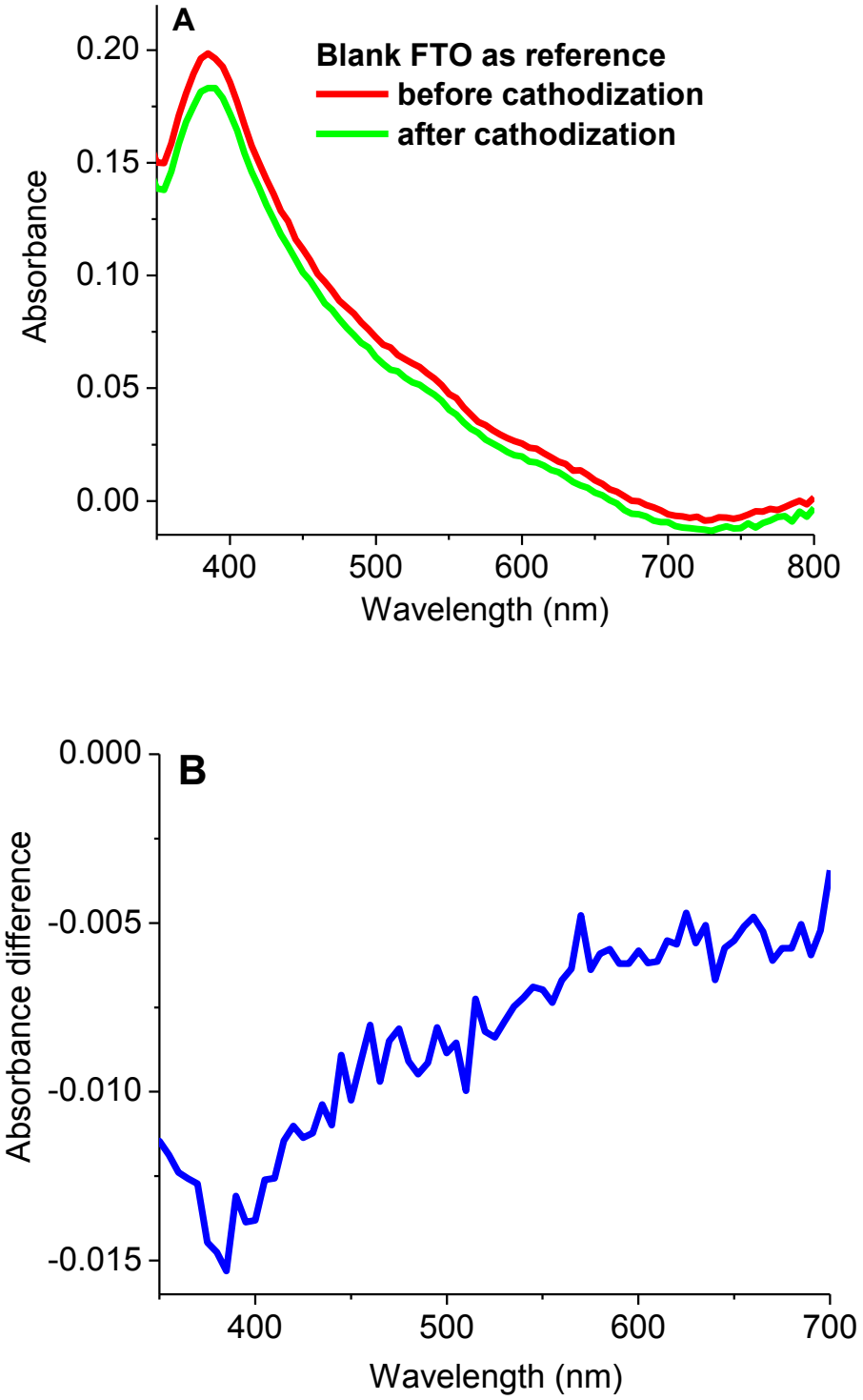

Figure 5.11 (A) absorbance of 22 nm hematite before and after applying -1.5 V for 10 s and (B) the absorbance difference after cathodic reduction.

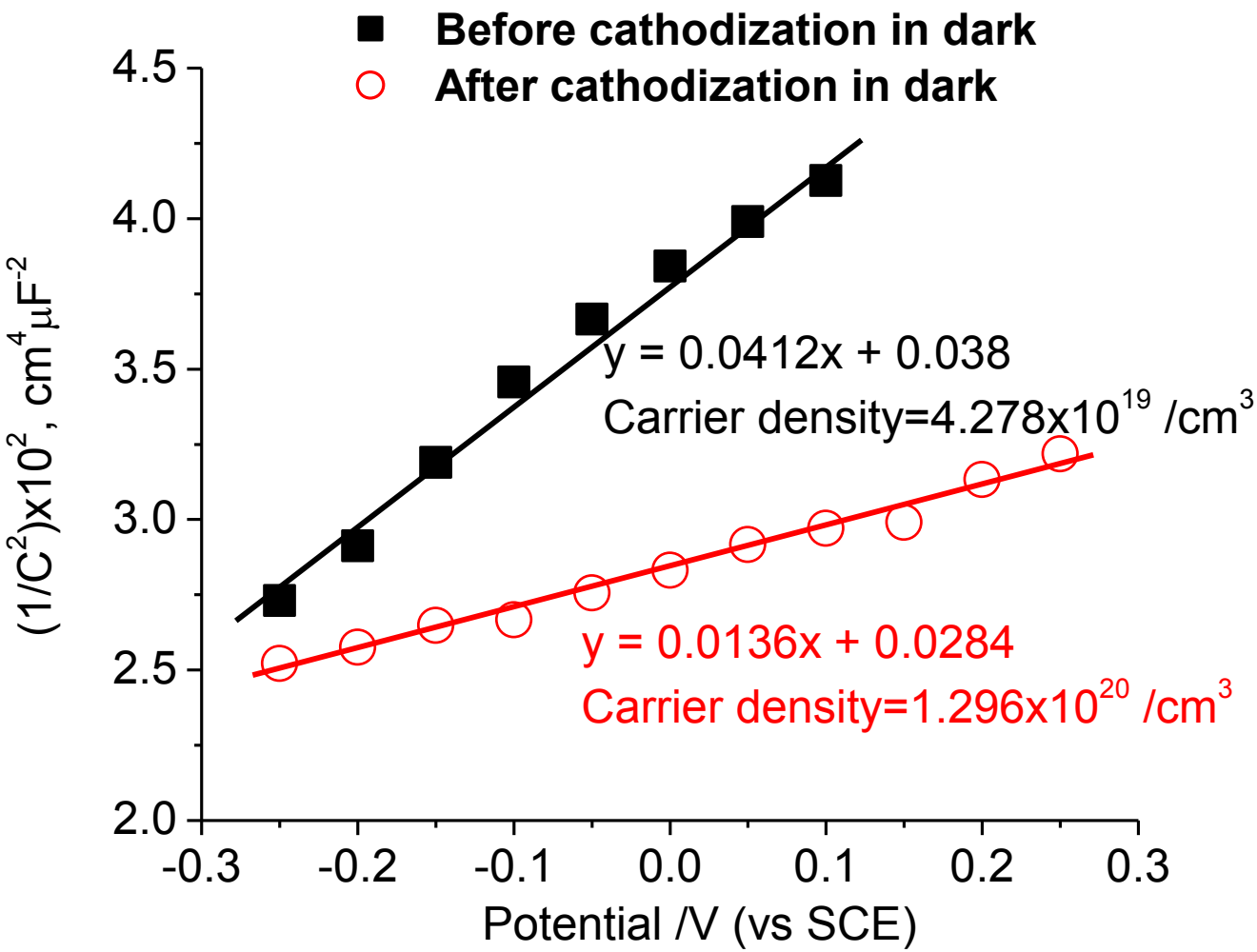

Figure 5.12 Mott-Schottky plot of 22 nm hematite before and after applying -1.5 V for 10 s.

5.4 Conclusions

The cathodization method was demonstrated to be effective in enhancing the photoelectrochemical performance of hematite. The enhancement is attributed to the increase of the carrier density after cathodization because of $Fe^{3+} \rightarrow Fe^{2+} \rightarrow Fe^{0}$. The reduction of $Fe^{3+} \rightarrow Fe^{2+} \rightarrow Fe^{0}$ majorly carries out close to the interface between hematite and substrate. This technique could be possibly applied to other semiconductor photocatalysts to improve their photoelectrochemical performances.

CHAPTER 6

POLYMER-GRAFTED UNIVERSAL TEMPLATE FOR FABRICATION OF NANOWIRE ARRAYS

6.1 Introduction

In addition to enhancing the absorbance of photocatalyst, surface plasmon is also vastly attractive for being applied in Raman Spectroscopy which is nondestructive and fast, but limited by its relative weak signal. Surface plasmon could magnify the Raman signal up to 10^5 – 10^8 times[1] through enhancing the local electromagnetic field or/and initiating a charge transfer between the chemisorbed species and metal surface. However, surface plasomon of metal nanostructures largely depends on their shape, size, and coverage. Therefore, in the fourth and final part of this study, vertically aligned Ag nanostructures with a control over the shape, size, and coverage were successfully prepared based on AAO templates. They were found to be sensitive and reproducible substrates for SERS applications.

This chapter details a study where AAO template was separated from Al substrate by NaOH, H_3PO_4, methanol and DI water, without using harmful $HgCl_2$ and $SnCl_4$, and AAO template was grafted on ITO substrate by a conductive polymer poly(3,4-ethylenedioxythiophene)-poly(styrenesulfonate) (PEDOT:PSS). Ag NWs were successfully electrodeposited in the AAO template on ITO substrate by DC deposition. The length of the Ag nanowires relies on the electrodepositon time and their diameter is determined by the pore size of AAO template which is subjected to the anodization condition such as anodization electrolyte and voltage. These standing Ag NW arrays were explored for the application in SERS.

6.2 Experimental

6.2.1 Surface modification of ITO substrate

ITO coated glass substrates (Colorado Concept Coatings LLC, 12-20 Ω/sq) were sonicated in detergent, DI water, acetone, iso-propanol and DI water for 10 minutes in each agent and finally exposed to ozone (UV/ ProCleaner, BioForce Nanosciences) for 10 minutes. A PEDOT:PSS (Sigma-Aldrich, 2.8 wt %) aqueous solution was spun-coated on ITO substrate at a rotating speed of 3000 rpm. Then it was annealed at 150 °C under nitrogen for 30 minutes to graft the polymers to the surface of ITO substrate. The ungrafted polymer was washed off by DI water.

6.2.2 Preparation of AAO template

Al plate (99.9%, Alfa Aesar) was cleaned in DI water, acetone, isopropanol, DI water for 10 minutes in each step and dried by a nitrogen blow. The clean Al plate was polished in a mixture of $HClO_4$ and ethanol (1:4 v/v) at 20 V and 0 °C for two minutes. Before anodization, the polished Al plate was immersed in 1 M NaOH for 3 minutes to remove the aluminum oxide formed during polish. Then the Al plate was anodized in 0.23 M oxalic acid at 45 V and 20 °C for 45 minutes. The barrier layer formed between the template and Al substrate during anodization was thinned through dropping the anodizing voltage from 45 V to 0.1 V by 5% in every 25 s. Edges of the anodized Al plate were scissored to expose the Al substrate. The AAO template was detached from Al substrate by being dipped in 1 M NaOH, 1.5 M H_3PO_4, methanol and DI water sequentially for about 10 s. Obtained AAO template was immersed in 0.5 M H_3PO_4 at 30 °C for 30 minutes to remove the barrier layer residual at the bottom of the template.

6.2.3 Graft AAO template on ITO substrate

Several drops of DI water/acetone (1:1 v/v) were dripped on PEDOT:PSS modified ITO

substrate and AAO template was floated in the solution. Excess solution was removed by a syringe and samples were dried at room temperature in air. Then the samples were annealed at 120 °C for 30 minutes under vacuum.

6.2.4 Electrodeposition of silver NWs

To prevent electrodeposition of Ag on the area of ITO without AAO template, insulating adhesives were spread at this area except for a strip of ITO was left for electric contact. Electrodeposition was carried out in a three electrode system: a working electrode of prepared sample, a counter electrode of Pt wire and a quasi-reference electrode of Ag wire. All the potential is referenced to Ag wire unless otherwise stated. A solution containing 0.012 M $AgNO_3$ (Fisher Scientific) and 0.32 M H_3BO_3 (Acros Organic) was used as electrolyte. A potential of -0.6 V was applied to electrodeposit Ag. After the electrodeposition, AAO template was wet-etched in 1 M NaOH and insulating adhesives were dissolved by acetone. Ag NWs were washed in DI water for several times and dried at room temperature in air.

6.2.5 Preparation of samples for Raman spectrum

Ag NW arrays were immersed in 10^{-6} M rhodamine 6G (R6G) aqueous solution for 6 hours. Then the samples were soaked in DI water for 45 minutes to remove the unattached R6G molecules and dried in the air.

6.2.6 Characterization

CV was obtained with an Electrochemical Station (CH Instruments, Inc., Austin, TX). A JOEL 7000 field emission scanning electron microscopy was used to characterize the morphology. XRD pattern was measured with a Brukker D8 XRD (Cu source, Kα1, 1.54 Å, 40 kV and 35 mA) at room temperature in air. Raman spectra were collected using a spectrometer

(Jobin Yvon, HR800 UV) equipped with a 633 nm He−Ne laser (2.5 mW). Water contact angle was by measured by Contact Angle Goniometer (Ramé-hart Inc.)

6.3 Results and Discussions

Figure 6.1 details the fabrication process of standing Ag nanowires on ITO substrate. AAO template was obtained by one-step anodization and the barrier layer was thinned by dropping anodizing voltage gradually. After being immersed in 1 M NaOH, 1.5 M H_3PO_4, methanol and DI water, AAO template was detached from Al substrate, without using highly toxic $HgCl_2$ and $ZnCl_4$. The barrier layer at the bottom of AAO template was further removed by dipping the template in 0.5 M H_3PO_4. ITO substrate was carefully cleaned and a layer of PEDOT:PSS was spun-coated on the surface and thermally annealed. Ungrafted polymer was washed away by DI water and a very thin layer of PEDOT:PSS was left on ITO substrate. The water contact angle of freshly cleaned ITO substrate was 20° and it dropped to less than 5° after the PEDOT:PSS modification, indicating PEDOT:PSS is very hydrophilic. Additionally, PEDOT:PSS planarizes the surface of ITO substrate,[2] which in turn enhances the adhesion between AAO template and ITO substrate. Then AAO template was carefully placed on PEDOT:PSS modified ITO substrate. The top side of AAO was used to contact ITO substrate because its surface is smoother than the bottom side.

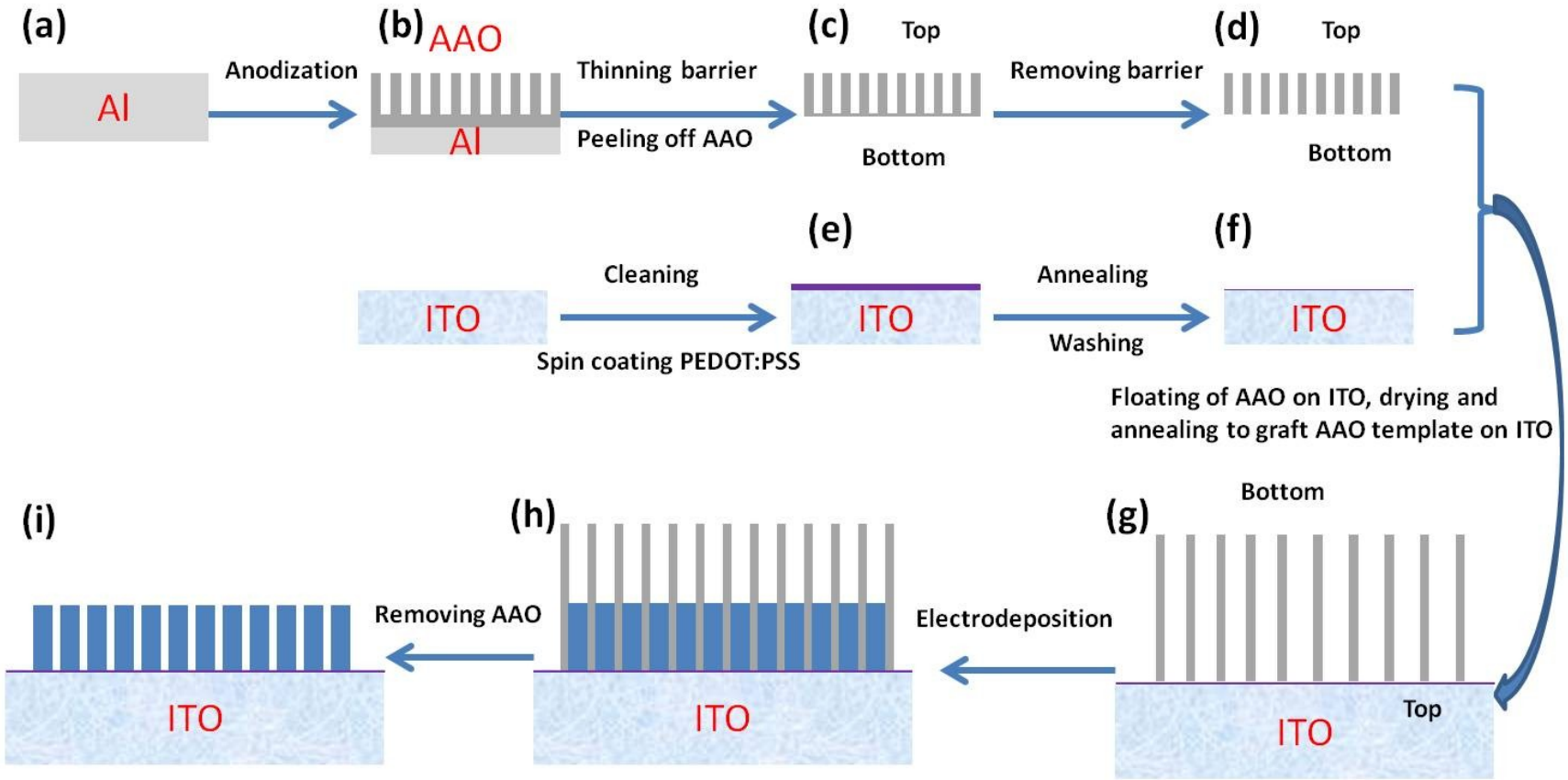

Figure 6.1 The fabrication process of vertically aligned Ag NW arrays on ITO substrate.

Figure 6.2A-E show the morphologies of the top and bottom of an AAO template, the pore diameter distribution of AAO template, and the cross-section of AAO. Figure 6.2B confirms that AAO pores at the bottom are open after H_3PO_4 treatment, which guarantees that the Ag^+ is able to transfer through the AAO pores. Because the pores at the bottom branched during the process of gradually dropping anodizing voltage,[3, 4] the pore size at the top is 83.34±8.51 nm which is larger than 49.25±8.66 nm of the bottom. Gaps between pores are around 10-15 nm and the pore density of the template at the top reaches $10^{14}/ m^2$. The pore size and thickness of AAO template are determined by anodizing conditions (such as anodizing voltage, time, and electrolyte) and the time being etched in H_3PO_4. To obtain an AAO template with a proper thickness for detaching and handling the AAO template easily, the anodization was mantained for 45 minutes. As displayed in Figure 6.2E, an AAO template with a thickness of 10 μm was obtained.

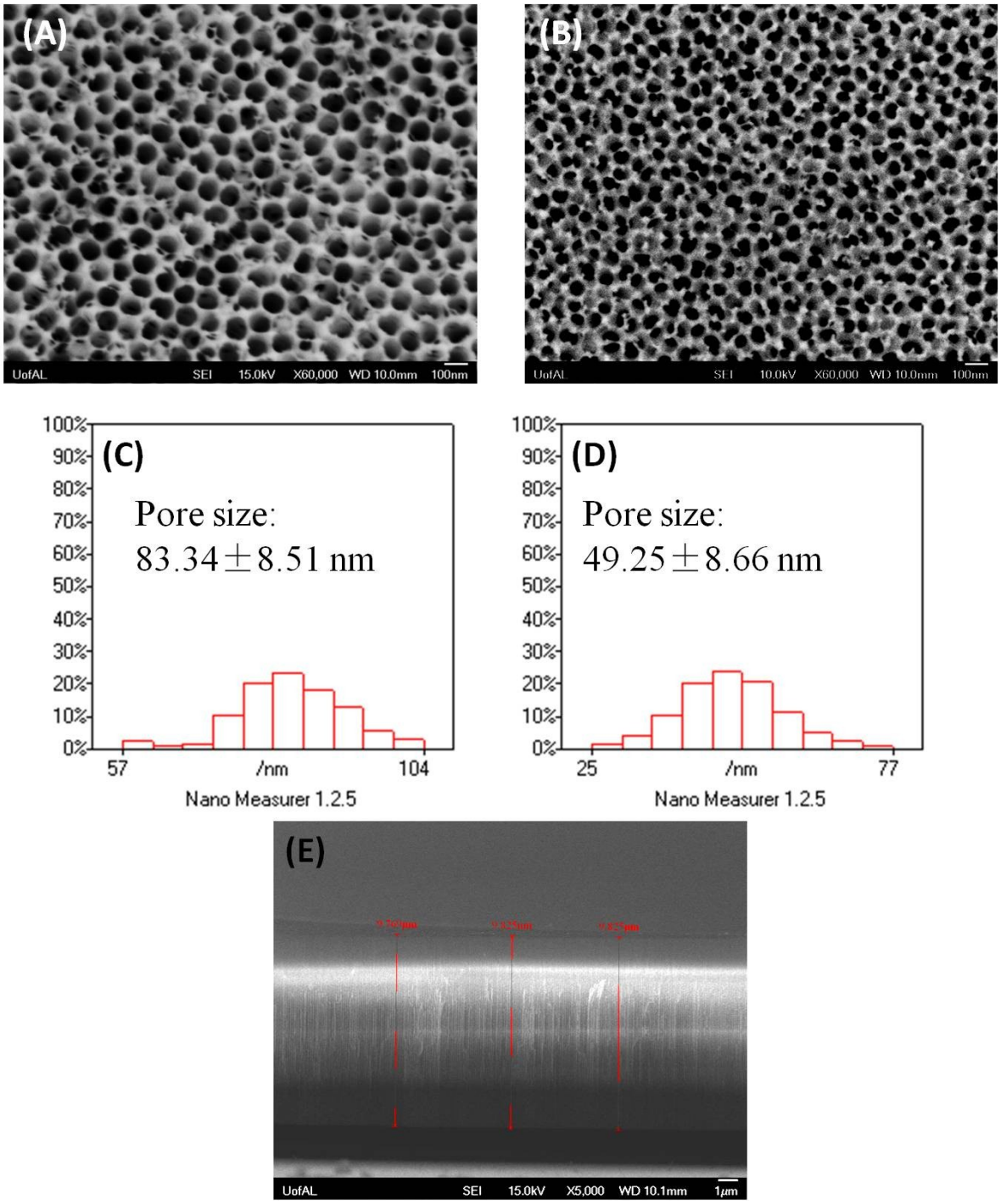

Figure 6.2 SEM images of top (A) and bottom (B) of AAO template; pore size distribution of top (C) and bottom (D) of AAO template; (E) the cross section of AAO template.

Electrodeposition of Ag was carried out in 0.012 M $AgNO_3$ and 0.32 M H_3BO_3 with $AgNO_3$ serving as a Ag source and H_3BO_3 maintaining the pH of the electrolyte to be about 5 for a steady growth of Ag NWs. Prior to the electrodeposition, CV of ITO substrate was performed to locate an appropriate potential for the electrodeposition of Ag NWs. As shown in Figure 6.3, the turn-on potential for cathodic current referring to reduction of Ag^+ is around -0.16 V. As surface roughness is important for SERS, -0.6 V, which is much more negative than the onset potential of cathodic current, was selected to grow Ag NWs at a high growth rate. The fast growth rate is prone to form a large crystal grain and therefore generate a rough surface on the Ag NWs.

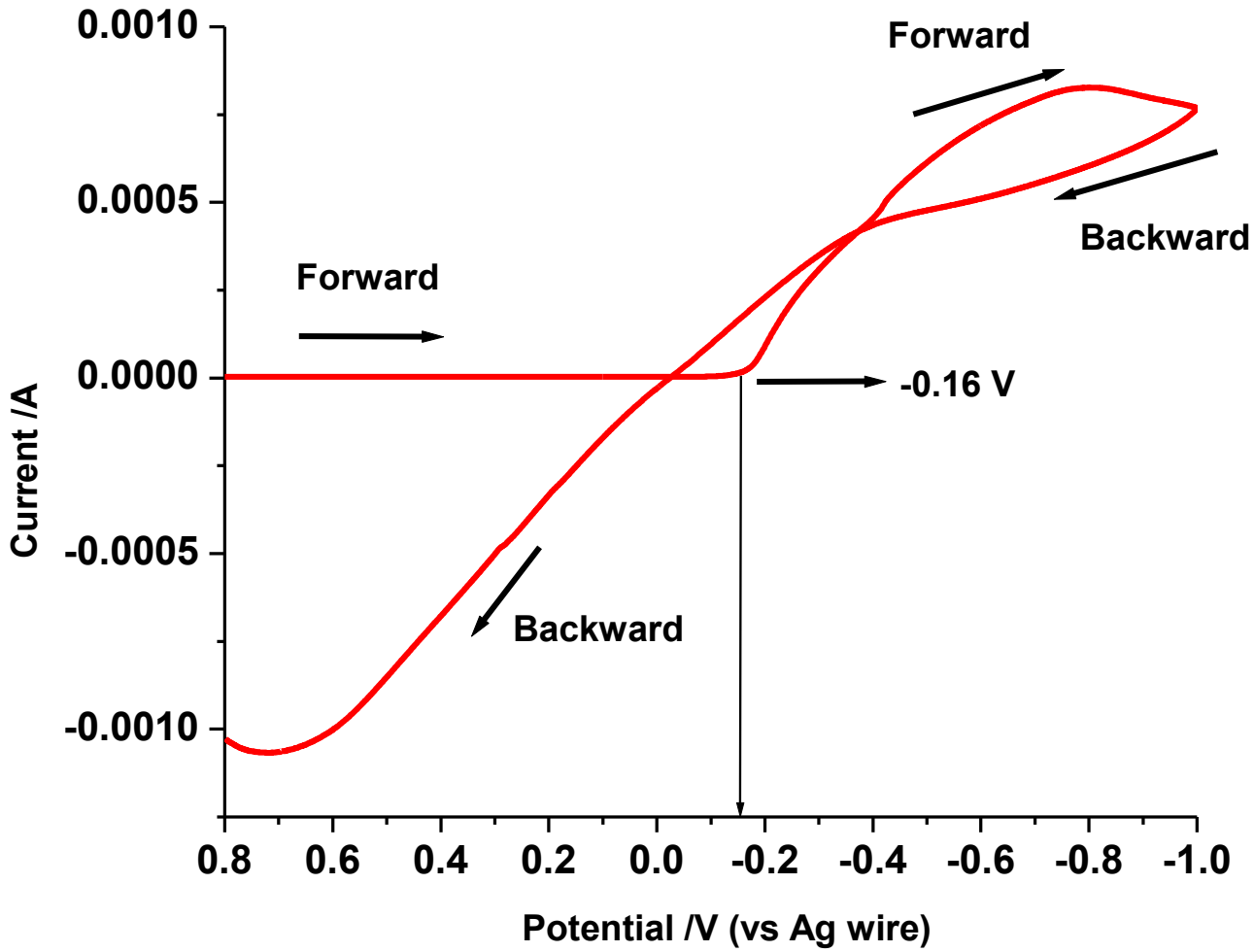

Figure 6.3 CV of ITO substrate in 0.012 M $AgNO_3$ and 0.32 M H_3BO_3.

Electrodeposition of Ag was carried out in 0.012 M $AgNO_3$ and 0.32 M H_3BO_3 at -0.6 V for 50 s. AAO template was etched away by NaOH after electrodeposition, with only Ag NWs left. Images of top and cross-section view of Ag NWs on ITO substrate are shown in Figure 6.4. As shown in Figure 6.4A, Ag NWs are densely packed on ITO substrate with a diameter around 90 nm and a distance from 10 to 15 nm between each nanowires, consistent with the characters of AAO template. In the cross-section view of Figure 6.4B, these Ag NWs are standing perpendicularly to the ITO substrate. The surface of Ag NWs is rough because of the formation of a large amount of small Ag nanoparticles (NPs) on the NW's surface aroused by the fast electrodeposition rate. The length of Ag NWs varies from 200 nm to 1 μm because of the different local conductivity on the surface of ITO substrate and the growth competition between Ag NWs. Normally, standing NW arrays drying out under natural environment are prone to aggregate because of the surface tension of the rinse liquid exerted on the NWs.[5] There are two reasons why these prepared Ag NWs stand vertically on ITO substrate. One is that the Ag NWs are in good contact with ITO substrate as shown in Figure 6.4B, which is a rigid substrate. The other one is that the diameter of the Ag NWs is around 90 nm while the length of is controlled less than 1 μm, so the rigidity of the Ag NWs is able to resist the surface tension from the rinse liquid and prevent the NWs from collapse.

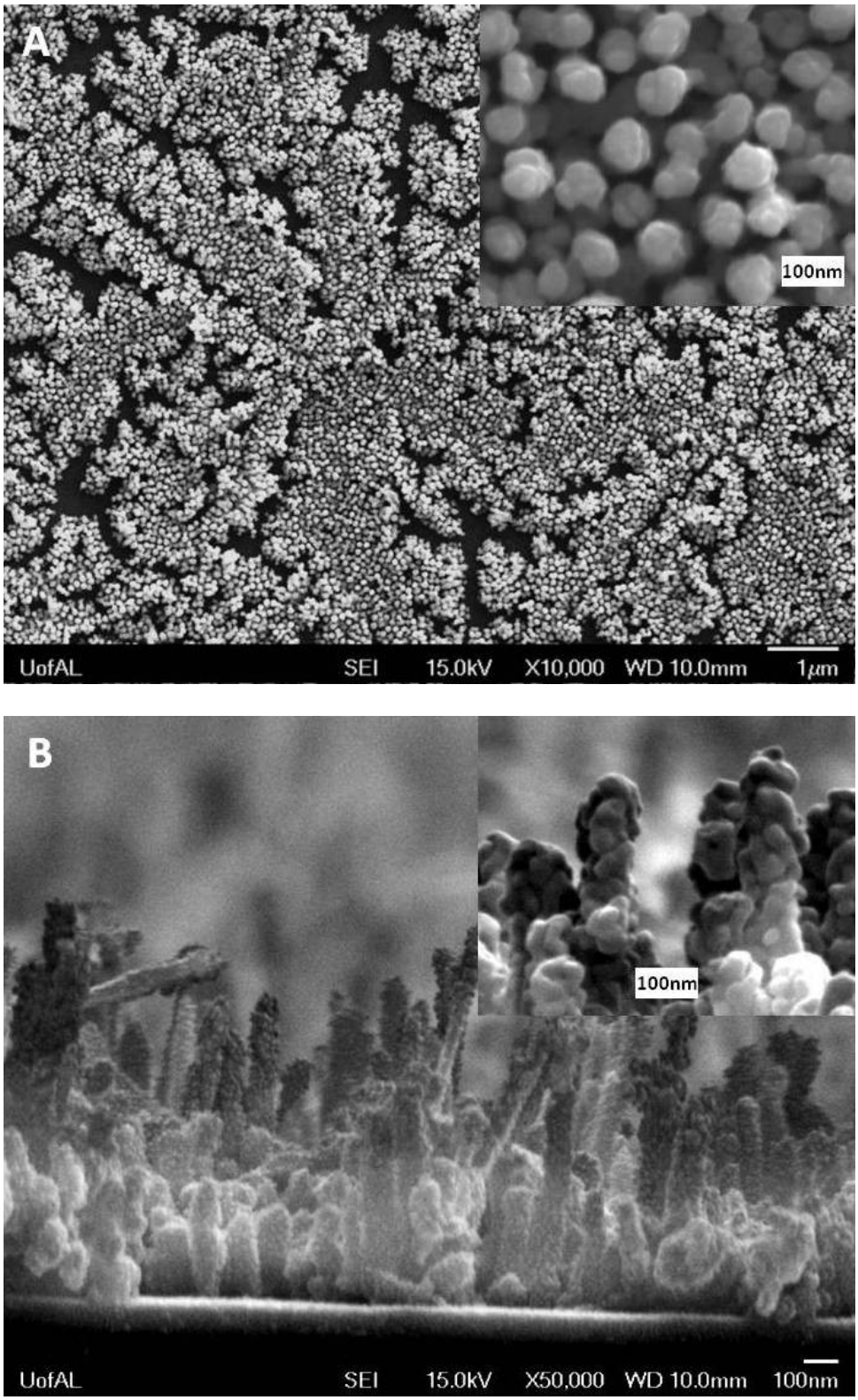

Figure 6.4 Top (A) and cross-section (B) of Ag NW arrays on ITO substrate after removing AAO template.

XRD pattern of Ag NWs on ITO substrate after removing AAO template is shown in Figure 6.5. Peaks center at 2θ=38°, 44.4°, 64.5°, 77.3° and 81.4° are indexed to (111), (2 0 0), (2 2 0), (3 1 1) and (2 2 2) of Ag corresponding to PDF standard card 00-001-1164 from International Centre for Diffraction Data (ICDD). These peaks suggest these Ag NWs are face-centered cubic crystal. The intensity of the peak of (1 1 1) is about 40 times of other peaks, indicating the Ag NWs have very good crystallinity and grow preferentially along the (1 1 1) plane, which has the lowest energy.[6] Other peaks shown in Figure 6.5 are from ITO substrate according to PDF standard card 00-039-1058 of ICDD.

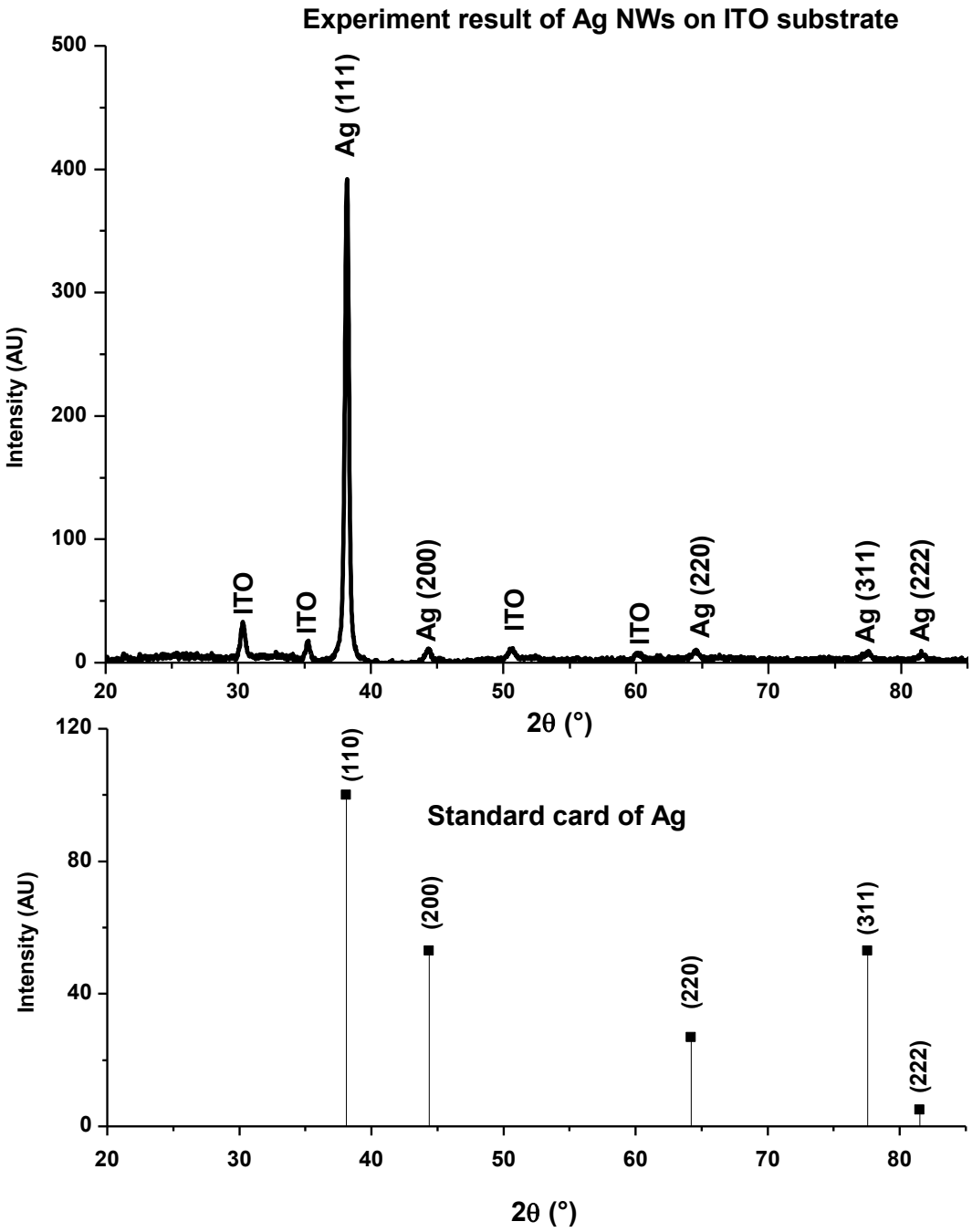

Figure 6.5 XRD pattern of Ag NW arrays on ITO substrate.

Raman spectroscopy is a fast analyzing technique and causes no damage to sample, but the high detection limit narrows its application. SERS, by taking the advantage of surface plasmon of metal (e.g. Ag and Au), could enhance the intensity of Raman signal by a factor of $10^5 – 10^8$ and obtain an extremely low detection limit.[1] Considering the large surface area of the Ag NWs and the small distance between these Ag NWs, the prepared Ag nanowire arrays should be suitable for SERS application. R6G molecules were attached on the Ag NW arrays as probing molecules to study their capability of enhancing Raman signals. Ag NW arrays were immersed in R6G solution to let R6G molecules absorb on the surface of Ag NWs and unabsorbed R6G molecules were washed away by DI water. As seen in Figure 6.6A, when no R6G molecules are attached on Ag NWs, background signals are weak except for one peak at 1466 cm^{-1} corresponding to PEDOT:PSS residues.[7] But since very few signals from R6G fall in the range from 1400 cm^{-1} to 1500 cm^{-1}, the signals from PEDOT:PSS will not cause a problem for the detection of R6G molecules. For the concentrated R6G solution (2 mM) solution dropped on ITO substrate, Raman signals from R6G molecules are very weak and hard to distinguish from the fluorescence background. However, with the same experimental set-up, when Ag NW arrays on ITO substrate are used as the substrate, for 1 μM R6G solution, which is diluted by two thousand times compared to 2 mM R6G solution, high-intensity Raman signals are detected from R6G molecules, demonstrating the SERS sensitivity of the Ag NW arrays. Peaks from R6G molecules are consistent with the literature.[8] To explore the SERS reproducibility of these Ag NW arrays, Raman signals were obtained from six randomly-picked points. As displayed in Figure 6.6B, the peak height, corresponding to SERS intensity, is very close for these six points, indicating the reproducibility of the Ag NW arrays.

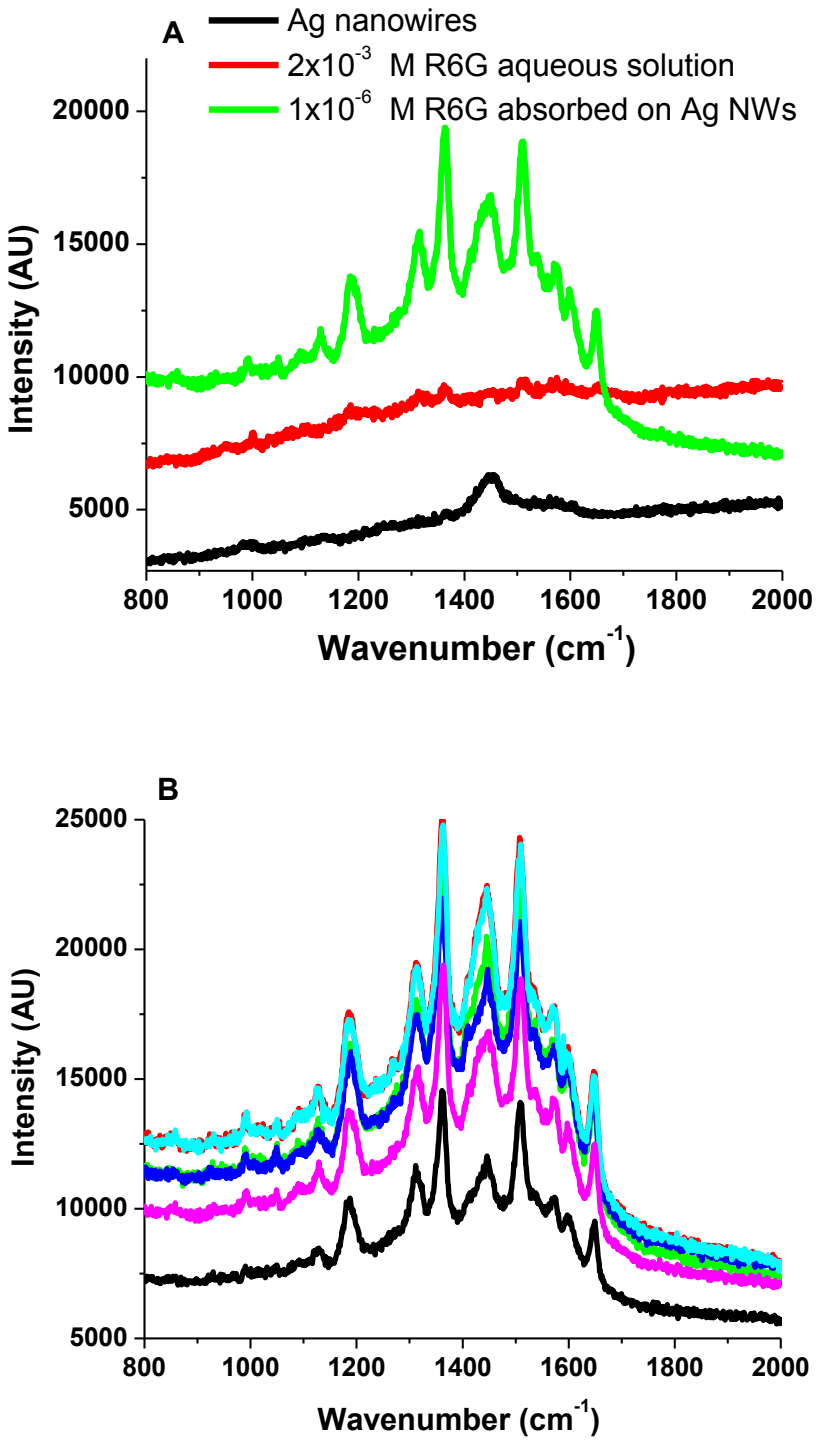

Figure 6.6 (A) Raman spectra from Ag NW arrays, $2x10^{-3}$ M R6G aqueous solution and 10^{-6} M R6G absorbed on Ag NWs (B) Raman spectra of 10^{-6} M R6G absorbed on the surface of Ag NWs at six randomly-picked points.

The strong SERS ability of the Ag NW arrays is attributed to two reasons. The critical one is the electromagnetic field around Ag NWs is dramatically enhanced, so the intensity of incident and scattered light is magnified tremendously by the enhanced field.[9] There are two factors for the electromagnetic field enhancement. The first one is the excitation of surface plasmons of Ag NWs and Ag NPs on the surface. Additionally, the distance between Ag NWs is very short, around 10 to 15 nm, and Ag NPs are densely packed along the Ag NWs. Therefore, the strong coupling between Ag NWs, Ag NPs on the surface of NWs and Ag NWs and Ag NPs happens, which enhances the electromagnetic field around Ag NWs.[10] The other fact worthy noting is that the small Ag NPs on the surface of Ag NWs increase the surface area of Ag NW arrays, which are able to bond more R6G molecules.

6.4 Conclusions

AAO template was successfully grafted on ITO substrate by the conductive polymer PEDOT:PSS. Standing Ag NW arrays were prepared on ITO substrate through electrodeposition of Ag in the grafted AAO template. The Ag NWs, uniform in diameter with different lengths, were found to have a large amount of small Ag NPs on the surface. The Ag NW arrays were demonstrated to be sensitive and reproducible substrates for SERS application.

REFERENCES

(1) Ko, H.; Singamaneni, S.; Tsukruk, V. V. Nanostructured Surfaces and Assemblies as SERS Media. *Small* **2008***, 4*, 1576-1599.

(2) Youn, J. H.; Baek, S. J.; Kim, H. P.; Nam, D. H.; Lee, Y.; Lee, J. G.; Jang, J. Improving the Lifetime of a Polymer Light-Emitting Diode by Introducing Solution Processed Tungsten-Oxide. *J. Mater. Chem. C* **2013***, 1*, 3250-3254.

(3) Furneaux, R. C.; Davidson, A. P.; Rigby, W. R. The Formation of Controlled-Porosity Membranes from Anodically Oxidized Aluminium. *Nature* **1989***, 337*, 147-149.

(4) Ersching, K.; Dorico, E.; da Silva, R. C.; Zoldan, V. C.; Isoppo, E. A.; Viegas, A. D. C.; Pasa, A. A. Surface and Interface Characterization of Nanoporous Alumina Templates Produced in Oxalic Acid and Submitted to Etching Procedures. *Mater. Chem. Phys.* **2012***, 137*, 140-146.

(5) Tanaka, T.; Morigami, M.; Atoda, N. Mechanism of Resist Pattern Collapse during Development Process. *Jpn. J. Appl. Phys.* **1993***, 32*, 6059-6064.

(6) Pan, H.; Sun, H.; Poh, C.; Feng, Y.; Lin, J. Single-Crystal Growth of Metallic Nanowires with Preferred Orientation. *Nanotechnology* **2005***, 16*, 1559-1564.

(7) Stavytska-Barba, M.; Kelley, A. M. Surface-Enhanced Raman Study of the Interaction of PEDOT:PSS with Plasmonically Active Nanoparticles. *J. Phys. Chem. C* **2010***, 114*, 6822-6830.

(8) Hildebrandt, P.; Stockburger, M. Surface-Enhanced Resonance Raman Spectroscopy of Rhodamine 6G Adsorbed on Colloidal Silver. *J. Phys. Chem.* **1984***, 88*, 5935-5944.

(9) Jeanmaire, D. L.; Duyne, R. P. Surface Raman Spectroelectrochemistry: Part I. Heterocyclic, Aromatic, and Aliphatic Amines Adsorbed on the Anodized Silver Electrode. *J. Electroanal. Chem.* **1977***, 84*, 1-20.

(10) Lee, S. J.; Baik, J. M.; Moskovits, M. Polarization-Dependent Surface-Enhanced Raman Scattering from a Silver-Nanoparticle-Decorated Single Silver Nanowire. *Nano Lett.* **2008***, 8*, 3244-3247.

CHAPTER 7

A FACILE METHOD FOR ELECTROCHEMICAL FABRICATION OF VERTICAL-ALIGNED SILVER NANOPLATES THROUGH ANODIC ALUMINUM OXIDE TEMPLATE FOR SURFACE PLASMONIC APPLICATION

7.1 Introduction

As discussed in previous chapter, AAO template is popular for preparing ordered nanomaterials because of its ordered structure and easy fabrication.[1] Most of the research has focused on filling the parallel channels of AAO template to synthesize one-dimensional nanowires.[2, 3] However, AAO template could be also used to prepare two-dimensional nanoplates which are intriguing.

In this chapter, vertical-aligned Ag nanoplates with a relatively uniform thickness were successfully electrodeposited on ITO substrate with the assistance of AAO template. AAO template serves two major functions here. One is that the porous structures lower the diffusion rate of electroactive species (Ag cations) traveling from bulk solution to the surface of ITO substrate. The other one is that the parallel channels of AAO template direct the diffusion of Ag cations. This method may help to understand more about the nanostructure of AAO template and extend the application of AAO template. The absence of surfactant during electrodeposition offers a chemical clean surface for further modification, which benefits the application of the Ag nanoplates in plasmonic catalyzed reaction, plasmonic-enhanced solar cell, and surface enhanced spectroscopy.

7.2 Experimental

7.2.1 Fabrication of AAO template

AAO template was prepared using the same method as chapter 6. Branch structures were generated at the bottom of the AAO template during the process of dropping anodizing voltge, which facilitates the detachment of AAO template from Al substrate. The AAO template was detached from Al substrate by being dipped in 1 M NaOH, 1.5 M H_3PO_4, CH_3OH and DI water sequentially for 10 s after edges of the anodized sample were removed. The AAO template was immersed in 0.3 M H_3PO_4 at 30 °C for 90 minutes.

7.2.2 AAO template transferred on ITO substrate

ITO coated glass substrates (Colorado Concept Coatings LLC, 12-20 Ω/sq) were washed in a sequence of detergent, DI water, acetone, isopropanol, and DI water for 10 minutes in each step and finally anodized in 0.01 M H_2SO_4 acid for 20 minutes. Then several drops of DI water/acetone (1:1 v/v) were dripped on the ITO substrate and AAO template was floated on the solution. Excess solution was removed by a syringe and let samples dry at room temperature in air. To prevent electrodeposition of Ag on the area without AAO template, the area on ITO without AAO template were covered by insulating glue (QUICK DRY) except for a strip of ITO was left for electric contact, leaving an area of 5 mm x 5 mm AAO exposed. The samples were annealed at 80 °C in air for 10 minutes.

7.2.3 Electrodeposition of Ag nanoplates

Electrodeposition was carried out in a solution containing 0.012 M $AgNO_3$ (Fisher Scientific) and 0.32 M H_3BO_3 (Acros Organic) using an Electrochemical Station (CH Instruments, Inc., Austin, TX). Prepared samples served as working electrodes. Pt and Ag wires were applied as the counter electrode and quasi-reference electrode, respectively. All the potentials mentioned in this paper were referenced to Ag wire. Two consecutive potential steps (E_1 and E_2) were selected for electrodepostion of Ag nanoplates according to the CV. E_1 was set

at around -1.5 V and E_2 was -0.2 V. After electrodeposition, AAO template was removed by being dipped in 1 M NaOH for 40 minutes and the sample was rinsed in DI water. The insulating glue was removed by dipping samples in acetone for 30 minutes.

7.2.4 Characterization of Ag nanoplates

XRD data were measured with Cu $K_{\alpha 1}$ radiation (wavelength is 1.54 Å) on a Brukker D8 (40 kV and 35 mA) at room temperature. A JOEL 7000 field emission scanning electron microscopy was used to characterize the samples' morphology. For preparation of samples for Raman measurements, several drops of 10^{-6} M R6G aqueous solutions were dripped on Ag nanoplates and let it dry in the air. Raman measurements were carried out using a spectrometer (Jobin Yvon, HR800 UV) equipped with a 633 nm He−Ne laser (2.5 mW). The accumulation time was 10 s.

7.3 Results and Discussions

Figure 7.1 schematically describes the fabrication process of vertical-aligned Ag nanoplates on ITO substrate with the assistance of AAO template. ITO substrate is cleaned carefully and then anodized in 0.01 M H_2SO_4 which further cleans the surface. AAO template is prepared by one-step anodization. The barrier layer formed at the bottom of AAO template during anodization will be thinned through lowering the anodizing voltage gradually. Because the anodizing voltage decreases step by step, branch structures will be generated at the bottom of the AAO template,[4, 5] which facilitates the detachment of AAO template from Al substrate. The edges of the anodized sample are scissored to expose the Al substrate. When the sample is immersed in 1 M NaOH, the basic solution will attack the AAO/Al interface between the branch structures and Al substrate, generating a large number of hydrogen bubbles and resulting in the separation of AAO template from Al substrate. AAO template is further treated with 0.3 M

H_3PO_4 to remove the barrier layer residue. Then AAO template is carefully placed on the clean ITO substrate and dried at room temperature. The samples are annealed at 80 °C in air to remove the water residue in the AAO template. The electrodeposition of Ag is carried out in $AgNO_3$ aqueous solution with a pH value around 5 and Ag nanoplates grow in the small gap between ITO substrate and AAO template. Finally, the AAO template is dissolved by a basic solution and vertically aligned Ag nanoplates are left on ITO substrate.

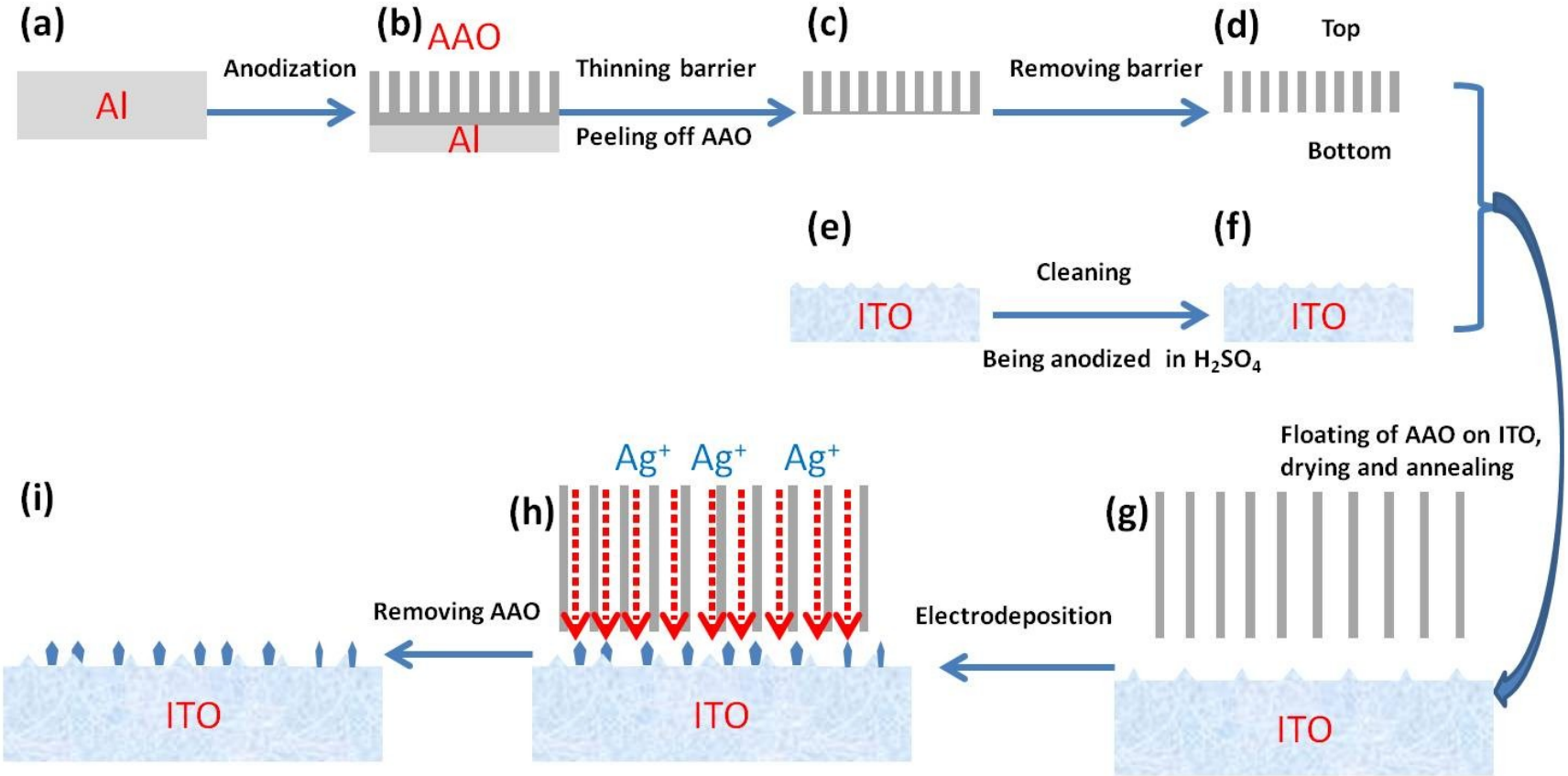

Figure 7.1 Fabrication process of vertically-aligned Ag nanoplates on ITO substrate.

After AAO template was layered on ITO substrate, it is clear in Figure 7.2 that these parallel AAO pores are perpendicular to the surface of ITO substrate, which guarantees the concentration gradient of Ag^+ is perpendicular to ITO surface. Meanwhile, a gap of 288±10 nm between AAO and ITO substrate was clearly shown in the inset picture of Figure 7.2. The formation of the gap is attributed to that ITO substrate and AAO template are hard material with a non-ideally flat surface, which makes it impossible to bind them seamlessly. A gap easily forms between the ITO substrate and AAO template. It is worth noting that the size of the gap will be a little different from sample to sample since the surfaces of ITO substrate and AAO template are not identical for different samples, but it is found that gaps are always to be hundreds of nanometer. The gap can be removed through coating a thin layer of hydrophilic polymer on ITO substrate to generate Ag nanowires in the pores.[6,7]

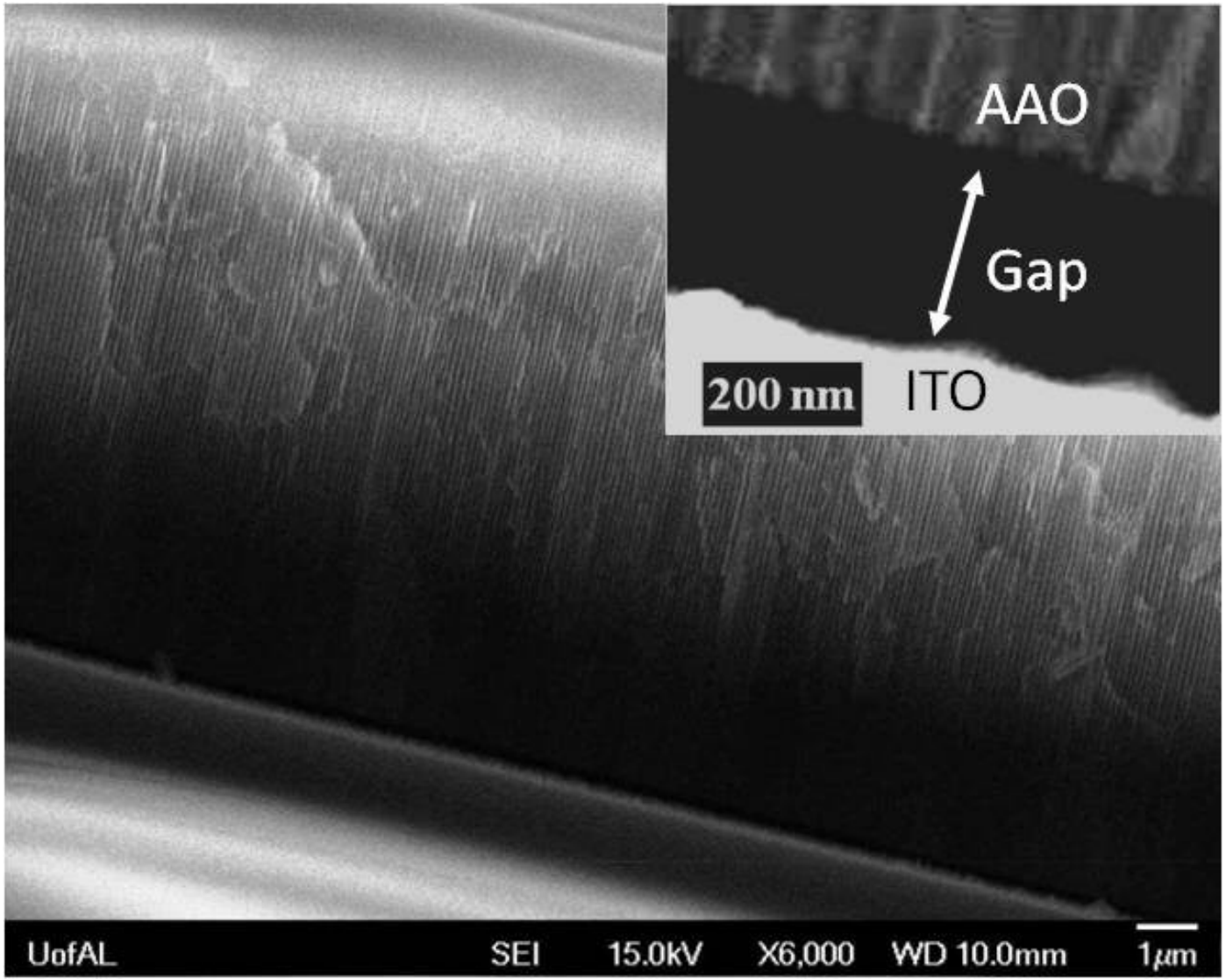

Figure 7.2 Cross section SEM image of AAO template attached on ITO substrate.

All the potential in this paper is referred to a quasi reference electrode of Ag unless otherwise stated. The onset potential of cathodic current corresponding to the reduction of Ag^+ to Ag is -0.16 V from the CV in Figure 6.3 in chapter 6. Therefore, -0.2 V, a little more negative than the onset potential of cathodic current, was selected for electrodeposition, which guarantees the electrodeposition of Ag while maintaining a low growth rate, benefiting the uniformity of Ag nanoplates.

To obtain a narrow the size distribution of Ag nanoplates, a double-potentiostatic method, which includes a short nucleation period and a slow growth period, was adopted to electrodeposit Ag nanoplates on ITO substrate. $AgNO_3$ served as Ag source and H_3BO_3 was used to maintain the pH for a steady growth of Ag nanoplates. There are two periods during the growth of Ag nanoplates. In the period I, a large amount of Ag nuclei were generated by shortly applying a very negative potential E_1-1.5 V which is able to overcome the energy barrier of forming Ag seeds on the ITO substrate.[8] During the period II, an E_2, -0.2 V, chosen according to the CV, was maintained for the growth of Ag nuclei formed in period I. After applying -0.2 V for 200 s, the cross-section image in Figure 7.3A clearly shows the Ag nanoplates were obtained. These Ag nanoplates under AAO template are perpendicular to the surface of ITO substrate and most of them exhibit a height of 500 nm, with some large ones displaying a height of 1 μm. As shown in Figure 7.3B, after the electrodeposition, the gap between AAO template and ITO substrate was enlarged from 288±10 to 1996±11 nm because very large Ag structures generated on very conductive places pushed the AAO template outward. Since the morphologies of top and bottom of AAO template are different as barrier layer residuals rough the bottom of AAO template, electrodeposition of Ag on samples with top and bottom sides of AAO template facing ITO substrate were carried out to explore the influence of the residulals. After electrodeposition,

neither the morphology of top nor bottom of AAO template were changed and no Ag was deposited on the surface of AAO template, suggesting the AAO template could be recycled after usage instead of dissolving it in basic solution. After the AAO template was removed, Figure 7.3C and 7.3D show vertically-aligned Ag nanoplates were prepared in both cases and no difference was observed for these two situations, verifying the barrier layer residual on the bottom of AAO template is not the reason for the formation of Ag nanoplates. Meanwhile no collapse observed after removing AAO template, indicating a good contact was achieved between Ag nanoplates and ITO substrate. In following experiment, to avoid the complication brought by the barrier residual on the bottom side of AAO template and simplify the study of the growth mechanism, all the Ag nanoplates were prepared with the top side of AAO template facing ITO substrate.

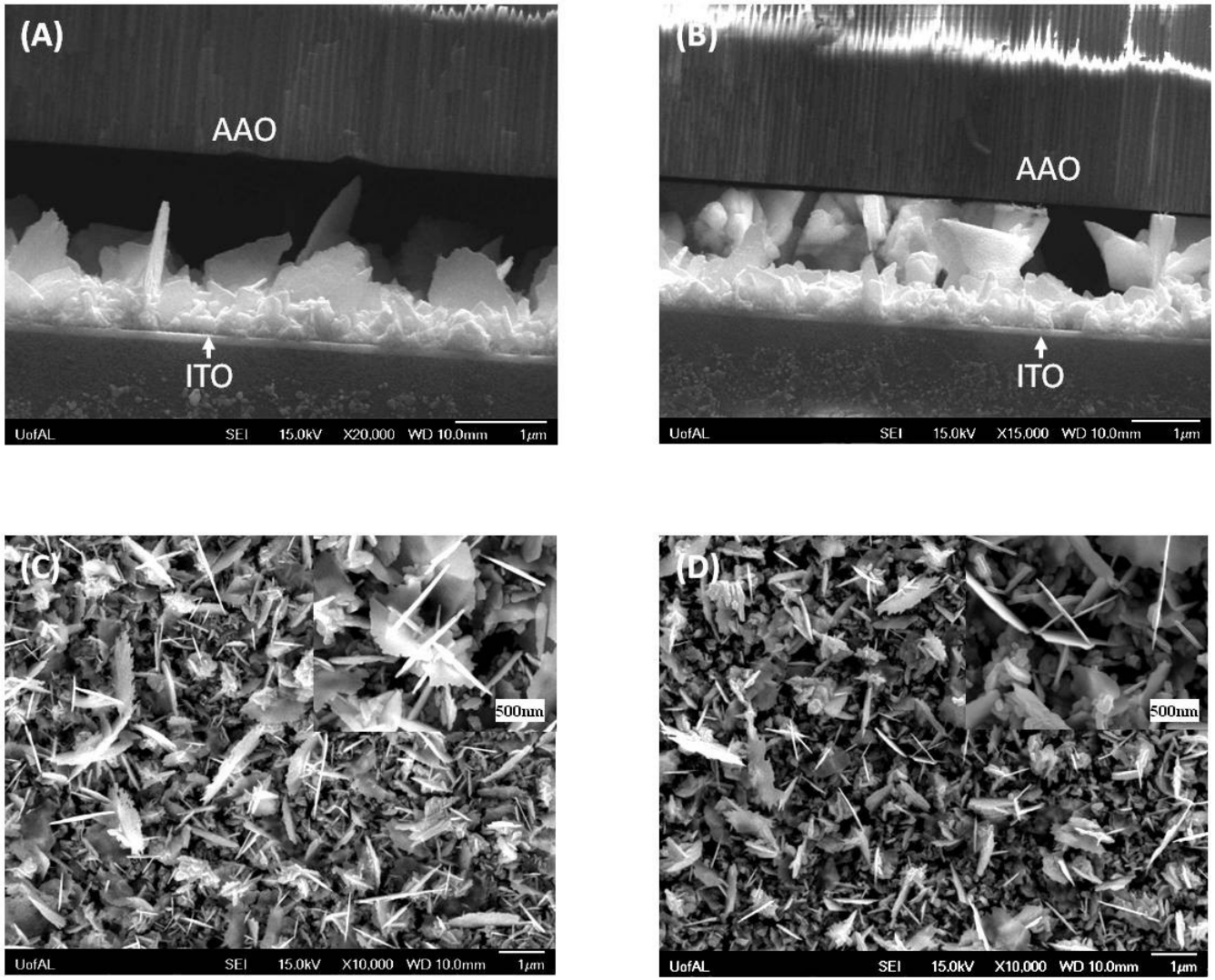

Figure 7.3 (A) and (B) SEM images of Ag nanoplates deposited on ITO substrate under AAO template with top side facing ITO substrate; Ag nanoplates prepared with (C) top side and (D) bottom side of AAO template facing ITO substrate.

To study the growing mechanism of Ag nanoplates under the AAO template, we took SEM images of Ag nanoplates growing at different stages. Figure 7.4A-F show the detailed morphological evolution of Ag nanoplates after applying a growing potential -0.2 V for 0 s, 10 s, 40 s, 120 s, 200 s, and 6000 s, with Figure 7.5A-F displaying the diameter distribution diagrams of Ag nanoplates. In the period I for the seed formation (only applying the nucleation potential -1.5 V for 2 s), small Ag spheres were observed on ITO substrate as shown in Figure 7.4A. The mean size of these seeds is 84.86±49.96 nm. It also should be noted that there are tremendous seeds on the ITO substrate which are too small to be observed and measured under SEM. In the period II (applying the growing potential -0.2 V) for the growth of seeds, Ag seeds formed in period I started to grow. Meanwhile, new seeds will also be produced during this process. According to the seeding/autocatalytic growth mechanism,[9] the reduction of Ag^+ at the seeds is tremendously faster than the generation of new seeds. So we expect to see large Ag nanostructures as well as the small Ag spheres in period II, which are clearly displayed in Figure 7.4B. In Figure 7.4B, instead of nanoplates, Ag branches were observed at the edge of these Ag nanoplates since the growing time is too short to form a perfect Ag nanoplate. The size distribution of Ag nanostructures after 10 s growth is 291.52±311.27 nm, which is broad because of the large Ag branches with a size around 800 nm and relative small Ag seeds with a size about 20 nm both show up. When the growth time increases from 40 to 6000 s as displayed in Figure 7.4C-7.4F, the edges of Ag nanoplates become smoother and smoother, suggesting the branches in Figure 7.5B connect with each other as more Ag^+ ions being reduced. Because more and more Ag nanoplates evolved from the seeds formed in the growing period II show up, the coverage of Ag nanoplates becomes denser and denser with the time increases. The information of the thicknesses and diameters of Ag nanoplates grown with various growing time is listed in Table

7.1. From 40 to 6000 s, the mean thickness of the Ag nanoplates increases from 10.97±1.65 nm to 70.22±13.21 nm and the mean diameter of Ag nanoplates increases from 347.16±131.28 nm to 946.19±171.45 nm, which displays the growth of these Ag nanoplates. However, the information from the mean thickness and diameter of the Ag nanoplates are not able to tell the growth process of each single Ag nanoplate because the generation of new Ag seeds in the growing period II skews the information on the development the diameter and thickness of the seeds formed in the period I. Therefore, the diameter and thickness of the largest Ag nanoplate in the SEM images from 40 to 6000 s is drawn and shown in Figure 7.6, which gives more insight into the evolution process of the Ag nanoplates. In Figure 7.6, the diameter of Ag nanoplate grows faster than the thickness from 40 to 200 s in the initial period. After 200 s, it is found that the 6000 s Ag nanoplates have a smaller diameter than that of 200 s Ag nanoplates but they are much thicker than 200 s Ag nanoplates. It indicates that the diameter of the Ag nanoplates grows at a snail's pace after it reaches a certain value and new Ag seeds are favorable to be generated right on these mature Ag nanoplates and then evolve to Ag nanoplates. This is attributed to the growth competition between the adjacent Ag nanoplates which limits enlargement of Ag nanoplate in diameter and force them to grow in thickness and generateion of new Ag nanoplates, clearly displayed in the inset pictures of Figure 7.4D and 7.4E.

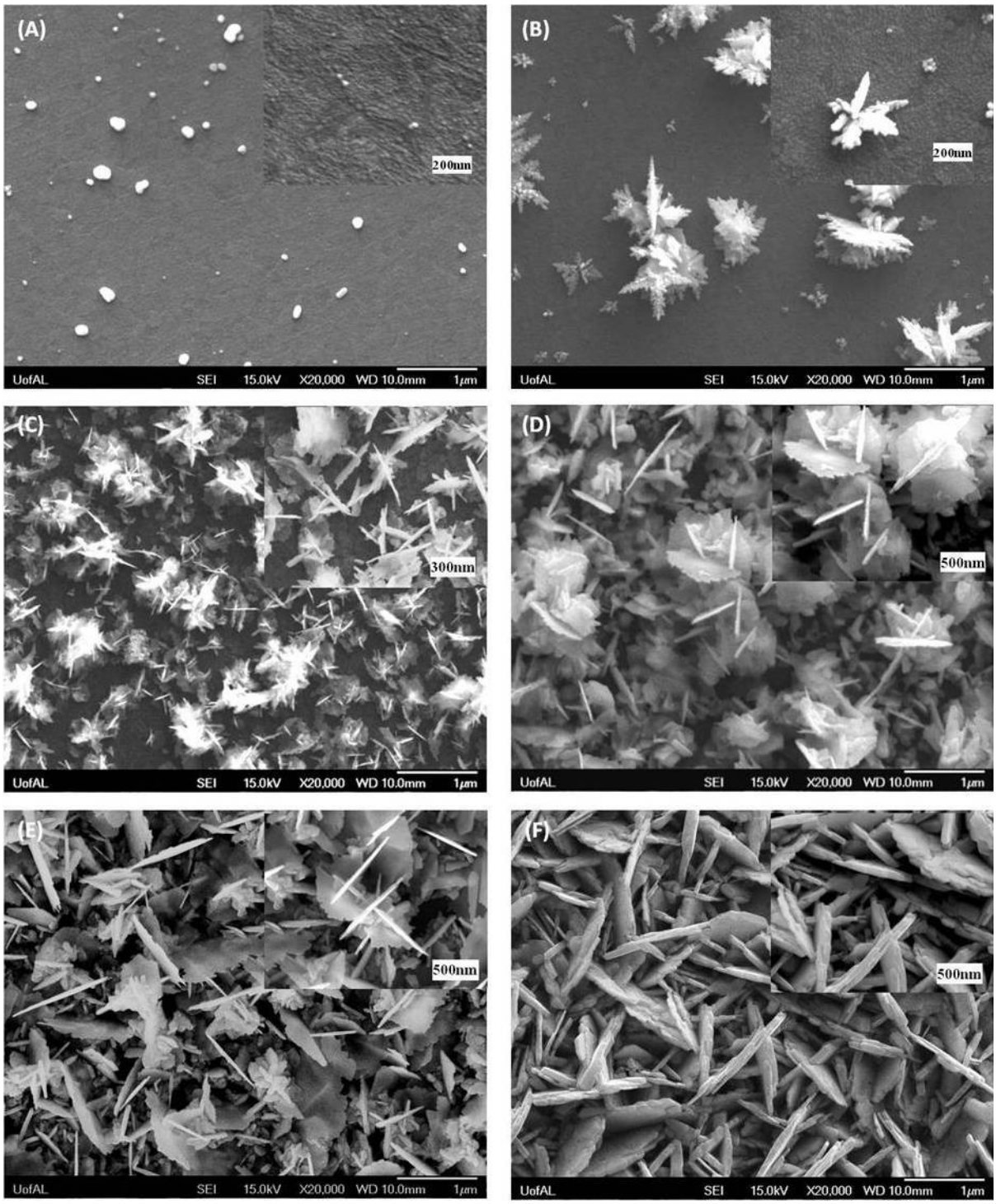

Figure 7.4 SEM images of Ag nanoplates after applying -0.2 V for (A) 0 s, (B) 10 s, (C) 40 s, (D) 120 s, (E) 200 s and (F) 6000 s.

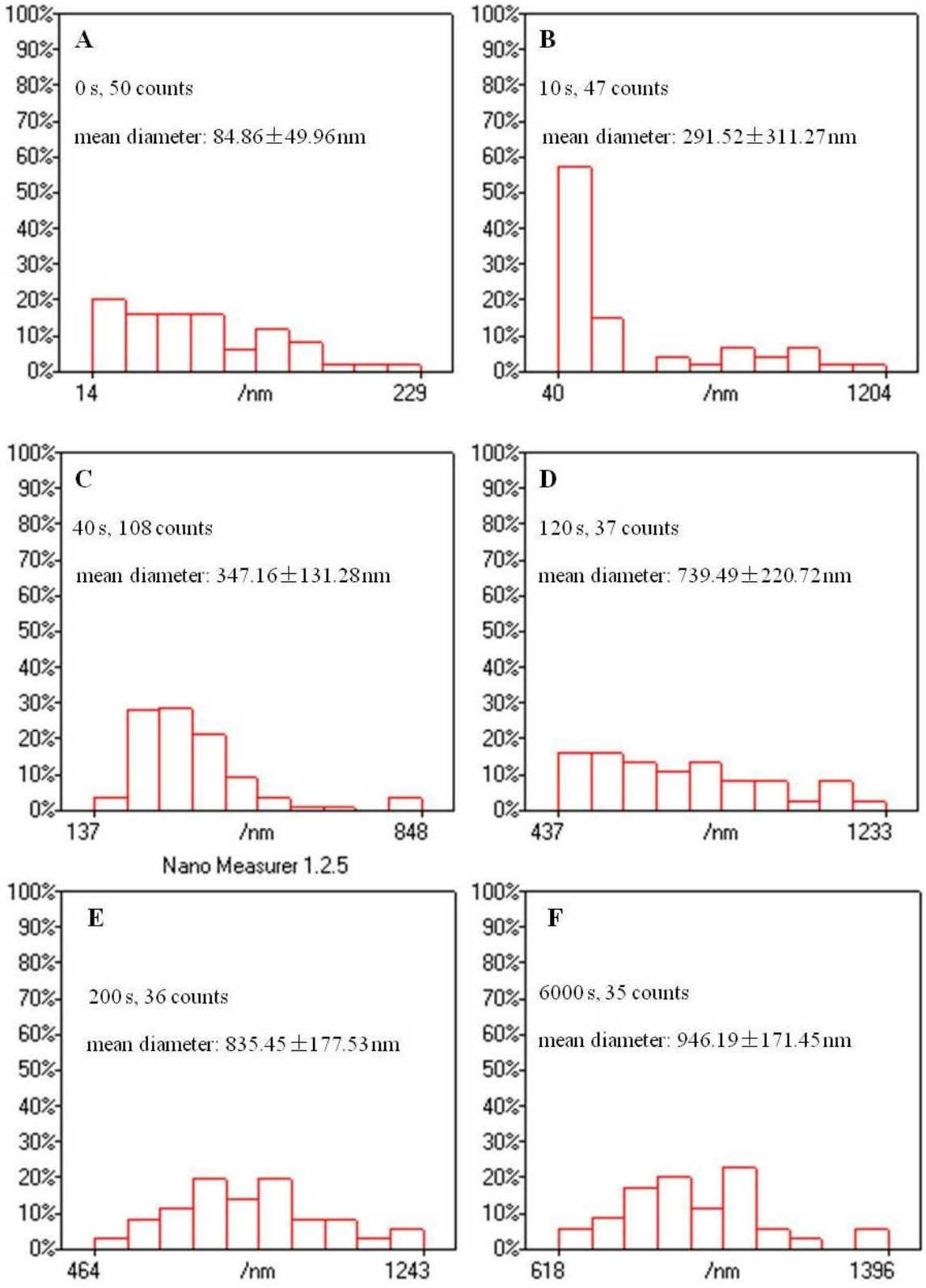

Figure 7.5 Diameter distribution diagrams of Ag nanoplates with various electrodeposition times A: 0 s; B: 10 s; C40 s; D: 120 s; E: 200 s, and F: 6000 s.

E_1= -1.5 V for 2 s	E_2= -0.2 V	Thickness of Ag nanoplates	Diameter of Ag nanoplates
	0 s	N/A	84.86±49.96 nm
	10 s	N/A	291.52±311.27 nm
	40 s	10.97±1.65 nm	347.16±131.28 nm
	120 s	25.79±4.45 nm	739.49±220.72 nm
	200 s	30.10±5.69 nm	835.45±177.53 nm
	6000 s	70.22±13.21 nm	946.19±171.45 nm

Table 7.1 Thicknesses and diameters of Ag nanoplates with various electrodeposition time.

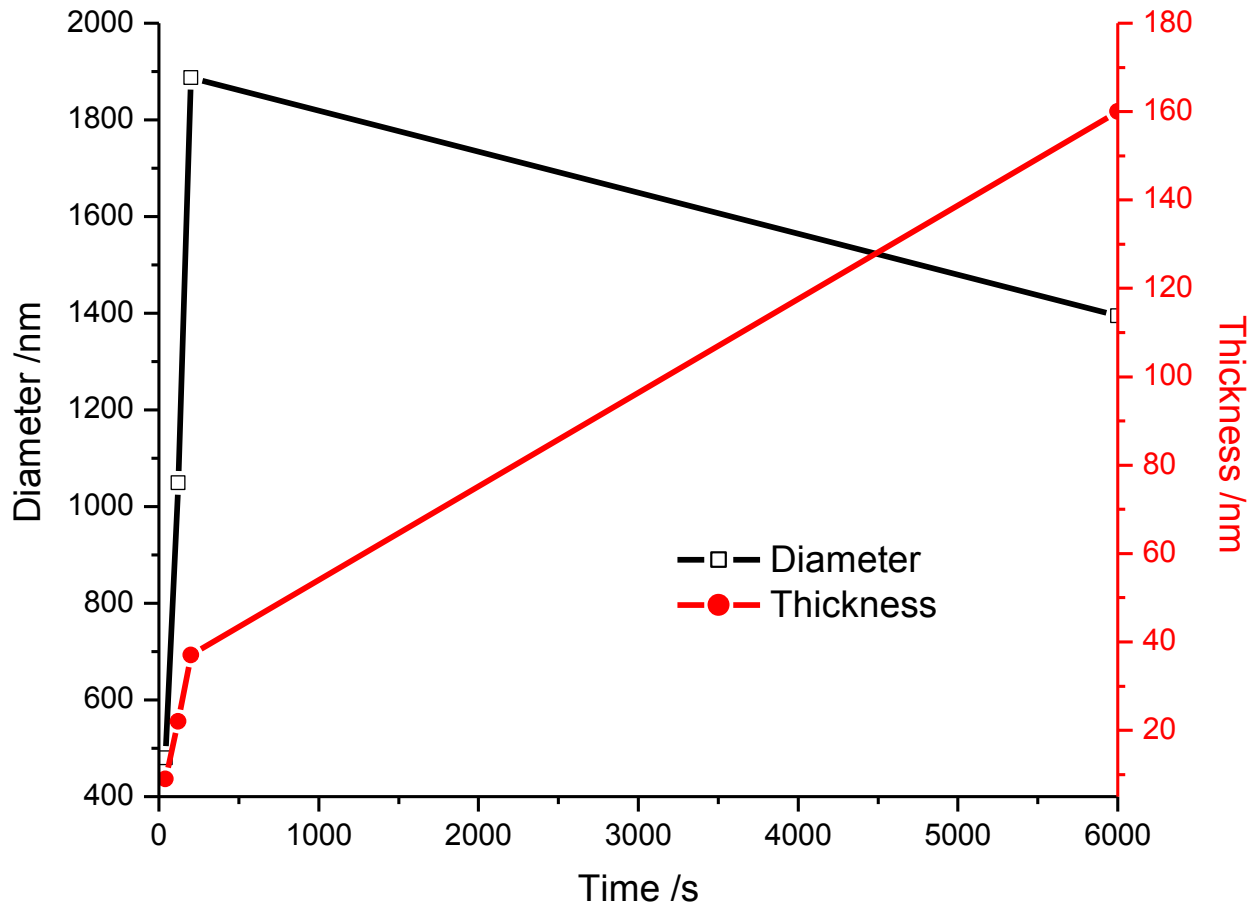

Figure 7.6 Diameter and thickness development of the largest Ag nanoplate with various electrodeposition time.

To explore the function of AAO template in the growth of Ag nanoplates, electrodeposition of Ag on the ITO substrate without AAO template was carried out by applying -1.5 V for 2 s and then -0.2 V for 40 s and 200 s at the same condition, respectively. Without the AAO template, after applying the growth potential for 40 s, the Ag spherical seeds formed in period I developed to irregular Ag spheres as shown in Figure 7.7A because of the spherical diffusion. Small Ag spheres also formed on ITO substrate, attributed to the new formed Ag seeds during Period II. After the growing potential was extended to 200 s, irregular Ag nanostructures were observed in Figure 7.7B. No Ag nanoplates could be formed when AAO template was absent. Meanwhile, when a much more negative potential -0.6 V corresponding to a much faster growing rate was applied for 400 s, Ag NWs grown on a layer of Ag substrate were observed in Figure 7.7C. The gap between AAO template and ITO substrate was filled first and then the electrodeposition of Ag proceeds in the pores to generate Ag NWs, which points out the low growth rate is important for the evolution of Ag nanoplates. In addition, when a layer of PSS:PEDOT polymer was adopted to glue the ITO substrate and AAO template to eliminate the gap between them, vertically aligned Ag NWs were electrodeposited on ITO substrate as discussed in Chapter 6 since electrodeposition of Ag was confined in the parallel pores.

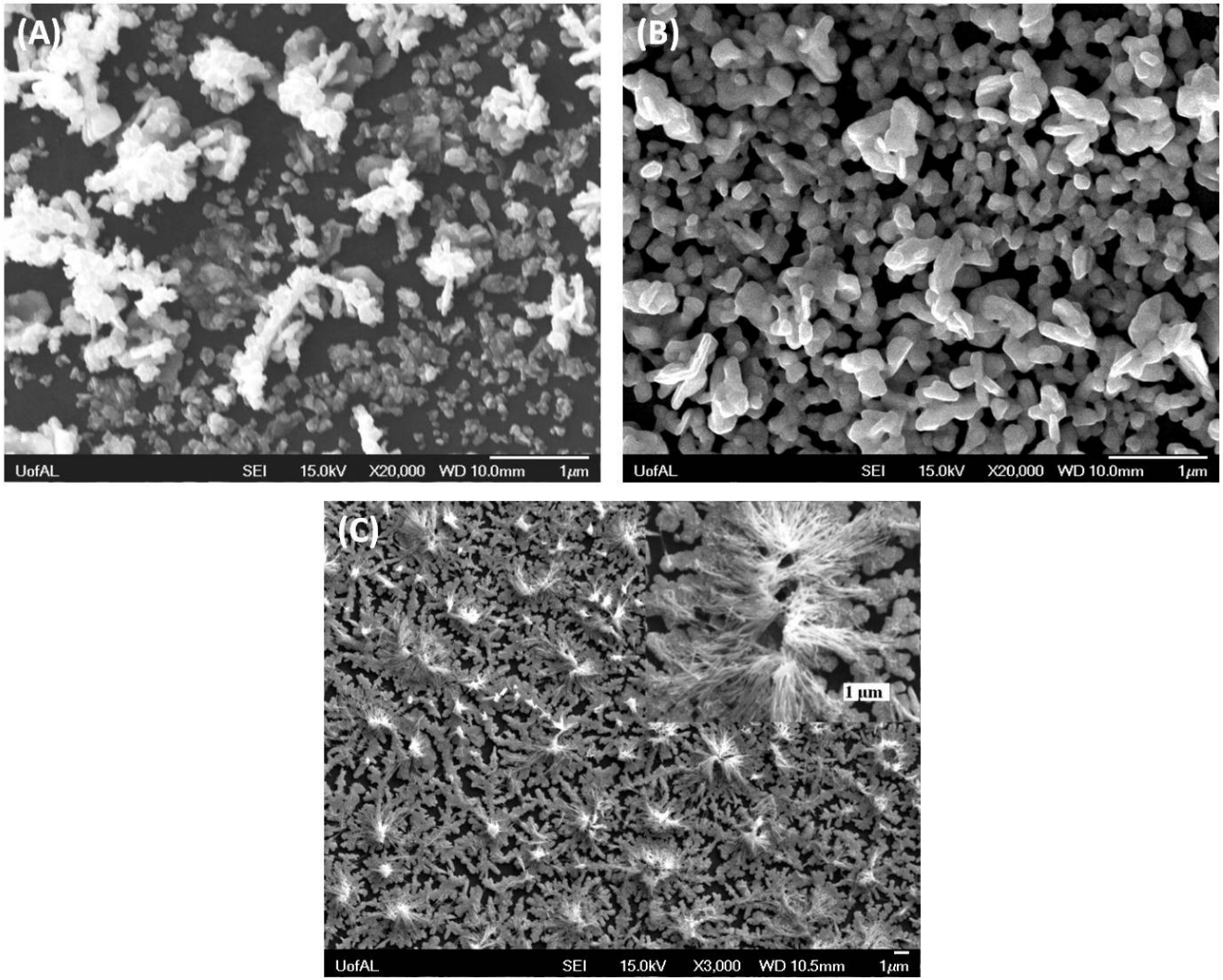

Figure 7.7 SEM images of Ag nanostructures electrodeposited on ITO substrate in the absence of AAO template (A) at -0.2 V for 40 s; (B) at -0.2 V for 200 s, and (C) at -0.6 V for 400 s.

The electrochemical process during Ag nanoplate growth is monitored by the current-time curves of period I and II revealed in Figure 7.8. Since the concentration of $AgNO_3$ in the electrolyte is 12 mM, for a 5 mm x 5mm AAO with a distance of 300 nm to the ITO substrate, there is 9 x 10^{-11} mol Ag^+ in the space between ITO substrate and AAO template, which is equal to a charge of 5.418 x 10^{-6} C. As seen from Figure 7.8, the reduction current in the period I is above 0.5 mA, which means the Ag^+ in the gap could be consumed up in 0.01 s. Therefore, Ag^+ in the gap will be consumed rapidly and Ag^+ in the bulk solution will go through the parallel AAO pores and move towards ITO substrate for continuous reduction. Meanwhile, in period II, it was found the reduction current for the bare ITO substrate is about 20% larger than that when AAO template is present, which is reasonable since AAO template acts similar to a filter which retards the flowing of Ag^+.

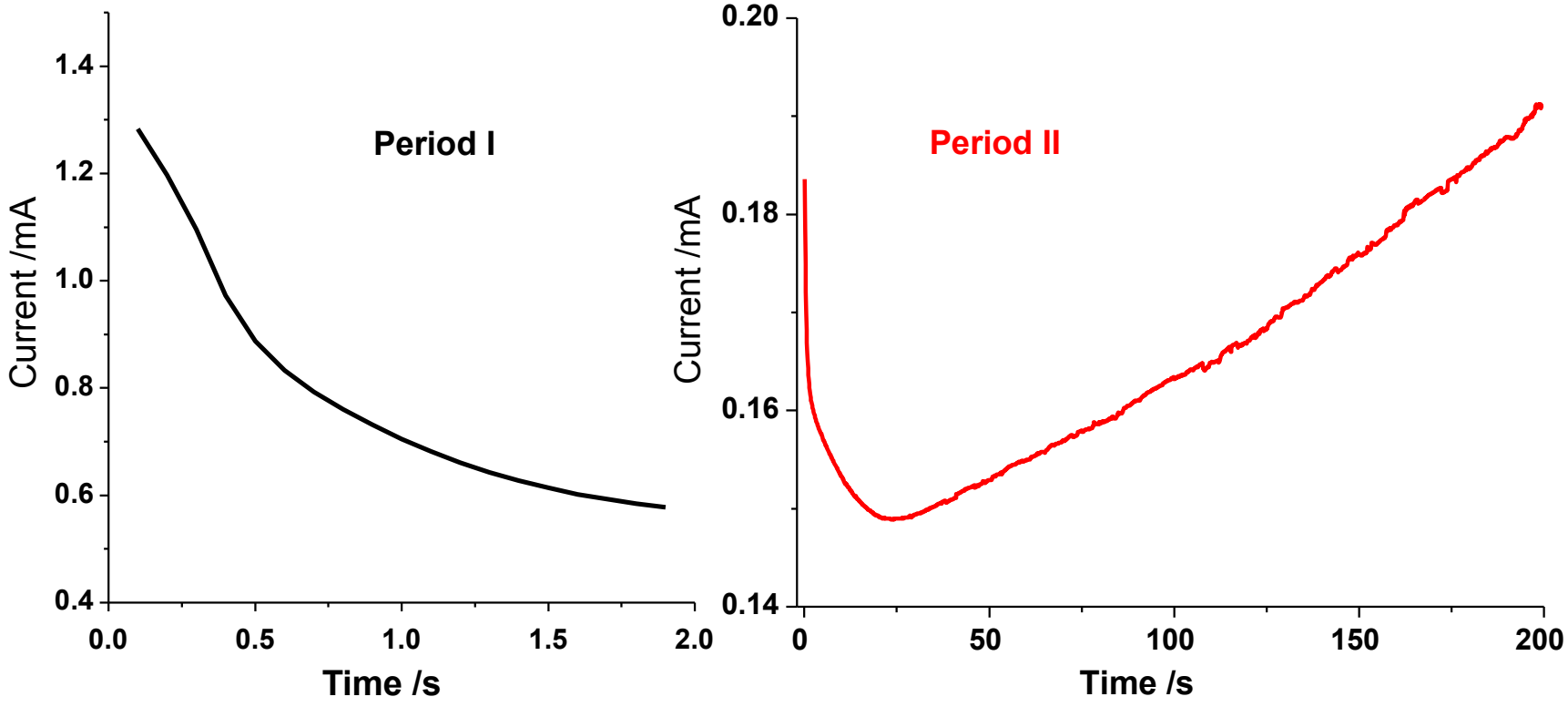

Figure 7.8 Current-time curves of the growth of Ag nanoplates during period I and II.

XRD data of Ag nanoplates on ITO substrate after removing AAO template is shown in Figure 7.9. According to the PDF standard card 00-001-1164 from International Centre for Diffraction Data (ICDD), peaks at 2θ=38.1°, 44.3°, 64.5°, 77.4°, and 81.4° with the relative intensities of 1: 0.32: 0.24: 0.22: 0.07 are indexed to (1 1 1), (2 0 0), (2 2 0), (3 1 1), and (2 2 2) of Ag respectively, respectively, which are a typical diffraction pattern of a face-centered cubic lattice.[10] The strong intensity of (1 1 1) indicates a good crystallinity of Ag which grows through the stacking of the lowest energy facet (1 1 1).[11] In a sense, these Ag nanoplates should be regarded as polycrystalline phase instead of single-crystal structures. Other peaks shown in Figure 7.9 originate from ITO substrate according to the PDF standard card 00-039-1058 of ICDD.

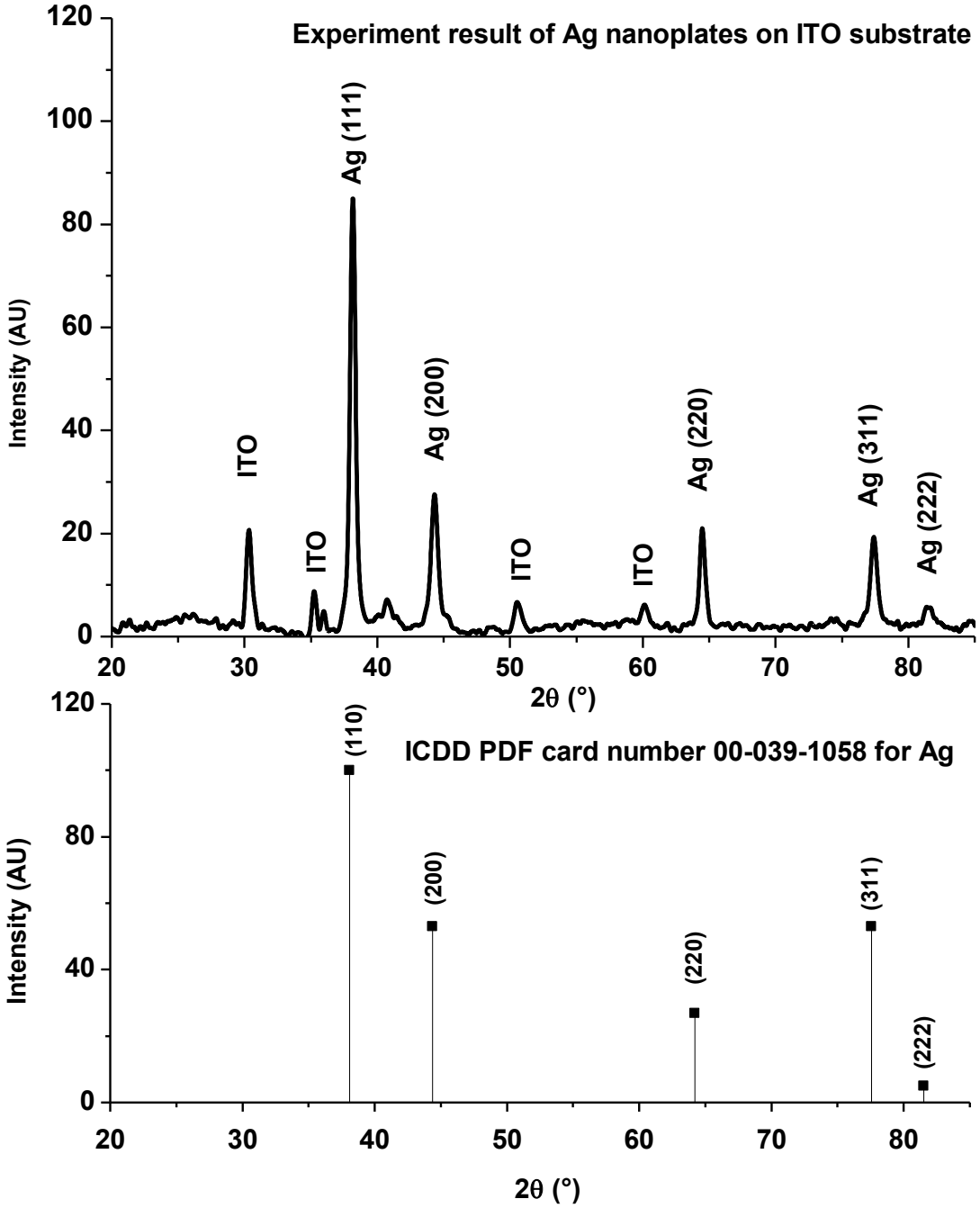

Figure 7.9 XRD patterns of Ag nanoplates on ITO substrate after removing AAO template.

Therefore, based on the results and analysis above, the growth mechanism of the Ag nanoplates is proposed in Figure 7.10 as follows: (A) in period I, Ag seeds are generated on ITO substrate by a potential more negative than the nucleation potential; (B) in period II, the low reduction rate of Ag cations deviates the growth of seeds from sphere shape and triggers the asymmetric growth because of the stacking fault, forming the branch-like structure. The electrical field also induces new nuclei on ITO substrate and the sharp edges of branches, but the rate of generating new seeds is much slower than that of growth of formed seeds; (C) different to the spherical diffusion of Ag^+ around the Ag nuclei when AAO template is absent, Ag^+ concentration gradient is perpendicular to the ITO surface in the presence of AAO template because AAO template is very close to the ITO substrate and its perpendicular and parallel pores confines the diffusion of Ag^+. Therefore, Ag^+ diffuses perpendicularly to the surface of ITO substrate to be reduced to Ag at the Ag seeds. Because of the small gap between ITO substrate and AAO template, the growth of Ag seeds is not limited in the pores of AAO template, instead, along the preferable (111) facet which has the lowest energy, generating small nanoplates. (D) with Ag^+ continuously being reduced, the growth of Ag nanoplates and generation of new Ag seeds go on. Ag nanoplates become larger and thicker with a larger and larger coverage of Ag nanoplates on the ITO substrate. After reaching the critical value of size, the diameter of Ag nanoplates almost stop growing with a preferable growth in thickness. The generation of new Ag seeds on the mature Ag nanoplates begins and producing Ag nanoplates repeats.

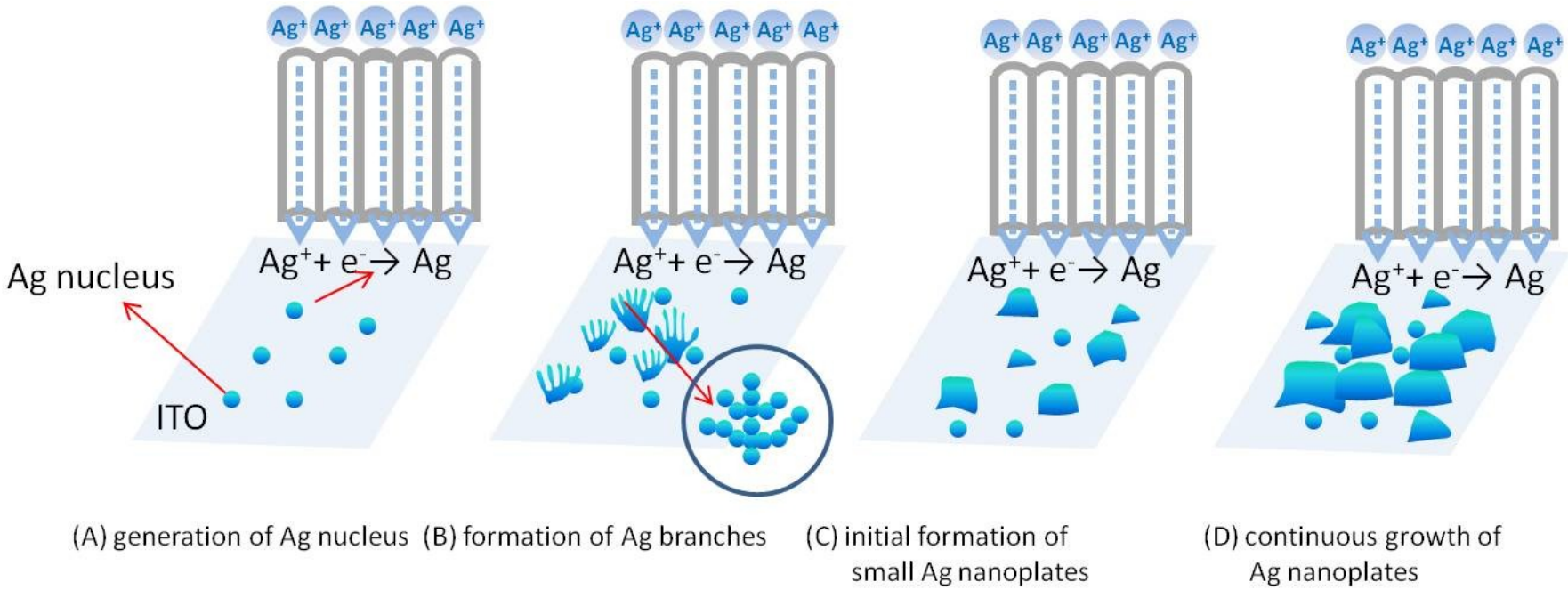

Figure 7.10 Illustration of the growth mechanism of Ag nanoplates under AAO template.

The surface of as-grown Ag nanoplates is chemical clean since no surfactant was added during the preparation, which enables them to be easily modified and benefits their application in SERS. Meanwhile, the coverage, mean thickness, and mean diameter of Ag nanoplates increases with the growth time while the SERS enhancement depends on the particle size and the separation distances between Ag particles.[12] Therefore, it is expected that there is an optimum growth time to obtain the strongest SERS enhancement where Ag nanoplates prepared under this situation displays a suitable size with a interparticle distance within 10 nm. R6G is chosen for studying the influence of coverage, thickness, and diameter of Ag nanoplates on the SERS enhancement because it is photo stable and has been broadly researched in SERS area. During the measurement, each sample was tested three times from three randomly-picked points. The spectra from the same sample display a similar peak height and fluorescent background with no site dependence, exhibiting a good reproducibility of the Ag nanoplates. Figure 7.11 displays the SERS spectra of 10^{-6} M R6G molecules on Ag nanoplates prepared under a different growth time and all peaks in the spectra are consistent with the fingerprint features in literature.[13] In Figure 7.11, no SERS enhancement was observed for the Ag nanoplates with 10 s growth time because the low coverage of Ag nanoplates weakens the coupling effect between Ag nanoplates. With the growth time increases, the coverage of Ag nanoplates on ITO substrate becomes denser and denser with a stronger coupling effect, resulting in a larger and larger fluorescent background. Weak Raman peaks from R6G molecules show up as well. When the growth time reaches 200 s, R6G Raman peaks become distinctive. However, the Raman signal and fluorescent background turn out to be very weak when the growth time extends to 6000 s although the coverage of Ag nanoplates is high. There are two reasons for the decrease of Raman signal and fluorescent background. One is that the Ag nanoplates prepared at 6000s are too large and thick that surface

Plasmon of Ag shifts to the red which lowers the absorbance of the light. On the other side, when the metal particle size increases, especially for very large particles, an enhancement in the scattering efficiency happens accompany with the increase in the electromagnetic field, which further lowers the Raman signals because of less light being absorbed to excite the surface plasmon with a more efficient scattering. The results demonstrate that the Ag nanoplates with suitable size and thickness exhibit a SERS enhancement from the surface-plasmon enhanced local electrical fields which depends on the size, thickness, and coverage of Ag nanoplates.

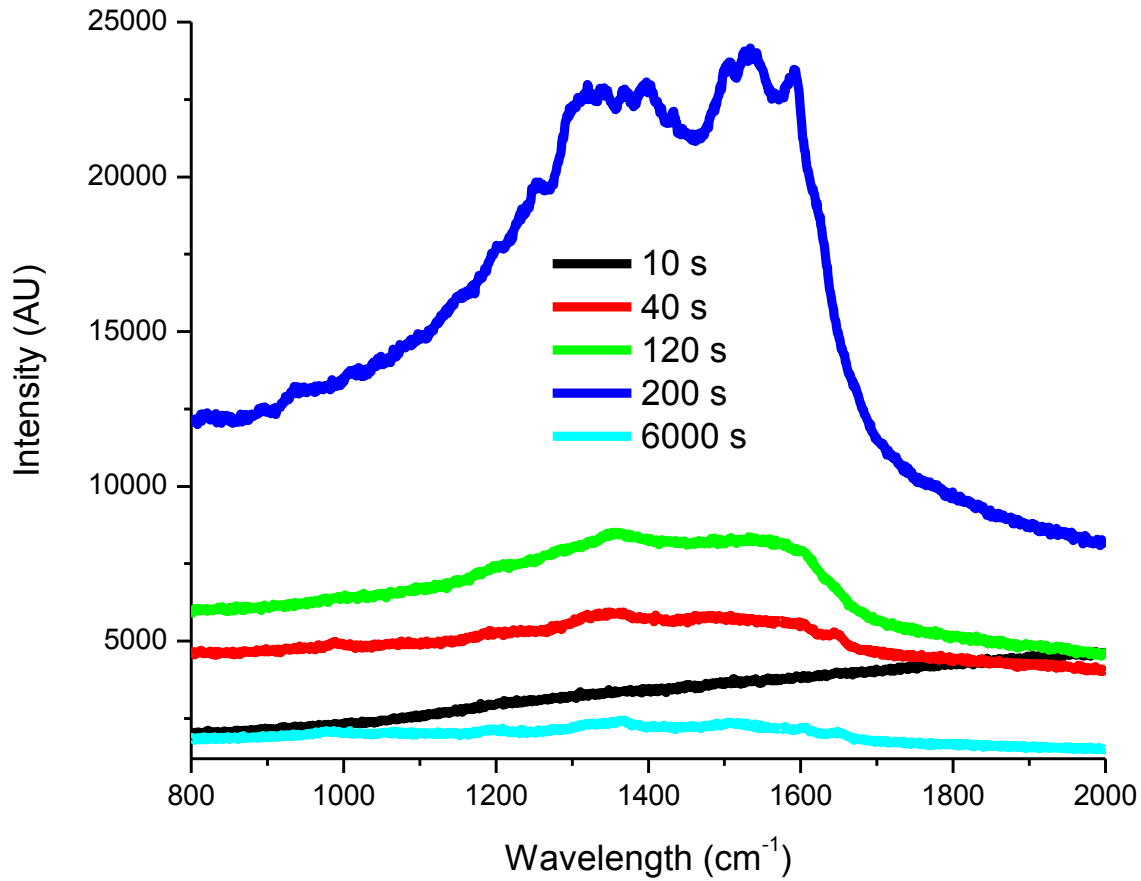

Figure 7.11 Raman spectra of R6G molecules on Ag nanoplates with various growth time.

In addition to AAO template, polystyrene (PS) template is also an admired option serving as a sacrificial template for preparing nanostructure because of its wide tunability over the diameter of PS spheres. PS spheres could be self-assembled on substrates and form an ordered structure, as shown in Figure 7.12A with 2 μm PS spheres patterned on ITO substrates. The ordered structure is able to function as a template and could be easily etched by organic solvent, such as toluene. Figure 7.12B displays Ag NWs bundles electrodeposited on ITO substrate through PS template after removing PS template by immersing the sample in toluene. The Ag NW bundles mimic the morphology of PS spheres and the pattern of PS template, suggesting the PS template directs the growth of Ag NW bundles.

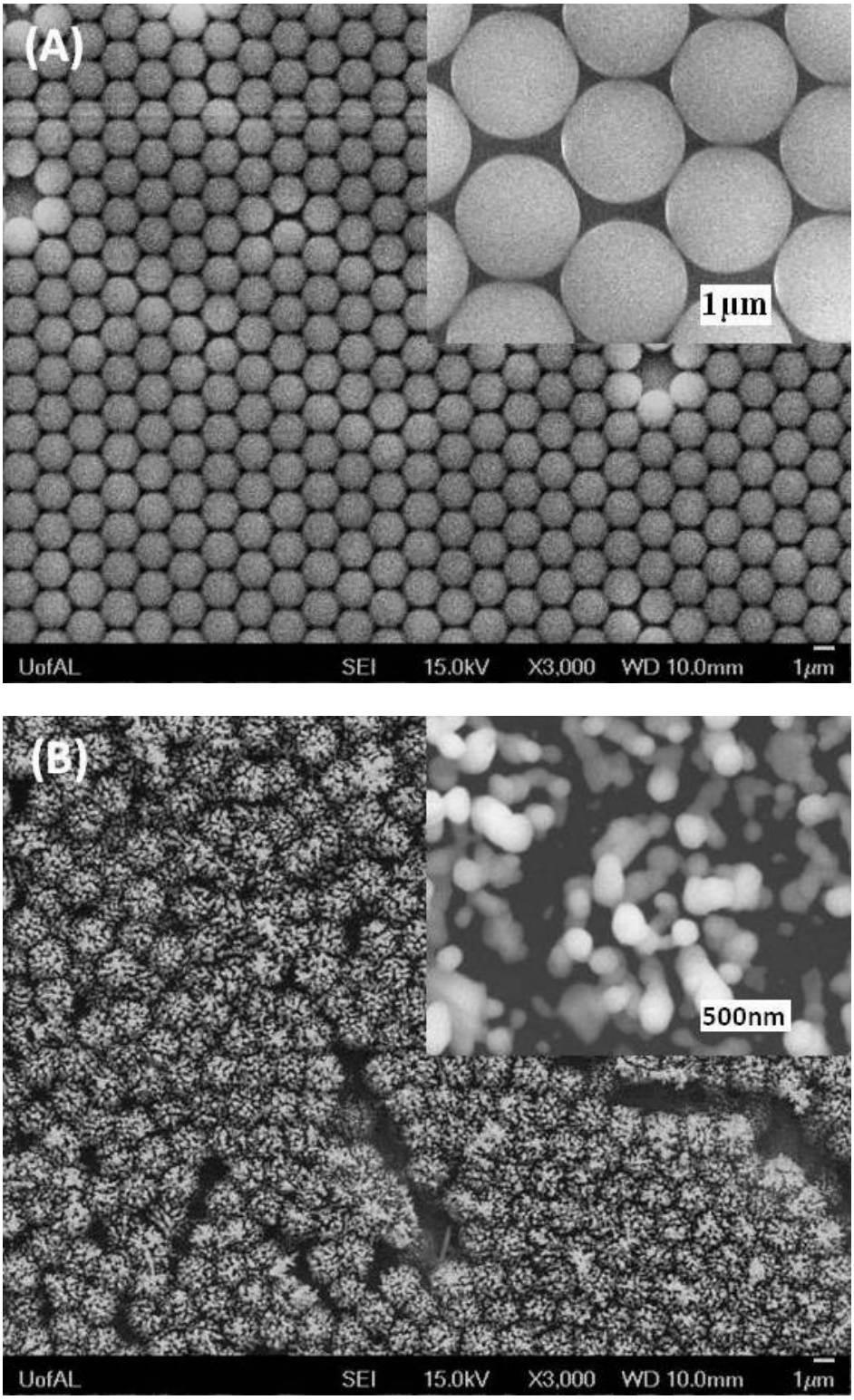

Figure 7.12 (A) top-view SEM images of PS spheres self-assembled on ITO substrate; (B) top-view SEM images of Ag NW bundles electrodeposited on ITO substrate through PS template.

7.4 Conclusions

Vertically aligned Ag nanoplates were successfully prepared on ITO substrate through a two-step electrodeposition with the assistance of AAO template attached on the ITO substrate. Importantly, the coverage, size, and thickness of Ag nanoplates could be tuned through adjusting the electrodeposition time. XRD pattern shows these Ag nanoplates grow preferably along (111) facet with a good crystallinity. It was found that the AAO template played a vital role in the growth of vertically-aligned Ag nanoplates by controlling the direction of Ag diffusion as well as lowering the diffusion rate of Ag cations. With a chemical clean surface, the Ag nanoplates with a suitable coverage, size, and thickness are able to serve as a SERS substrate. This simple approach of fabricating nanoplates could be utilized to prepare other metal nanoplates on various conductive substrates which will have promising applications.

REFERENCES

(1) Lee, W.; Park, S. Porous Anodic Aluminum Oxide: Anodization and Templated Synthesis of Functional Nanostructures. *Chem. Rev.* **2014**, *114,* 7487–7556.

(2) Choi, J.; Sauer, G.; Nielsch, K.; Wehrspohn, R. B.; Gösele, U. Hexagonally Arranged Monodisperse Silver Nanowires with Adjustable Diameter and High Aspect Ratio. *Chem. Mater.* **2003***, 15*, 776-779.

(3) Sun, B.; Jiang, X.; Dai, S.; Du, Z. Single-Crystal Silver Nanowires: Preparation and Surface-Enhanced Raman Scattering (SERS) Property. *Materials Letters* **2009***, 63*, 2570-2573.

(4) Furneaux, R. C.; Davidson, A. P.; Rigby, W. R. The Formation of Controlled-Porosity Membranes from Anodically Oxidized Aluminium. *Nature* **1989***, 337*, 147-149.

(5) Ersching, K.; Dorico, E.; da Silva, R. C.; Zoldan, V. C.; Isoppo, E. A.; Viegas, A. D. C.; Pasa, A. A. Surface and Interface Characterization of Nanoporous Alumina Templates Produced in Oxalic Acid and Submitted to Etching Procedures. *Mater. Chem. Phys.* **2012***, 137*, 140-146.

(6) Byun, J.; Lee, J. I.; Kwon, S.; Jeon, G.; Kim, J. K. Highly Ordered Nanoporous Alumina on Conducting Substrates with Adhesion Enhanced by Surface Modification: Universal Templates for Ultrahigh-Density Arrays of Nanorods. *Adv Mater* **2010***, 22*, 2028-2032.

(7) Gu, W.; Liao, L. S.; Cai, S. D.; Zhou, D. Y.; Jin, Z. M.; Shi, X. B.; Lei, Y. L. Adhesive Modification of indium–tin-Oxide Surface for Template Attachment for Deposition of Highly Ordered Nanostructure Arrays. *Appl. Surf. Sci.* **2012***, 258*, 8139-8145.

(8) Bian, J.; Li, Z.; Chen, Z.; He, H.; Zhang, X.; Li, X.; Han, G. Electrodeposition of Silver Nanoparticle Arrays on ITO Coated Glass and their Application as Reproducible Surface-Enhanced Raman Scattering Substrate. *Appl. Surf. Sci.* **2011***, 258*, 1831-1835.

(9) Jana, N. R.; Gearheart, L.; Murphy, C. J. Evidence for Seed-Mediated Nucleation in the Chemical Reduction of Gold Salts to Gold Nanoparticles. *Chem. Mater.* **2001***, 13*, 2313-2322.

(10) Chen, H.; Simon, F.; EychmuÌˆller, A. Large-Scale Synthesis of Micrometer-Sized Silver Nanosheets. *J. Phys. Chem. C* **2010***, 114*, 4495-4501.

(11) Pan, H.; Sun, H.; Poh, C.; Feng, Y.; Lin, J. Single-Crystal Growth of Metallic Nanowires with Preferred Orientation. *Nanotechnology* **2005***, 16*, 1559-1564.

(12) Wang, H. H.; Liu, C. Y.; Wu, S. B.; Liu, N. W.; Peng, C. Y.; Chan, T. H.; Hsu, C. F.; Wang, J. K.; Wang, Y. L. Highly Raman-Enhancing Substrates Based on Silver Nanoparticle Arrays with Tunable Sub-10nm Gaps. *Adv Mater* **2006***, 18*, 491-495.

(13) Hildebrandt, P.; Stockburger, M. Surface-Enhanced Resonance Raman Spectroscopy of Rhodamine 6G Adsorbed on Colloidal Silver. *J. Phys. Chem.* **1984***, 88*, 5935-5944.

CHAPTER 8

FUTURE WORK

Vertically standing metal NRs and NWs were successfully prepared using the template-free method at a low cost, but the uniformity of metal NRs and NWs in diameter and length is must still be improved. Meanwhile, how to use this technique to prepare metal NRs and NWs with a diameter under 20 nm is still a big challenge. The control of diameter, length, and coverage of metal NRs and NWs should be thoroughly explored and understood as well. This could be done through optimizing the deposition voltage, the concentration of the electrolyte, and combining with alternating current (AC) technique. In addition, using this method to prepare alloy NRs and NWs is intriguing, which would have an application in magnetic recording such as recording tapes. As-prepared metal NRs and NWs are possibly able to sustain an annealing process at a certain temperature to be converted to metal oxide, which would broaden their applications further into photocatalyst, solar cell, and batteries. Or since Ag is easily converted to Ag_2S, CdS thin film could be obtained through ion exchange with Cd salt solution. The thickness of CdS film can be tuned through adjusting the ion exchange time. This will be good model for studying the influence of the surface plasmonic effect on the electrochemical performance of photocatalysts.

Given that Ag NRs and NWs prepared in the template free methods are not uniform in diameter and length which brings difficulty to the study of the longitudinal mode of surface plasmon, these NWs and NRs could be scratched off their substrates and re-dispersed in solution. Then the influence of plasmonic effect of each single NR and NW on SERS and electrochemical

properties of the photocatalyst could be explored independently using a polarized laser which is more focused and localized.

The corrosion of plasmonic metals is another problem that must be tackled. A thin layer of TiO_2 could be coated on these NRs and NWs to serve as a protection layer. Since the Ag and Au plasmonic structure may be expensive for commercialization, other metals such as Cu and Al could be alternatives which are much cheaper and more abundant. One thing worth noting about Al is that an oxide layer which is highly resistive could be easily formed in air, which possibly hinders the application of Al surface plasmonic structure. But we could use the Al nanostructures as the scaffolds and coat a thin layer of Ag, Au, or Cu on them to lower the cost while maintaining the strong surface plasmon.

Another interesting area is to prepare parallel metal NRs and NWs lying down on semiconductor or even insulating substrates. These metal NRs and NWs could increase the conductivity of substrate considerably and bring them into the areas of electronics. Additionally, the distance between these NRs and NWs may be altered to adjust the surface plasmon. Moreover, NRs and NWs which are lying down could be built layer by layer into a 3D sturcture. In this way, the conductivity and strength of the substrates could be enhanced.

Besides AAO template, PS template also exhibits a potential in preparing ordered plasmonic nanostructures as shown in chapter 7. Besides preparing nanostructure on the top of or under PS spheres, if an experiment is designed and carried out carefully, nanostructures could be planted right into the voids between PS spheres. The size of the voids and distance between these voids are directly linked to the diameter of PS spheres which is easily altered. Therefore, a patterned nanostructure with adjustable size and interspaces could be achieved, which means a

tunable surface plasmon is obtained because the size and interspaces of the nanostructure determine the position and intensity of the surface plasmon.

The cathodic reduction method exhibited a dramatic enhancement of the photoelectrochemical performance of hematite, but the degradation of the performance is also obvious. How to permanently improve the photoelectrochemical performance of hematite using this method remains a question and should be resolved.

Since the overall goal is to enhance the efficiency of water splitting to obtain more hydrogen more efficiently and the hematite studied in this dissertation only works for water oxidation, the counter reaction of water splitting—water reduction—should be coupled with the oxidation of water. The surface kinetics for hydrogen production ought to be explored and improved for a better overall efficiency. Meanwhile, after oxygen and hydrogen could be productively generated through water splitting, a low-cost and efficient method for the separation of the hydrogen from the oxygen should also be targeted.